Nanoelectrode Lithography: Modeling, Experimental Validation, and Instrumentation

Rashed Md. Murad Hasan

A thesis submitted for the degree of Doctor of Philosophy

Centre for Precision Manufacturing

Department of Design, Manufacturing and Engineering Management

University of Strathclyde

May 2020

Declaration Statement

This thesis is the result of the author's original research. It has been composed by the author and has not been previously submitted for examination which has led to the award of a degree.

The copyright of this thesis belongs to the author under the terms of the United Kingdom Copyright Acts as qualified by University of Strathclyde Regulation 3.50. Due acknowledgement must always be made of the use of any material contained in, or derived from, this thesis.

Signed: 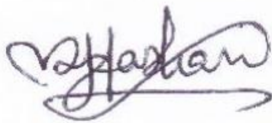

Date: 06 May 2020

Abstract

Continuous rapid shrinking of feature size made the authorities to seek alternative patterning methods as the conventional photolithography process is reaching its intrinsic resolution limit. In this regard, some promising techniques have been proposed as the next generation lithography (NGL) that have the potentials to achieve both high volume production and very high resolution. Among them, several methods such as Extreme Ultraviolet Lithography (EUVL), Electron Beam lithography (EBL), Nanoimprint Lithography (NIL), Directed Self Assembly (DSA) and Scanning Probe Lithography (SPL) have demonstrated excellent potentials as promising candidates for future industrial nanofabrication. However, all these technologies are in their development phases and still need further work to overcome some challenges in terms of flexibility, uniformity, high throughput, high resolution, high reliability, high- efficiency, defectivity, and cost of ownership. On the other hand, nanoelectrode nanolithography (NEL) has been developed in the laboratory and demonstrated as an efficient lithographic tool. It has been strengthened in recent years as one of the most promising methods due to its high reproducibility, low cost, and ability to manufacture nano-sized structures. This method is based on the spatial confinement of the anodic oxidation between a conductive stamp and the sample surface. However, the non-uniformity issue severely limits the existing nanoelectrode lithography to be applied for large area nanopatterning. Besides, other issues such as stamp lifetime and low-cost stamp fabrication method need to be addressed to make this lithography technique viable for commercial applications.

A clear and explicit understanding of the mechanism at a molecular level helps to improve this technique. Therefore, this PhD thesis firstly aims to gain an in-depth

understanding of nanoscale mechanisms involved in the anodic oxidation process and the parametric influence in nanoelectrode lithography through molecular dynamics (MD) simulations. To do this, three-dimensional MD models of oxidation nanocell were developed, and a reactive force field (ReaxFF) was adopted to describe the interactions between atoms. The MD simulations were implemented in LAMMPS software and were performed by using a High-Performance Computing (HPC) service, ARCHIE-WeSt. The simulation results demonstrated two forms of adsorption of water molecules: molecular adsorption and dissociative adsorption. After breaking the adsorbed hydroxyls, the oxygen atoms insert into the substrate to form the Si−O−Si bonds so as to make the surface oxidized. A linear dependency of the electric field intensity on oxidation growth was observed. The relative humidity also showed the same linear behavior after a certain value (40%). The simulation results have been compared qualitatively with the experimental results, and they show in good agreement.

MD simulation results also showed that the crystallographic orientation of the substrate has a great impact on the oxidation process. It was revealed that the thickness of the oxide film and the initial oxygen diffusion rate follow an order of (100) > (110) > (111) at lower electric field intensities. It also confirmed that surfaces with higher surface energy are more reactive at lower electric field intensity. Crossovers occurred at a higher electric field intensity (7 V/nm) under which the thickness of the oxide film yields an order of T(110) > T(100) > T(111). Atomic force microscope (AFM) oxidation experiments were performed to validate these results, which showed different orders for the (100) and (111) substrates, while (110) remained the largest for the oxide thickness. A good correlation has been found between the oxide growth and

the orientation-dependent parameters where the oxide growth is proportional to the areal density of the surfaces. The oxide growth also follows the relative order of the activation energies, which could be another controlling factor for the oxide growth. However, the differences between simulation and experimental results probably relate to the empirical potential as well as different time and spatial scales of the process.

Another objective of this thesis is to develop a new NEL process with a brass stamp that does not require conductive layer deposition. The brass material was chosen as it has high elastic modulus and high breaking strength, which ensures higher life expectancy. Therefore, this thesis reports the feasibility of using brass materials as the conductive stamps for NEL to shorten the process steps and reduce the production cost. The fabrication of nanostructures on the brass stamp was performed on a single point diamond turning (SPDT) machine. Some burrs were formed during the machining process, that prohibit the stamps from achieving a homogeneous contact with the substrates. Oxidation experiments were carried out with a home built NEL system. The results showed that an introduction of a thin layer of polymer (PS-OH) on the silicon substrate could improve the contact uniformity so as the oxidation.

Finally, a rolling nanoelectrode lithography process was proposed, for the first time, to scale up the nanoelectrode lithography technique for large-area nanofabrication. A test-bed was developed to realize uniform pressure distribution over the whole contact area so that the local oxidation process occurs uniformly over a large area of the samples. A brass roller wrapped with a fabricated polycarbonate strip has been used as a stamp to generate nanopatterns on a silicon surface. The experimental results indicated that a significant improvement in pattern uniformity compared to the other results was obtained with the conventional NEL process.

Moreover, the impact of pattern direction has been investigated, which shows no significant variation in the oxide pattern. Lastly, the rolling speed and the applied bias voltage were identified as the primary control parameters for the oxide growth.

Acknowledgments

First and foremost, I would like to express my sincere gratitude to my supervisor Professor Xichun Luo. It is no exaggeration to say that without his consistent guidance, support, ingenuity, and encouragement, this thesis would never have existed. I also wish to thank my co-supervisor Professor Yi Qin, for his support and valuable suggestions.

My sincere thanks go to Professor Olivier Politano from ICB, Université Bourgogne Franche, France. His knowledge and assistance helped me to accomplish the molecular dynamics simulations. I would also like to acknowledge Professor Ricardo Garcia and Dr. Francisco Espinosa Barea from Instituto de Ciencia de Materiales de Madrid, CSIC, Spain for their valuable support, and giving me access to their laboratory instruments. I also extend my sincere thanks to Dr. Saurav Goel and Mr. Alan Heaume from Cranfield University, UK, for their generous support in machining the brass roller.

I want to thank my friends and colleagues Dr. Wenlong Chang, Dr. Yukui Cai, Dr. Wenbin Zhong, Dr. Fei Ding as well as all members of the Centre for Precision Manufacturing for their kind hospitality and support.

Financial support from the University of Strathclyde and EPSRC (EP/K018345/1 and EP/T024844/1) grant is thankfully acknowledged. I also recognize the use of the EPSRC (EP/K000586/1) funded ARCHIE-WeSt High-Performance Computer at the University of Strathclyde.

My appreciations also go to my siblings and their families, my parents-in-law, and my brothers-in-law. They have all been fantastic and very supportive during all stages of my study. Words would be few to describe my gratitude towards my beloved

parents, Mr. Mahabub ul Alam and Mrs. Syeda Jahera Nur Begum. This journey would not have been possible without their never-ending love and support. I dedicate this work to my beloved parents.

Finally, I must thank my wonderful wife, Tazreen Sadaf, for her endless patience, encouragement, and support. I need to thank my little boy, Wafiq Omair Nuraz, for being such a bundle of joy and relief from the scholarly endeavor.

List of Publications

Journal papers:

1. **Rashed Md. Murad Hasan** and Xichun Luo, 'Promising Lithography Techniques for Next-Generation Logic Devices,' *Nanomanufacturing and Metrology*, (2018) 1:67–81.

2. **Rashed Md. Murad Hasan**, Olivier Politano and Xichun Luo, 'ReaxFF molecular dynamics simulation study of nanoelectrode lithography oxidation process on silicon (100) surface,' *Applied Surface Science*, 496 (2019) 143679.

3. Y. Cai, X. Luo, Y. Tian, **R. M. M. Hasan**, W. Chang and Y. Qin, 'Dynamic behaviours of water droplets impacting on laser ablated surfaces,' *Colloids and Surfaces A*, 580 (2019) 123743.

4. **Rashed Md. Murad Hasan**, Olivier Politano and Xichun Luo, 'Substrate orientation effects on nanoelectrode lithography: ReaxFF molecular dynamics and experimental study,' *Journal of Physics D: Applied Physics*, 53 (2020) 295108.

5. **Rashed Md. Murad Hasan**, Xichun Luo and Jining Sun, 'Rolling Nanoelectrode Lithography,' *Micromachines*, 11 (2020) 656.

Conference papers:

1. **Rashed Md. Murad Hasan** and Xichun Luo, 'Nanolithography: Status and Challenges,' In: 23rd International Conference on Automation & Computing (ICAC), Huddersfield, 2017, pp. 1-6.

2. **Rashed Md. Murad Hasan,** Fei Ding, Xichun Luo and Andrew Cox, 'Nanoelectrode Lithography of Silicon surface by Brass Stamp,' In: 7th International Conference on Nanomanufacturing, Xi'an, China, 2020. (Submitted).

Table of Contents

Declaration Statement .... **II**

Abstract .... **III**

Acknowledgments .... **VII**

List of Publications .... **IX**

Journal papers: IX

Conference papers: IX

Table of Contents .... **X**

List of Tables .... **XVI**

List of Figures .... **XVII**

Nomenclature .... **XXIII**

Abbreviations .... **XXV**

Chapter 1 Introduction **1**

1.1 Background 1

1.2 Aim and objectives 2

1.3 Thesis overview 3

Chapter 2 Literature Review **5**

2.1 "State of the art" in nanolithography 5

2.2 Extreme ultraviolet lithography 7

2.2.1 Mechanism *7*

2.2.2 Status and challenges *8*

2.2.3 Advantages and disadvantages *12*

2.3 Electron beam and Focused ion beam lithography 13

2.3.1 Mechanism *13*

2.3.2 Status and challenges *14*

2.3.3 Advantages and disadvantages *16*

2.4 Nanoimprint lithography 17

2.4.1 Mechanism *17*

2.4.2 Status and challenges *19*

2.4.3 Advantages and disadvantages *23*

2.5 Directed self-assembly 24

2.5.1 Mechanism *24*

2.5.2 Status and challenges *25*

2.5.3 Advantages and disadvantages *28*

2.6 Scanning probe lithography 28

2.6.1 Mechanism *28*

2.6.2 Status and challenges *30*

2.6.3 Advantage and disadvantage *34*

2.7 Nanoelectrode lithography 35

2.7.1 Mechanism *35*

2.7.2 Status and challenges *38*

2.7.3 Advantages and disadvantages *43*

2.8 Comparison 44

2.9 Molecular Dynamics simulation approach 47

2.9.1 Principle of molecular dynamics *48*

2.9.2 Ensembles *50*

2.9.3 Boundary conditions *50*

2.9.4 Potential energy function/force field 51

2.9.5 Previous simulation studies on the oxidation process of Silicon. 54

2.10 Summary 56

Chapter 3 Modeling of the NEL Process.. 59

3.1 Introduction 59

3.2 MD simulation scheme 59

3.3 Modeling of the systems and simulation procedure........................... 60

3.4 Potential energy function employed in MD simulations................... 64

3.4.1 ReaxFF potential principle 64

3.4.2 Calculation of bond order and bond energy............................... 66

3.4.3 The energy of nonbonded atoms 67

3.4.4 Polarization of charges.. 67

3.5 Introduction of the electric field in the code LAMMPS / ReaxFF 69

3.6 Validation of the modified LAMMPS with ReaxFF.......................... 70

3.6.1 Force field validation.. 70

3.6.2 Validation of the introduction of the electric field...................... 73

3.7 Summary 74

Chapter 4 MD Simulated Study for the NEL Oxidation Process....................... 75

4.1 Introduction 75

4.2 Analysis of the oxidation process 75

4.3 Effect of the electric field.. 85

4.4 Effect of the relative humidity (RH) 90

4.5 Summary 92

Chapter 5 MD Simulated Study of Substrate Orientational Effects on NEL and Experimental Validation 94

5.1 Introduction 94

5.2 Analysis of the oxidation kinetics 94

5.3 Influence of applied electric field 101

5.4 Experimental results 103

5.5 Possible explanation for the order of oxide growth 106

5.6 Summary 107

Chapter 6 Nanoelectrode Lithography by Flat Stamps 109

6.1 Introduction 109

6.2 NEL system prototype: design and implementation 109

6.2.1 Three axes translational displacement 109

6.2.2 Sample metal base 110

6.2.3 Stamp holder 111

6.2.4 Humidity controlling and measurement 111

6.2.5 Power supply and weighing scale 111

6.2.6 Computer control 111

6.3 Stamp preparation 113

6.3.1 Preparation of the polycarbonate stamp 113

6.3.2 Fabrication of brass stamp with SPDT process 115

6.4 Nano-patterning with polycarbonate stamp 118

6.4.1 Preparation of the samples 118

6.4.2 Oxidation process and results 119

6.5 Nano-patterning with brass stamp 121

6.5.1 Preparation of the sample *121*

6.5.2 Oxidation process and results *123*

6.6 Advantage and disadvantage of brass stamps in the NEL process .. 125

6.7 Summary 126

Chapter 7 Rolling Nanoelectrode Lithography 127

7.1 Introduction 127

7.2 Description of the rolling NEL system 127

7.3 Fabrication of the roller stamp 131

7.4 Implementation of the R-NEL system 133

7.5 Experimental methods 135

7.5.1 Preparation of the samples *136*

7.5.2 Contact area calculation *136*

7.6 Results and discussion 137

7.6.1 Nanofabrication with R-NEL *137*

7.6.2 Influence of the pattern directions *139*

7.6.3 Effect of the rolling speed *141*

7.6.4 Effect of the applied bias voltage *142*

7.7 Summary 143

Chapter 8 Conclusions and Future Works 145

8.1 Conclusions 145

8.2 Contributions to knowledge 148

8.3 Recommendations for future works 148

Appendix A: RH calculations [218] 151

Appendix B: Specification of Air Bushing 152

References 153

List of Tables

Table 2.1 Comparison of NGL techniques. 45

Table 2.2 List of MD potentials. 52

Table 3.1 Characteristics of the simulated systems. 63

Table 3.2 Cohesive energy and surface energy of silicon computed with different potentials, DFT calculations, and experiments. 72

Table 4.1 O/Si stoichiometry in the oxide film.. 89

Table 4.2 The thickness of the water layers for different simulation models. 90

Table 6.1 Machining condition and tool geometry. 115

Table 7.1 Parameters for contact-area calculation. 137

Table B Specification of air bushing [270] 152

List of Figures

Figure 2.1 Schematic of a EUVL system [15]. 8

Figure 2.2 The process steps of (a) EBL and (b) FIBL system................................. 14

Figure 2.3 Basic NIL process steps. 17

Figure 2.4 Schematic illustration of the DSA processes [78]. 25

Figure 2.5 Outline of the SPM lithography processes. (a) m-SPL. (b) t-SPL. (c) o-SPL. (d) DPL. 30

Figure 2.6 Diagram of the NEL process steps. 36

Figure 2.7 Schematic of the oxidation nanocell [153]. 38

Figure 2.8 (a) SEM image of silicon substrate after oxidation using SiC stamp [5]. (b) SEM image of silicon substrate after oxidation using a DVD stamp [4]. (c) AFM image and the profile of a silicon surface after KOH etching. (d) AFM image and the profile of a silicon substrate after dry etching using fluorocarbon gas. 39

Figure 2.9 XPS spectra measurement [7]... 40

Figure 2.10 Process of multiple patterning [7]. a) First patterning. b) Second patterning. (c) AFM image of the pattern after two successive oxidations. 41

Figure 2.11 AFM/SEM images of Template growths. (a) deposition of the TTF derivative [8]. (b) deposition of anti-BSA antibodies [11]. (c) Au nanoparticle arrays [158]. 42

Figure 2.12 (a) Variation of oxide height with the thickness of the PMMA layer. (b) Percentage of the patterned area as a function of the PMMA thickness [8]. 42

Figure 2.13 Resolution and throughput in nanolithography. 46

Figure 2.14 Schematic of molecular dynamics. 49

Figure 2.15 Chemical elements currently described by the ReaxFF potential [205]. 54

Figure 2.16 (a) MD evolution of water molecules in the presence of an external electric field. (b) Height of the water bridge as a function of time for six values of the electric field (2.25, 2.0, 1.75, 1.5, 1.25, and 1.0 V/nm). The dotted lines present the fit to the sigmoidal function [213]. 55

Figure 3.1 Sequence of steps for MD simulations. 60

Figure 3.2 Simulation model. 61

Figure 3.3 Crystal planes of the silicon substrates. 62

Figure 3.4 Simulation models: Si (orange), O (red), and H (white) atoms. 62

Figure 3.5 Evolution of the total energy of the system over time for different values of the electric field. 73

Figure 3.6 Evolution of the system temperature over time for different values of the electric field. 74

Figure 4.1 Side view and top view of the system after 400 ps of simulation. 76

Figure 4.2 The interaction between H_2O and Si (100) substrate surface. (a) Three water molecules in which one water molecule (numbered 1) adsorbed on the Si substrate surface. (b) Dissociation of water and the formation of Si−OH and H_3O^+. (c) Proton transfer process between two adjacent water molecules. 76

Figure 4.3 (a) Two water molecules on the Si surface. (b) Formation of Si−H and Si−OH. (c) Bond breaking of Si−OH to form Si−O−Si and H_3O^+ formation. .. 77

Figure 4.4 Evolution of the oxide film for an electric field of 2 V/nm. 79

Figure 4.5 Evolution of the chemical compositions for an electric field of 2 V/nm. 80

Figure 4.6 Partial radial distribution functions in the oxide film. 82

Figure 4.7 g(r) after melting. 82

Figure 4.8 g(r) after cooling. 83
Figure 4.9 Oxygen atoms distributions below the Si surface at 400 ps. Z is the depth below the surface, and its origin is taken as the initial surface position. 84
Figure 4.10 Distribution of atomic charges after 400 ps. 84
Figure 4.11 Evolution of oxide film thickness for various electric field intensities. 86
Figure 4.12 The thickness of the oxide film as a function of the electric field at 400 ps. 86
Figure 4.13 Evolution of the H_2O molecules time for the different electric fields. 87
Figure 4.14 Evolution of the H_3O^+ over time for the different electric fields. 88
Figure 4.15 Evolution of the number of oxygen atoms over time in the oxide film for the different electric fields. 88
Figure 4.16 RDF of Si-O pairs in the oxide film for different electric fields after 400 ps. 89
Figure 4.17 Evolution of oxide film for different relative humidity (RH) with an applied electric field of 5 V/nm. 91
Figure 4.18 The height of the oxide film as a function of the relative humidity with an applied electric field of 5 V/nm. 92
Figure 5.1 Side views of the three systems after 400 ps at 300 K. 95
Figure 5.2 First formation of Si−O−Si. 95
Figure 5.3 Number of H_2O in the three systems. 96
Figure 5.4 Number of H_3O^+ in the three systems. 96
Figure 5.5 Evolution of oxide films for an electric field of 7 V/nm at 90% RH. 97
Figure 5.6 Ratio of the Si−H_2O number to the Si−OH number. The data are average of the last 100 ps. 98

Figure 5.7 Evolution of the number of oxygen atoms over time in the oxide film.... 99

Figure 5.8 Partial radial distribution functions in the oxide film. 100

Figure 5.9 Oxygen atoms distributions inside Si substrates along the z direction at 400 ps. 100

Figure 5.10 Mulliken charge distributions of the Si atoms for three crystallographic orientations at 400 ps. 101

Figure 5.11 Rate of initial oxygen diffused in the surfaces for different electric fields. 102

Figure 5.12 Thickness of the oxide films for different electric fields..................... 103

Figure 5.13 AFM images of nanostructures on different substrates and height cross-section along the lines marked in the images. 105

Figure 5.14 The oxide height for different substrates obtained with a bias of 12 V and 44% RH. 105

Figure 6.1 Panoramic view of the NEL prototype system. 110

Figure 6.2 Sample metal base. 112

Figure 6.3 Software interface. 112

Figure 6.4 System enclosure, power supply, and the Computer control system. 112

Figure 6.5 Schematic of a conventional DVD-R. (a) Spiral guide grooves. (b) Internal structure. 114

Figure 6.6 (a) Image of the stamp peeled off from a DVD-R. (b) AFM image shows the surface morphology of the motifs. (c) Profile of the motifs...................... 114

Figure 6.7 Fabrication of brass stamp with SPDT. (a) Machining set up. (b) Brass stamp after flat turning. (c) Brass stamp after microstructure fabrication. 116

Figure 6.8 (a) AFM images of the fabricated brass structures. (b) Burrs are marked to visualize clearly. (c) Profile of the fabricated structures. (d) Surface topography on the top of a motif. 117

Figure 6.9 RCA cleaning of the sample. (a) Less water droplets were adhered to the sample before cleaning. (b) More water droplets were adhered to the sample after cleaning. (c) AFM topography image of silicon after the cleaning process. 119

Figure 6.10 (a) AFM topography images of the oxide lines. (b) Profile of the oxide lines in the region marked by the line drawn in figure (a). 120

Figure 6.11 [5] (a) AFM topography images of the DVD stamp. (b) Cross-section of DVD stamp in the region marked by the line drawn in figure (a). (c) AFM topography images of the sample after the oxidation process. (d) Cross-section of the sample in the region marked by the line drawn in figure (c). 121

Figure 6.12 AFM topography images of the silicon surfaces. (a) After oxidation process. (b) After RIE etching process. 122

Figure 6.13 Schematic of the Si substrate with PS-OH brush layer. 122

Figure 6.14 (a)-(c) Optical image of the motifs at different areas of the substrate after the RIE etch process. (d) Profile of the silicon lines manufactured. 124

Figure 6.15 Unoxidized areas on the substrate due to burrs. 124

Figure 6.16 (a) AFM images of the brass stamp after 15 operations. (b) Profile of the motifs. 125

Figure 7.1 Schematic of the proposed rolling NEL system. 128

Figure 7.2 Design concept of a prototype of the rolling NEL system. 129

Figure 7.3 Contact area calculation with deformed/elastic roller. 131

Figure 7.4 (a) Peeled polycarbonate strip. (b) Roller with a rubber band. (c) Completed roller stamp. 132

Figure 7.5 (a) AFM topographic image of the roller stamp. (b) Line profile of the AFM image. 133

Figure 7.6 Air bushing system. 134

Figure 7.7 Airflow controller. 134

Figure 7.8 Implemented R-NEL system. 135

Figure 7.9 AFM topography images of the distorted oxide pattern. 138

Figure 7.10 (a) AFM topography image of the oxide lines made by R-NEL. (b) Profile of the line marked in the image (a). 139

Figure 7.11 Schematic diagram of pattern directions. (a) Orthogonal. (b) Parallel. 140

Figure 7.12 Parallel pattern direction. (a) AFM topography image of the oxide lines. (b) Profile of the lines marked in the image (a). 140

Figure 7.13 (a)-(c) AFM topographic images. (d) Relationship between the rolling speed and oxide height (left side of the graph) and FWHM (right side of the graph). 141

Figure 7.14 Height of oxide lines for different applied bias voltages at a rolling speed of 0.50 mm/minute. 143

Figure A The curves represent twice the theoretical values of the film thickness, 2d (grey), and the radius of the meniscus, 2k (black) vs the relative humidity. ... 151

Nomenclature

m_i	Mass of the atom i
a_i	Acceleration of the atom i
r_i	Position vector of the atom i
F_i	Force on the atom i
E_{ReaxFF}	ReaxFF energy
E_{bond}	Bond energy
E_{lp}	Lone-pair energy
E_{over}	Overcoordination energy
E_{under}	Undercoordination energy
E_{val}	Valence angle energy
E_{pen}	Penalty energy
E_{coa}	Angle conjugation energy
E_{conj}	Torsion conjugation energy
E_{tors}	Torsion energy
E_{hbond}	Hydrogen bond energy
r_{ij}	Relative position between atom pair
r_{ijk}	Relative position between triplets of atoms
r_{ijkl}	Relative position between quadruplets of atoms
q_j	Atomic charge distribution
BO_{ij}	Bond order between a pair of atoms
$E_{vdWalls}$	van der Waals energy
$E_{Coulomb}$	Coulomb interaction energy

k_c	Dielectric constant
χ	Electronegativity of each atom
η	Hardness of each atom
γ	Shielding parameter
$\mathbf{R}_v$	Spatial positions
E_{surf}	Surface energy
A	Surface area
E_m	Elastic moduli
v	Poisson's ratio
R	Radius
L	Length
b	Half-width of the rectangular contact area
t	Time

Abbreviations

AFM	Atomic Force Microscope
AIMS™	Aerial Image Measurement System™
AI-REBO	Adaptive Intermolecular Reactive Empirical Bond Order
BCP	Block Co-Polymer
BO	Bond Order
CAR	Chemically Amplified Resist
CD	Critical Dimension
CDU	Critical Dimension Uniformity
CHIPS	Chemo-epitaxy Induced by Pillar Structures
CoO	Cost of Ownership
CMG	Chemically Modified Graphene
COMB	Charge Optimized Many-Body
COOL	Coordinated Line epitaxy
DPL	Dip-Pen Lithography
DPP	Discharge Produced Plasma
DRAM	Dynamic Random Access Memory
DSA	Directed Self Assembly
DUV	Deep Ultraviolet
DVD	Digital Versatile Disc
EAM	Embedded-Atom Method
EBL	Electron Beam Lithography
EEM	Electronegativity Equalization Method

EFF	Empirical Force Field
EIM	Embedded-Ion Method
EPE	Edge Placement Error
EUV	Extreme Ultraviolet
EUVL	Extreme Ultraviolet Lithography
FCM	Flexible Conductive Mold
FEL	Free-Electron Laser
FET	Field Effect Transistor
FIBL	Focused Ion Beam Lithography
FWHM	Full Width at Half Maximum
HIM	Helium Ion Microscope
HODC	High Order Distortion Correction
HP	Half Pitch
HPC	High-Performance Computing
HSQ	Hydrogen Silsesquioxane
HVM	High-Volume Manufacturing
IC	Integrated Circuit
i-MAT	interferometric Moiré Alignment Technology
ITRS	International Technology Roadmap for Semiconductors
J-FIL	Jet and Flash Imprint Lithography
LADI	Laser Assisted Direct Imprint
LAMMPS	Large-scale Atomic/Molecular Massively Parallel Simulator
LELE	Litho-Etch-Litho-Etch
LER	Line Edge Roughness

LiNe	Liu–Nealey chemoepitaxy
LPP	Laser Produced Plasma
LWR	Line Width Roughness
MD	Molecular Dynamics
MEAM	Modified Embedded-Atom-Method
MEBDW	Multiple E-Beam Direct Write
ML	Mono Layer
MPI	Message-Passing Interface
MSCS	Mask Magnification and Shape Control System
MTR	Multi-Trigger Resist
NA	Numerical Aperture
NEL	Nanoelectrode Lithography
NGL	Next Generation Lithography
NIL	Nanoimprint Lithography
NPGS	Nanometer Pattern Generation System
OAI	Off-Axis Illumination
OPC	Optical Proximity Correction
OVITO	Open Visualization Tool
PBC	Periodic Boundary Condition
PEB	Post Exposure Bake
PLDC	Pixel Level Dose Correction
PMMA	Poly(methyl methacrylate)
PS-b-PDMS	Polystyrene-block-poly(dimethylsiloxane)
PS-OH	Hydroxyl-terminated Polystyrene

P2VP-b-PDMS	Poly(2-vinylpyridine)-block-poly(dimethylsiloxane)
QC	Quantum Chemical
QEq	Charge Equilibration
RDF	Radial Distribution Function
ReaxFF	Reactive Force Field
RESCAN	Reflective-mode EUV mask scanning lensless imaging microscope
RET	Resolution Enhancement Technologies
RH	Relative Humidity
RIE	Reactive Ion Etching
RLS	Resolution LER Sensitivity
SADP	Self-Aligned Double Patterning
SAQP	Self-Aligned Quadruple Patterning
SAM	Self-Assembled Monolayers
SEM	Scanning Electron Microscope
SIT	Sidewall Image Transfer
SMART™	Surface Modification for Advanced Resolution Technology™
SMO	Single Machine Overlay
SPDT	Single Point Diamond Turning
SPL	Scanning Probe Lithography
SPM	Scanning Probe Microscopes
STEM	Scanning Transmission Electron Microscope
SW	Stillinger-Weber
TTF	Tetrathiafulvalene

WPH	Wafers Per Hour
XMMO	Crossed Matched Machine Overlay
XPS	X-ray Photoelectron Spectroscopy
193i	193nm Immersion Lithography

Chapter 1 Introduction

1.1 Background

As reported by the International Technology Roadmap for Semiconductors 2015 (ITRS2015) that new types of logic devices (Gate-all-around structures) have already been introduced, which will replace the fin structures soon [1]. This report also demonstrates the development of many new types of memory devices that can be possible alternatives in the future. These advanced devices require sub-10 nm feature dimensions. As the feature size continues to shrink rapidly in keeping with Moore's law, the dominant conventional photolithography process is reaching its intrinsic resolution limit. Moreover, this rapid shrinking of feature size intensely enhances the design complexity and introduces various manufacturing challenges. Consequently, lithography techniques must accomplish the stringent industrial requirements with excellent capability to meet future challenges.

Various alternative patterning techniques have already been investigated to overcome this intrinsic resolution limit of photolithography. They have the potentials to achieve both high volume production and very high resolution. However, these promising methods are facing numerous challenges, such as low throughput, large facilities requirement, non-uniformity, defectivity, and high cost. To further boost the efficiency and lower the cost, fabrication techniques, which are capable of replicating nanostructures, became a hot topic in the last decades, among which the most widely adopted technique is nanoimprint lithography (NIL). Nevertheless, the NIL techniques suffer from several challenges relating to the resist, such as trapped air in the transferred patterns due to the bubble defects [2, 3] and defective patterns due to

adhesion between the stamp and the resist during the demolding process. To overcome these challenges, a resistless local oxidation-based nanoimprint technique called nanoelectrode lithography (NEL) is introduced [4, 5]. Nanoelectrode lithography can be a promising candidate owing to its high resolution, reduced process steps, high accuracy, and low cost of operation. It has already been developed in the laboratory and been demonstrated as an efficient lithographic tool. This method is based on the spatial confinement of the anodic oxidation between a conductive stamp and the sample surface and has effectively been used in the patterning of different substrates: silicon [6-8], GaAs [9, 10] and pentacene layers [11].

However, the non-uniformity issue severely limits the existing nanoelectrode lithography to be applied for large area nanopatterning. The existing NEL systems require large-sized flat stamps to fabricate nanostructures in large areas. It is difficult to achieve a uniform contact between the stamp and the sample with these large stamps. Besides, other issues such as stamp lifetime and low-cost stamp fabrication method need to be addressed to make this technique viable for commercial applications. Overcoming this non-uniformity constraint and in search of new stamp materials for the NEL process is the key motivation behind this work.

1.2 Aim and objectives

This thesis aims to establish a new cost-effective nanoelectrode lithography technique and its test-bed for the large-area nanofabrication. Besides, a clear and explicit understanding of the mechanism at a molecular level helps to improve the NEL technique. Moreover, the parametric influences, such as crystallographic orientation is still unexplored. As the instantaneous oxidation processes are difficult to observe experimentally, this thesis uses the advantages of a molecular dynamics (MD)

simulation study to investigate the oxidation mechanism and the parametric effects. The principal objectives are:

1. To review the state-of-the-art nanofabrication approaches and identify the knowledge gap.
2. To investigate the atomistic insight into the dynamics of the local anodic oxidation process.
3. To reveal the parametric effects and the crystallographic orientational dependency on the NEL process.
4. To investigate the feasibility of the new stamp materials for the NEL system.
5. To design and develop a new roller based nanoelectrode lithography system that can facilitate to achieve uniform large-area patterns fabrication.

1.3 Thesis overview

This work is divided into 8 chapters. As an introduction to the first chapter, the background of the thesis is explained, and the aim & objectives of this research are determined.

- Chapter 2 presents a comparative assessment of the next generation lithography techniques in terms of their mechanisms, status, and challenging issues. The basic principles and the framework of the molecular dynamics simulations are also discussed. It also presents a review of the previous simulation studies performed to understand the oxidation process.

- Chapter 3 provides a detailed description of the MD simulation technique employed in this study, including the simulation procedure, the force field, and the simulation conditions.

- In Chapter 4, the results obtained from the reactive force field (ReaxFF) MD simulations of the NEL oxidation mechanism are presented. Apart from the structural and morphological features related to the growth of the oxide film, the influences of the experimental parameters (applied voltage, exposure time, and relative humidity) on the NEL process are also discussed.

- Similarly, Chapter 5 describes the ReaxFF MD simulation results for the substrate orientation effects in the NEL process. It also presents the AFM oxidation experimental results to verify the simulation results. This chapter also explains the possible reasons for the orientational effects on oxide growth.

- Chapter 6 contains the implementation of a NEL system and the experimental study to examine the feasibility of using brass as a conductive stamp for the NEL process. It includes the fabrication of brass stamp with Single Point Diamond Turning (SPDT) machine and the fabrication of nanostructures by using it.

- Chapter 7 proposes and develops a rolling NEL system, for the first time, through a new instrument designed for large area nanofabrication. The parametric effects, such as rolling speed, pattern direction, and applied voltage, are also analyzed.

- Lastly, Chapter 8 contains a summary of this work with the most relevant conclusions of it. In addition, possible future directions and recommendations are also provided.

Chapter 2 Literature Review

2.1 "State of the art" in nanolithography

Photolithography using 193 nm deep ultraviolet (DUV) is the dominant method of patterning nanoscale features today for the microelectronics industries. Resolution Enhancement Technologies (RET) and Immersion method enable the photolithography with patterning beyond its intrinsic resolution limit. RET improves the quality of an image. It generally includes phase shift mask, optical proximity correction (OPC), modified or off-axis illumination (OAI), and multiple patterning. Although they have extended the capability of the lithography process, these methods experience some restrictions as well. The phase shift method has some limitations on the implementation of a mask due to phase termination problems and masks fabrication difficulties. The OPC technique introduces layout restrictions and prohibitive costs to make the corrected masks, while OAI presents complexity to the illumination source in the wafer stepper and the mask design.

Multiple patterning is currently the leading sub-20 nm high volume manufacturing technology. It enables to print patterns with a resolution that is smaller than the single exposure lithography using multiple process steps. There are many different techniques to implement multiple patterning, including litho-etch-litho-etch (LELE), self-aligned double patterning (SADP), and self-aligned quadruple patterning (SAQP). However, more and more masks are required for achieving finer process nodes, resulting in prohibitively expensive manufacturing cost, and it requires much tighter overlay control than single patterning techniques [12]. 193 nm immersion lithography (193i) has given a significant boost to the further development of microelectronics. The 22-nm and 14-nm nodes are currently manufactured with multi-

patterning immersion ArF lithography [13]. However, this technique brings enormous process challenges like leaching, immersion defects, and the filling methods of a purified medium. Despite these challenges, it has been the mainstream lithographic technique used in microelectronics manufacturing industries since the last decade. Now it is reaching its intrinsic limits.

Even though the capability of high-resolution, X-ray lithography (utilizes x-rays wavelength of 0.4 nm to 4 nm) techniques were proved to be unsuccessful in providing an economically attractive lithographic process due to some difficulties, one of them was to find the right combination of materials and wavelength. Warping of absorber material due to internal stresses is an issue to mitigate. Furthermore, the most critical point is the failure to furnish suitable masks as these masks had to be unity magnification and the requirement of creating the mask from adequately x-ray absorbing materials. Again, the requirement of thick absorber layers and membranous nature of the substrate made X-ray lithography unpopular in the nanofabrication arena.

As the conventional photolithography has approached its ultimate limits, considerable efforts have been devoted to Next Generation Lithography (NGL) techniques by various research laboratories and industries around the globe. Some of these techniques are Extreme Ultraviolet Lithography (EUVL), Electron Beam Lithography (EBL), Focused Ion Beam Lithography (FIBL), Nanoimprint Lithography (NIL) and Directed Self Assembly (DSA). They have the potentials as the replacement to conventional photolithography. On the other hand, some emerging nanofabrication methods such as SPM based lithography (SPL) and nanoelectrode lithography (NEL) have been developed in the laboratory. They have demonstrated excellent potential as promising candidates for future industrial nanofabrication.

This chapter gives a critical review of some alternative lithographic techniques from the aspects of the mechanism, overall status, and challenging issues. Finally, it introduces the basic concept and framework of the numerical simulation approach, followed by a review of the previous simulation works performed on the NEL process.

2.2 Extreme ultraviolet lithography

2.2.1 Mechanism

Due to wavelength limitations, current attention is directed toward developing EUVL, which uses extreme ultraviolet radiation to increase efficiency, reduces manufacturing cost, and supports the development of processing power. In the last decade, researchers put extensive interest in EUVL as a "next wavelength" replacement for 193-nm DUV lithography [14]. EUVL utilizes 13.5 nm photons that are obtained typically from a plasma source. An optical element called a 'collector' then collect EUV light. Light from the collector is focused on the illuminator (formed of multilayer-coated normal incidence mirrors as well as grazing incidence mirrors) through an intermediate focus. The illuminator illuminates the right amount of light and guides it onto the reticle stage (i.e., a mask). The reflected image of the reticle arrives into the projection optics (consist of six or more multilayer mirrors) with a demagnification. Finally, the image is focused onto the wafer stage to form a pattern into a substrate coated with a photoresist. Every step is operated in a low-hydrocarbon, high vacuum environment. Figure 2.1 shows a schematic of a EUVL exposure system [15].

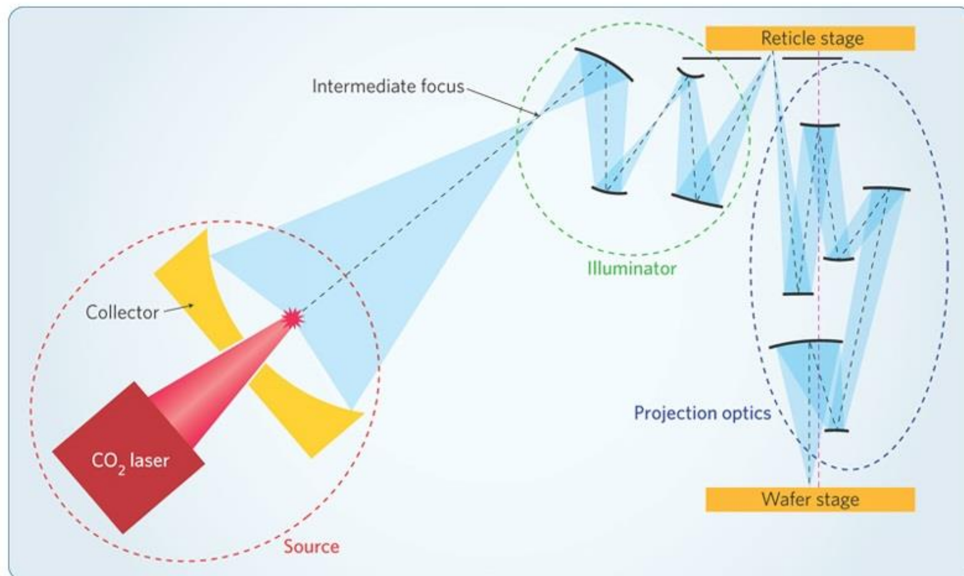

Figure 2.1 Schematic of a EUVL system [15].

2.2.2 Status and challenges

Over the last few years, considerable progress has been made to move EUVL towards increased HVM viability. Most remarkably, there have been substantial developments to exposure throughput, reliability, variance control, and patterning materials for the high resolution required [16, 17]. EUVL is now becoming industrial standard exposure metrology for the advanced technologies beyond the 7-nm node [18]. ASML, a leading company involved in the development of EUVL tools, has claimed that the throughput specification of 170 wafers per hour (WPH) can be achieved on its new generation TWINSCAN NXE:3400C EUV scanner [19]. This system also showed a chuck overlay of 1.4 nm and a matched machine overlay of 1.5 nm. Although the targeted 4-week average availability (>80%) has been achieved with NXE:3400, it needs to continue to improve further [20].

In terms of production timescales, ASML went into production in 2017. As of Q2 2019, there were 38 NXE:3400B scanner bases installed at various fabs worldwide [20]. From 2011 to 2019, the EUV systems have already run total wafers of 4.5 million [20]. The source power, masks, and resist materials still have critical issues for mass production. For the future technology at the 5-nm node and beyond, sources powers of 500-1000 W at a reduced operational cost per wafer may be required [21]. Laser Produced Plasma (LPP) and Discharge Produced Plasma (DPP) are the two main techniques to produce EUV sources. The source power has been improved ten times in recent years [22]. Igor Fomenkov of ASML reported that more than 250 W LPP-EUV powers could be generated by using plasma generation schemes [23]. Mitsubishi Electric is developing a new high-power CO_2-Sn-LPP EUV source for HVM with more than 25 kW CO_2 driver laser system to achieve 330 W with a long collector mirror lifetime and stable output [24]. Another approach by using FEL (free-electron laser), many tens of kilowatts power can be produced [25]. Although EUV source technology is very close to the requirements, some cost of ownership issues needs to be investigated before the insertion of EUVL into HVM. For further improvement, novel approaches for power sources are still investigated [26, 27].

A key factor for the adoption of EUVL in HVM is the choice of EUV resist with high sensitivity, high resolution, low line edge roughness (LER), low line-width roughness (LWR), and better contact hole critical dimension uniformity (CDU). Chemically amplified resists (CARs) have effectively achieved the scaling requirements of the semiconductor industry [28]. RLS (resolution, line-edge roughness, and sensitivity) performance and stochastic variations are the critical issues for the CARs as well as for other resist materials. High-sensitivity (< 20mJ/cm^2) resist

materials are required to reduce the development cost of high-power exposure sources that, in turn, leads to large LER values. Acid diffusion in CARs influences these performances. Y. Vesters *et al.* have reported that by selecting an appropriate ratio of quencher to PAG (photo-acid generator), a EUV dose reduction of up to 12% can be achieved with 240-second PEB (post-exposure bake) time, while keeping LWR and resolution constant [29]. For better optimization of these parameters, some other resist materials and approaches have been studied.

Non-chemically amplified resists (non-CARs) show high-resolution capability, high sensitivity, and low LER as they have no acid diffusion issues. Recently, the main chain scission type resists have been introduced for EUVL. 16 nm half-pitch patterning was achieved on the ASML NXE3300B EUV scanner with a dose of 57 mJ/cm^2 by using main chain scission type resists (ZER02) [30]. They presented an unbiased LWR of 2.7 nm and an unbiased LER of 2.0 nm. Irresistible Materials (IM) is developing a novel multi-trigger resist (MTR), which is a non-metal based negative tone resist. It consists of a base molecule and a crosslinker. The previous reports showed that 16 nm half-pitch lines were patterned by using MTR with a dose of 38 mJ/cm^2, which gave an LER of 3.7 nm [31] and with a dose of 22.5 mJ/cm^2 [32]. Some researchers have reported the development of the metal-containing photoresist that has high sensitivity performance, which could be very helpful for the low energy power source to realize EUVL [33, 34]. Some other new techniques, including nanoparticle photoresists with high sensitivity, have also been reported [35-38].

However, it is an urgent need to mitigate the stochastic failures such as broken line, nano-bridge, merging holes, and closing holes. These nano failures are influenced by many factors, including aerial image quality, photon absorption, acid shot noise,

and acid diffusion. The probable solutions lie with the co-optimization of a variety of different aspects (materials used, hardware, and metrology). An exposure dose can be a useful parameter to drive down the failures. Higher dose absorber materials can reduce the stochastics. Moreover, the substrate underneath the resist influences the exposure dose and the LWR, and therefore, optimization of the substrates could be a potential improvement parameter to the exposure dose and LWR reduction [39].

Pattern collapse is another challenging issue faced by the resists patterned at high resolution. Several strategies have been proposed to mitigate this problem. Since the capillary forces are one of the reasons for pattern collapse, eradicating any process steps where the liquid-air interface reaches the resist surface can be an effective way to avoid this problem. Moreover, mechanically robust resists are less susceptible to the damage due to the capillary forces [40]. Another way could be controlling the thickness of the resist film properly as thin-film can avoid pattern collapse during development and rinse. Some other processes were studied to decrease pattern collapse with increased resolution [41, 42].

Mask blank defects and yield limit the applicability of EUVL. One way to mitigate the defects is the pattern shift process where the design is shifted before the writing to avoid patterning over blank defects. Vadim Sidorkin *et al.*, have reported the achievement of <5 nm 3σ uncorrected image placement (IP) error for aligned patterns with these methods [43]. However, extensive researches are still needed to improve mask materials, fabrication processes, defect inspection & disposition metrology, and mask protection.

The interaction between the oblique incident EUV light and the patterned absorber may cause the Mask 3D effects at the wafer level. Vicky Philipsen *et al.* have

suggested some alternate absorber materials (Nickel and Cobalt) to reduce the 3D mask effects and to improve the overall imaging window [44]. For the defect-free mask manufacturing, ZEISS, and the SUNY POLY SEMATECH EUVL Mask Infrastructure consortium developed a EUV aerial image metrology system, the AIMS™ EUV [45]. These actinic tools are convenient for blank inspection, pattern mask inspection, and defect repair verification. Besides, Iacopo Mochi *et al.*, have developed a reflective-mode EUV mask scanning lensless imaging microscope (RESCAN), which has the capability of actinic patterned mask inspection for defects and patterns with high resolution and high throughput [46].

To enhance the patterning capability of EUVL, double patterning with existing tools can be a possible solution. Another option could be to increase the numerical aperture (NA) of the EUV projection optics. Therefore, manufacturers (ASML, ZEISS) have already made plans to generate the next generation of EUVL with High-NA (0.55), which will have a resolution of 8 nm for direct printing [47]. High-NA EUV system can be advantageous as it can mitigate the mask splits and the cumulative edge placement error (EPE) for mask splits [20]. It can also lessen the process complexity. However, this significant increase in the NA could face many challenges such as defectivity, flatness, novel absorbers substrate thermal properties, pellicle, and stitching. It also requires many adaptations. Besides, the accomplishment of EUVL as part of the integrated patterning techniques remains a critical issue, and therefore the workability of EUVL as a patterning technique continues to accelerate.

2.2.3 Advantages and disadvantages

The advantages of EUVL are high throughput, wide process windows, and extendibility to future nodes. It uses a smaller wavelength, which leads to more densely

packed components on the microchip, creating faster processing power. Hence, faster computer processors can be achieved with EUVL. This technique has the potential to provide economic sustainability with its applications in nearly every field, including engineering and medical fields. Reduced power consumption and a lessened number of exposures can make the EUVL cost-effective in most patterning processes. The disadvantages of this lithography technique are higher start-up costs, complexity, reliability, and relative infrastructure immaturity.

2.3 Electron beam and Focused ion beam lithography

2.3.1 Mechanism

EBL and FIBL are maskless techniques that are widely used in nanostructure patterning and IC (Integrated Circuit) fabrications with its ability to form arbitrary two-dimensional patterns down to the nanometer scale. EBL uses an accelerated electron beam to dramatically modify the solubility of a resist material during a subsequent development step. The electron beam is focused and scanned on the surface of the resist with the diameter as small as a couple of nanometers in a dot by dot fashion. Then the patterns can be transferred to the substrate material by etching like other lithographic methods.

Similarly, FIBL involves the exposure by an accelerated ion beam to directly hit the sample surface. When high-speed ions hit the sample surface, energy is transmitted to atoms on the surface, which leads to five possible reactions: 1) sputtering of neutral ionized and excited surface atoms, 2) electron emission, 3) displacement of atoms in the solid, 4) emission of photons, and 5) chemical reactions. Based on these phenomena, FIBL systems are also employed for depositing materials

such as tungsten, platinum, and carbon via ion beam induced deposition and the implantation that can modify a material surface. Figure 2.2 shows the process steps of the EBL and FIBL system.

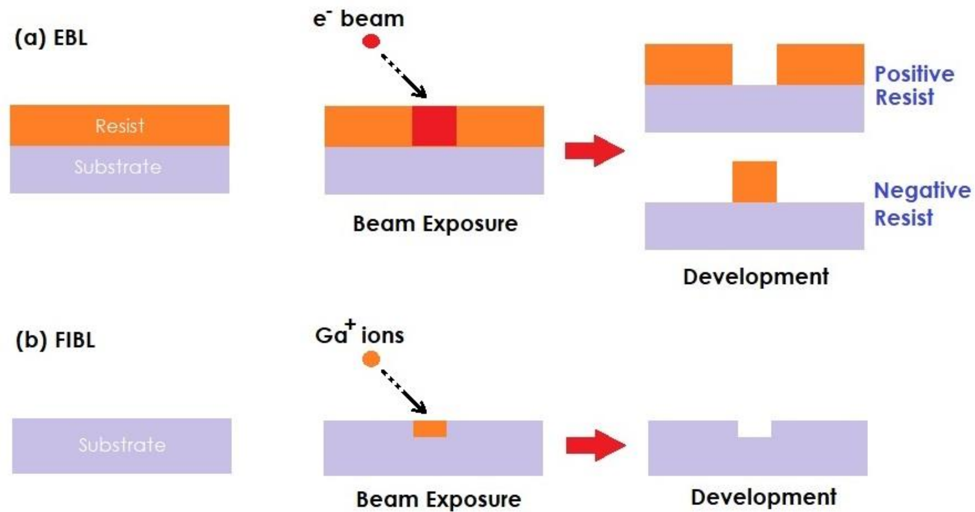

Figure 2.2 The process steps of (a) EBL and (b) FIBL system.

2.3.2 Status and challenges

Both methods suffer from low throughput that limits their applications within research and mask/mold fabrication. To increase the system throughput, multiple e-beam direct write (MEBDW) lithography concepts have been pursued with nanometer resolution, using >10,000 e-beams writing in parallel [48]. Significant developments in productivity are required to make direct-write practicable for wafers. In the past, some progress has been reported, including MAPPER (a 5kV raster wafer writer) [49], IMS (50 kV raster mask writer, single source, many spots in the single-lens field) [50], and multibeam wafer writer [51]. These are the promising solutions in exposure cost reduction for 20-nm half-pitch and beyond. Mapper's 3rd generation platform (FLX) using 650,000 beamlets has been introduced with a target of 40 wafers per hour

throughput [52]. Recently, a CDU of 7.3 nm 3 sigma, 25 nm overlay and 1 WPH throughput at 300 mm wafers have been achieved with FLX-1200 [53]. Raith has claimed that its 100 kV electron beam lithography (EBPG5200) has an overlay accuracy of ≤ 5 nm for extreme direct write precision [54]. NuFlare has developed a multi-beam mask writer (MBM-1000) for the sub-5 nm semiconductor production, which includes a pixel level dose correction (PLDC) to correct and improve the profile of dose deposited in resist [55].

As the feature size is shrinking, the resist material plays a significant role in attaining the required resolution in EBL. Because of its high sensitivity, sharp contrast, and better roughness, PMMA is one of the high-resolution resists that is commonly used in the EBL process. Like EUVL, the same CARs are often used in EBL, and they also suffer the same problem to minimize the RLS trade-off. One of the examples of commercially successful inorganic non-CAR resists used for EBL is Hydrogen silsesquioxane (HSQ), which shows high resolution (sub-5 nm) capability, high etch resistance and small local CDU [56, 57]. However, these resists display relatively low sensitivity. Hence, new high-resolution inorganic resists materials with high sensitivity have been proposed, such as metal-containing resists. Mapper Lithography, CEA-Leti, and Raith are the leading providers, are working to develop turnkey solutions for EBL and FIB systems. In the last decade, less than 10 nm resolution capability by these maskless lithography techniques has been repeatedly reported [58-60].

Electron microscope equipped with pattern generator modules enables nanoscale patterning within desired areas. The Nanometer Pattern Generation System (NPGS) is one of the popular SEM (Scanning Electron Microscope) lithography system that provides a powerful, versatile and user-friendly system for doing advanced EBL or

ion beam lithography using a commercial SEM, Scanning Transmission Electron Microscope (STEM) or Helium Ion Microscope (HIM) [61]. According to ITRS roadmap, the key challenges for these maskless technologies is to build a pilot tool for patterning the entire wafers with a chip like patterns and overlay control. The earliest insertion of such kind of technology is expected in 2021, and the target would be the '5 nm' logic node [1].

2.3.3 Advantages and disadvantages

Electron beam and focused ion beam lithography have advantages of high resolution, high density, high sensitivity, and high reliability. As these techniques are maskless, they are the ideal tools for flexible generation for low volume applications. Due to their intrinsically high resolution, excellent pattern definition can be achieved. They are highly automated and very accurate control of pattern with direct writing. EBL has a greater depth of focus and an excellent choice for the formation of masks and templates for optical lithography and nanoimprint lithography. On the other hand, it has the drawback of low speed and low throughput. It is a complicated and expensive system, as well. It also suffers from scattering and overexposure problems, which cause pattern distortion. During the lithography process, the electrons can be scattered (forward and backward) that broadens the diameter of the electron beam. Hence, these wider electron beams produce the wider nanostructures and degrade the resolution of the system. Moreover, they can also add more exposure to the adjacent feature, which initiates overexposure problem. Hence this method is not efficient for industrial processing.

2.4 Nanoimprint lithography

2.4.1 Mechanism

Nanoimprint lithography is an advanced nanofabrication method that is capable of high-throughput patterning of nanostructures with high resolution (down to the 3 nm regime). Because of the low cost, reduced process steps, and high fidelity, NIL became an attractive technique for a wide range of optics and electronics applications. Nanoimprint lithography methods can be classified into three categories: thermal-NIL, UV-NIL, and laser-assisted NIL. The basic steps of the NIL process are shown in Figure 2.3.

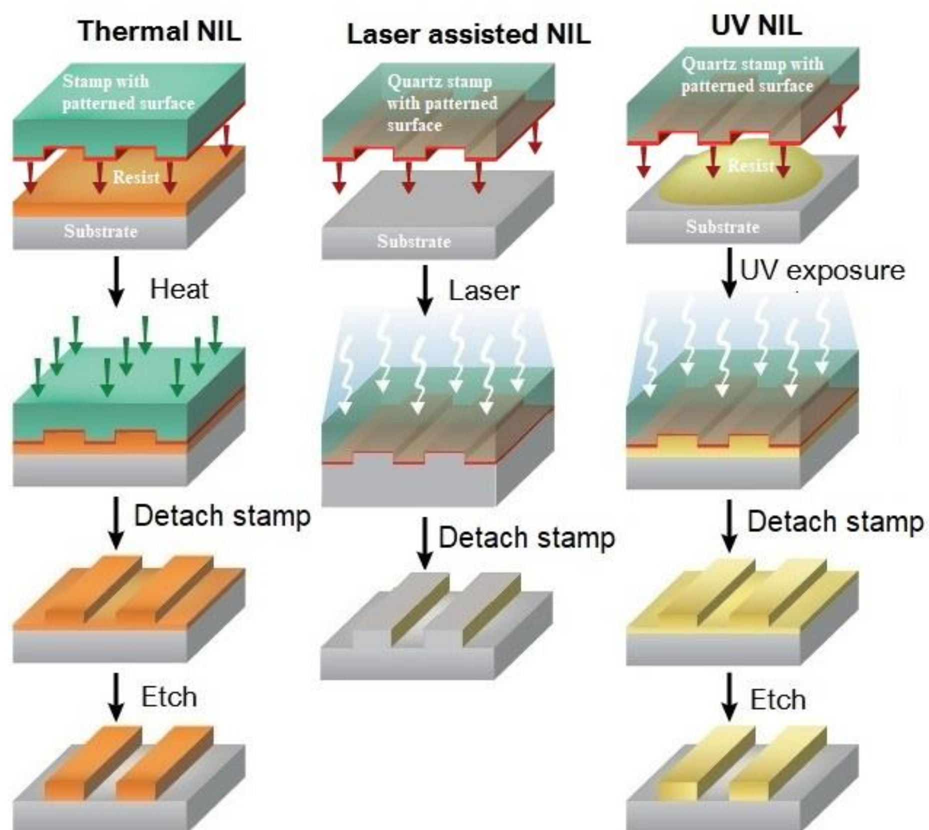

Figure 2.3 Basic NIL process steps.

In thermal NIL, a thin film of a thermoplastic polymer (imprint resist) is deposited first by spin coating onto the substrate. The next step is to press the prefabricated stamp with the substrate together under an absolute pressure. Subsequent heating is used above the polymer's glass transition point to achieve the softened polymeric film. In the post thermal cooling process, the substrate is cooled down, and the stamp is removed from it while keeping the pattern resist on the substrate. Finally, an etching process is used to remove the resist residual layer. Youn *et al.* described a thermal roller NIL approach where the stamp is connected with two moveable springs through the pullers [62]. Replicating of ultra-precision micron-scale structures can be achieved with this thermal roller imprinting process at the scan speed of 0.1–10 mm/s. For thermal NIL, pattern stability is a critical issue, which is related to internal stress relaxation at the glass transition temperature of the polymer after imprinting. As this issue limits the throughput, UV-NIL became more suitable over thermal NIL for mass scale patterning applications.

UV-NIL is a low-pressure at room temperature imprint technique, which involves the coating of the sample surface with a UV-curable liquid resist. The resist material is exposed to the UV light and the subsequent solidification of the resist under UV radiation. Afterward, an optically transparent stamp is pressed into the substrate to extract the patterns. Canon’s latest NIL system uses Jet and Flash imprint lithography (J-FIL), which involves field-by-field inkjet deposition of a low viscosity UV curable resist fluid on the substrate. The tool dispenses up to 100,000 picoliter drops over a field of 26 mm × 33 mm. The importance of inkjet and similar sophisticated dispensing is to give a variable loading appropriate for the local density of raised features on the stamp. This gives a continuous residual layer of uniform and

minimal thickness. Then the mask with a relief structure is aligned to the substrate. Shaping the mask with a ~10–15 μm bow using air pressure is the next step. Then, vertically moving actuators are used to relax the mask bowing. After the resist filling, it goes under UV radiation. Lastly, etching is performed just after the separation of the mask from the substrate.

The laser-assisted direct imprint (LADI) is a resistless technique that does not require etching. With this technique, a single excimer laser pulse is exposed through the transparent quartz stamp to melt a thin surface layer of the silicon substrate. Then, the resulting liquid layer is embossed by the quartz stamp. Finally, the stamp is released after the substrate has cooled down. Various nanostructures with sub-10 nm resolution could be imprinted into a silicon wafer using LADI with the embossing time below 250 ns. The capability of high-resolution and high-speed patterning make the LADI as a promising technique for a variety of applications, and it can be extended to other materials (polysilicon, Ge, and dielectrics) and processing techniques.

2.4.2 Status and challenges

Some challenges have prohibited NIL from being adopted on a larger scale, such as defectivity, contamination, throughput, overlay, and mask life. Cost benefits also depend on the improvement of these parameters. Defectivity plays a significant role in meeting the cost of ownership (CoO) requirements. Defectivity in the NIL process includes non-filled defects, solid-phase defects during the separation process, and particle related defects. Non-filled defects are formed due to the contamination of the underlying adhesion layer. Another reason for these defects is shorter resist spread times. Therefore, the increased fluid filling time leads to a decrease in defect density.

In 2018, a defectivity of <1pcs/cm^2 has already been reported for the 2x nm HP L/S structures [63].

During the separation process, shear forces imparted between the mask and wafer can slit the feature. Careful controlling of the system during separation can mitigate these defects. To reduce the particle defects, which are located on the wafer and mask, some approaches have already been taken. Manufacturers usually use ceramic materials to reduce particle generation, which eventually produces more particles. Therefore, surface treatment methods (polishing, coating, and heating) have been applied to solve this problem. The relative particle generation is reduced to 0.3% for the heat treatment, 0.4% for coating, and 1.4% for proper polishing [64]. These types of methods are also applied to all relevant materials within the tool.

Takahiro Nakayama *et al*. demonstrated a particle reduction method introducing an air curtain system [64]. With proper optimization, the curtain system can reduce the particle generated on the wafer to 0.003 pieces/wafer. However, additional polishing and cleaning methods were applied to drive particle reduction down to 0.0008 pieces/wafer. In 2018, some methods for in-situ particle removal, mask neutralization, and resist filtration have been discussed [65]. Their result shows the particle counts on a wafer reduced to only 0.0005 pieces per wafer path or a single particle over 2000 wafers.

It is essential to minimize the formation of hard particles to extend the mask life as they can create permanent defects in the mask. Mask life of more than 80 lots was demonstrated by suppressing the particles [65, 66]. Recently, a study has been carried out on auto wafer chuck cleaning and electrostatic cleaning plate mask neutralization, which showed an improvement of the mask lifetime to >300 lots [66]. Moreover, mask

replication can be useful to increase the mask lifetime. By using the J-FIL-based mask replication tool, a master mask created by e-beam can be duplicated to create replicas inexpensively. For example, one e-beam master being used to make 4100 replicas, followed by each replica patterning 41000 wafers, leads to an equivalent master mask life of 4100 000 wafers. Several companies such as Molecular Imprints Inc., Canon Corporation, and DNP have developed mask replicators and demonstrated their ability to meet resolution, pattern uniformity, image placement, and defect requirements [67].

One of the critical issues for NIL is high overlay accuracy. Generally, the current devices now require an overlay of better than 4 nm, 3 σ. For the demanded overlay accuracy, many technology enhancements are required, such as the improvement of overlay control accuracy, image placement accuracy, and mix & match technique. Hayashi *et al.* demonstrated that 3.2 nm crossed matched machine overlay (XMMO) and 2.4 nm single machine overlay (SMO) can be achieved by using CANON's NIL system [68]. This system employed the mask magnification and shape control system (MSCS), the interferometric Moiré alignment technology (i-MAT), the precision x–y–θ air-bearing stage, and the high order distortion correction (HODC) system which have allowed better overlay performance. The overlay correction has already met the target, and further improvement can be possible by applying wafer chucks with better flatness specifications. In terms of image placement, an accuracy of 0.8 nm and 1.0 nm in X and Y alignment, respectively, has been reported by Hamaya *et al*. [69].

Several parameters influence the throughput of a nanoimprint system. One of the contributors is the resist fill time. By careful optimization of several parameters (resist drop volume, system controls, material engineering, design for the imprint, and

system controls), fill time can be decreased. In 2018, a throughput of 80 WPH was achieved by increasing the resist filling speed with improved resist and optimized resist drop arrangement [66]. Recently, a throughput of up to 90 WPH was attained with an FPA-1200NZ2C four-station cluster tool introduced by CANON, where they applied multi-field dispense technology [69]. A further enhancement is needed to catch up with the desired CoO, where spin-coating NIL and large field NIL can be promising solutions. In a spin-coating NIL, fast resist filling can be achieved with no bubble trapping, and there is no resist dispensing step. Therefore, it is expected to provide a throughput of more than 110 WPH with this method.

One of the major influences of NIL technology is the capability of large area printing, which is desirable for cost-effective high-volume manufacturing industries. Large area patterning with high density and high fidelity has been reported in the earlier reports [70, 71]. For high-resolution large area patterning, a roll-type UV-NIL process with a flexible transparent thin stamp has been proposed [72]. In the last few years, significant development of the high-speed roll-to-roll and roll-to-plate NIL apparatus for large area patterning of flexible substrates have been demonstrated [73-76].

NIL finally entered the mainstream semiconductor arena with Toshiba's installation of Canon's NIL system to produce planar NAND devices. The tool is capable of printing sub-10 nm feature sizes and has demonstrated 14 nm half-pitch patterning [66]. This system is now approaching to produce 3D NAND devices as well as next-generation memory types (storage-class) in the future. In 3D NAND, horizontal layers (memory cells) are stacked on top of each other and then connected using tiny vertical channels. 3D NAND requires some tricky patterning steps which are fit for NIL. Therefore, it can be an effective patterning method for 3D NAND

devices. In 2016, CEA-Leti and EV Group initiated a new program called INSPIRE to diversify the NIL applications beyond semiconductors [77]. To accelerate this technology adoption, Canon, Nanonex, Suss, and others continue to develop the NIL systems and deliver them for a range of markets, such as memory devices, nanophotonics, bio chips, solar cells, optical communication, pharmaceutics, and medicine.

2.4.3 Advantages and disadvantages

NIL is a fast and straightforward process. It offers a promising low-cost alternative lithography technology with some other advantages, such as high resolution, CDU, and smaller LER. Since it can be used to fabricate nanopatterns at a large scale in a short time, this can be a high-throughput technique. It also has a low cost of ownership and high-resolution extendibility. Nevertheless, NIL could offer its 3D patterning capability for the advancement of 3D chip technology. Because of its flexibility and ability to combine with other techniques, it has created enormous opportunities for future lithography techniques for many other potential applications. However, low overlay structure accuracy and thermal expansion effects are the disadvantages of the NIL. One of the drawbacks of NIL over other nanofabrication techniques is the flexibility of patterning. The stamp must be remanufactured when the designed pattern is changed slightly. Another disadvantage is the current reliance on other lithography techniques to fabricate the stamp that needs lots of money and time.

2.5 Directed self-assembly

2.5.1 Mechanism

DSA is one of the promising techniques for high-volume low-cost manufacturing at a sub-lithographic resolution. DSA enables finer resolution that attracted a great deal of interest from major semiconductor manufacturers. Recent developments in DSA materials and processing make it compelling next generation patterning techniques. There are two types of DSA processes: 'epitaxial self-assembly' (Chemo-epitaxy) and 'graphoepitaxy.' In epitaxial self-assembly, dense chemical patterns are employed to direct block co-polymer (BCP) self-assembly. Highly ordered nanopatterns can be achieved if the period of the surface chemical pattern is proportionate with the equilibrium period of the BCP self-assembled nanostructure. Graphoepitaxy guides patterning by topographical geometry for DSA. The selective wetting of a BCP component at the trench sidewalls enforces the lateral ordering of the self-assembled BCP nanodomains along the trenches. Thus, it improves the pattern density by subdividing the topographical pre-pattern. Figure 2.4 presents the schematic illustration of the two processes [78].

▪ Chemoepitaxy (chemical pattern)

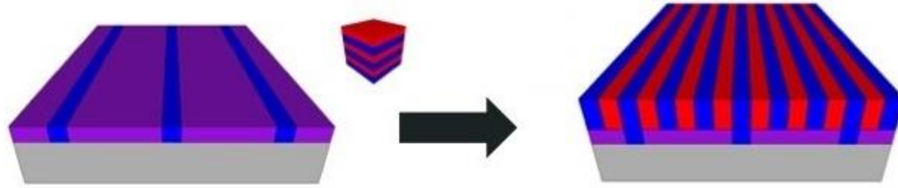

▪ Graphoepitaxy (topographic pattern)

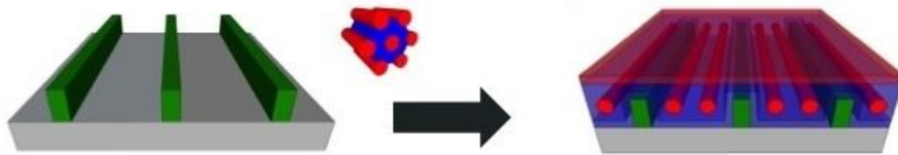

Figure 2.4 Schematic illustration of the DSA processes [78].

2.5.2 Status and challenges

DSA pattern defects, pattern uniformity, pattern placement accuracy, material quality control, cost, and ease of integration into manufacturing flows are the critical issues to adopt DSA technology on semiconductor manufacturing. Missing and bridge holes are the typical defect types of DSA holes in a physical guide. Researchers are also focusing on recognizing the factors that are responsible for assembly defects (dislocations and line-period bridges). The sources for these defects are the guide pattern mismatching, particles on the substrate, and chemical issues. Missing defects are related to the critical dimension and the surface affinity of the guide pattern, while the dislocation defects are associated with an insufficient bake process [79]. Pathangi *et al*. presented the 14 nm half-pitch DSA line/space patterning into the silicon substrate with reduced defectivity [80]. In 2017, it was claimed that a dense (pitch 120 nm) contact area superior to 0.01 mm^2 free of DSA related defects is achieved [81]. More

recent research also shows that less defectivity (<0.2 cm^{-2}) can be achieved with DSA [82]. Moreover, to improve pattern quality, some experiments have been performed on various etch mask materials and etch process conditions [83].

LER is another challenge of DSA line patterns. For HVM industries, the LER number should be about 10% of the target critical dimension. It has been suggested that the optimization of the pattern transfer process is one of the effective ways to improve the LER of the DSA pattern. By using this method, LER can be improved less than 2 nm [84]. Further improvement is required for the sub-10 nm patterning node. The interfacial length between the two domains influences the LER of DSA lines. Since it is related to the Flory-Huggins interaction parameter (χ) of BCPs, one solution to improve the LER could be the adoption of BCPs with a higher χ number. However, the high χ block copolymers are still not readily available.

Another issue of DSA of BCPs is the pattern density. Some pattern density enhancement approaches have been proposed, including the 'thermal flow process,' 'lift-off process,' and 'pattern trimming process' [85-89]. By utilizing a low-topography resist prepattern, ~5 teradot/in^2 dot arrays with long-range order have been demonstrated [83]. Highly ordered patterns using PS-b-PDMS have been reported in some publications [90, 91]. The χ of BSPs inherently determines the minimum feature size. High χ BCP, P2VP-b-PDMS has been reported that can generate 6 nm scale line/space patterns [91]. In 2017, a research group from the Argonne National Laboratory developed a new way to create some of the world's thinnest wires using the DSA process that could enable mass manufacturing with standard types of equipment [92]. Recently, a new chemo-epitaxy process (Arkema-CEA) has been introduced, which can overcome the resolution limitation of the current chemo-epitaxy

process. This process is based on sidewall image transfer (SIT) patterning and could produce low critical dimension and pitch that permits the high χ BCP integration [93].

DSA can also integrate bottom-up self-assembly with conventional top-down lithography. It can enhance the capabilities of other lithographic techniques that enable manufacturing at a drastically reduced cost. Researchers are investigating the possibility of hybrid DSA processes (a combination of both chemo and grapho elements), which can be possible alternatives for sub-5 nm process nodes. They have the potential to widen the area of applications for DSA. S. Morita *et al.* described a low-cost lithography process for making sub-15 nm patterns using DSA on a nano-imprinting guide [94]. Developments of several new processes have been reported, such as CHIPS flow [95], LiNe process [96], SMART™ process [97], and COOL process [98].

However, several application fields for DSA other than semiconductor device process such as flexible/transferable DSA technology utilizing chemically modified graphene (CMG) has been demonstrated [99, 100]. Several DSA consortiums (CEA-Leti, IBM and IMEC, Arkema, Brewer, EMD Performance Materials, TEL, TOK) are involved in a systematic investigation to integrate DSA effectively into commercial semiconductor process. However, further researches are required on process optimization, perfect defect control, effective pattern transfer, and relevant material development to make DSA capable of various commercial device manufacturing as a next-generation lithography solution.

2.5.3 Advantages and disadvantages

By DSA, the overall resolution can be increased to a level that is compatible with the 7 nm and 5 nm logic nodes. DSA could simplify and reduce the process steps. It can ease process integration and provide low-cost processing in advanced semiconductor processes. Moreover, reduced defectivity through material and process optimization, increased pattern fidelity, better material quality control at HVM, and high throughput are the other advantages of DSA. The block copolymers have defects repair tendency in the patterns manufactured by other photolithographic techniques. With this ability, DSA can play a significant role in the future of semiconductor fabrication. By DSA, it is possible to define the orientation, structural dimensions, and pattern density accurately. However, in terms of LER and CD control, DSA seems still to be well behind EUVL. Other disadvantages are defectivity, limited pattern types, a random orientation, and relatively long processing time.

2.6 Scanning probe lithography

2.6.1 Mechanism

Since its invention, the scanning probe microscopes (SPM) have become potential tools to fabricate nanostructures with atomic scale accuracy. SPM based lithography techniques can be used to process a variety of materials such as metals, semiconductors, polymers, and biological molecules, while the system operates in liquid, air, or vacuum. Moreover, they can perform a variety of physical and chemical modifications, such as thermal interactions, electric field-induced reactions, electrochemical reactions, thermochemical reactions, mechanical forces, or deposition of ink. Based on these interactions, four major lithography methods have been

successfully developed: mechanical SPL, thermomechanical SPL, oxidation SPL, and dip-pen lithography.

Mechanical SPL (m-SPL) is one of the simplest mechanical techniques for the removal of material through plowing and cutting (Figure 2.5a). The first step is the positioning of the tip in a specific region of the sample. A force is applied on the tip then, which causes a slit in the sample, thus creating the desired nanostructure. By controlling the tip's path through the sample, complex nanostructures can easily be fabricated. The amount of force required for these techniques depends strongly on the material properties of the substrate. Another approach based on mechanical lithography that minimizes the applied force is the thermomechanical SPL (t-SPL). In this technique, a heated tip is used to weaken the sample surface, thereby reducing the force necessary to fabricate the nanostructures (Figure 2.5b). Using silicon substrates covered with a polymethyl methacrylate (PMMA) film, it has been possible to generate structures of a size between 10-50 nm.

The oxidation SPL (o-SPL) technique is based on local anodic oxidation reactions (Figure 2.5c). When an electric field is applied between the tip and the substrate, a water bridge is formed between them. This water bridge acts as the electrolyte providing the oxyanions needed for the oxidation reaction. The size of the produced oxide structures can be controlled by the lateral confinement of the electric field within the water bridge. Hence, it is possible to generate structures with dimensions smaller than 10 nm.

Dip-Pen lithography (DPL) is a direct writing technique in which the tip is submerged first in a solution containing molecules or ink (Figure 2.5d). Then the ink-coated tip is used to create motifs on a sample surface. Molecular transport from the

tip to the sample surface is carried out by the water bridge present between an atomic force microscope (AFM) tip and a surface under normal conditions. Unlike other methods, DPL can manufacture nanostructures below 15 nm in size, providing simple control over the sizes and geometries of the structures.

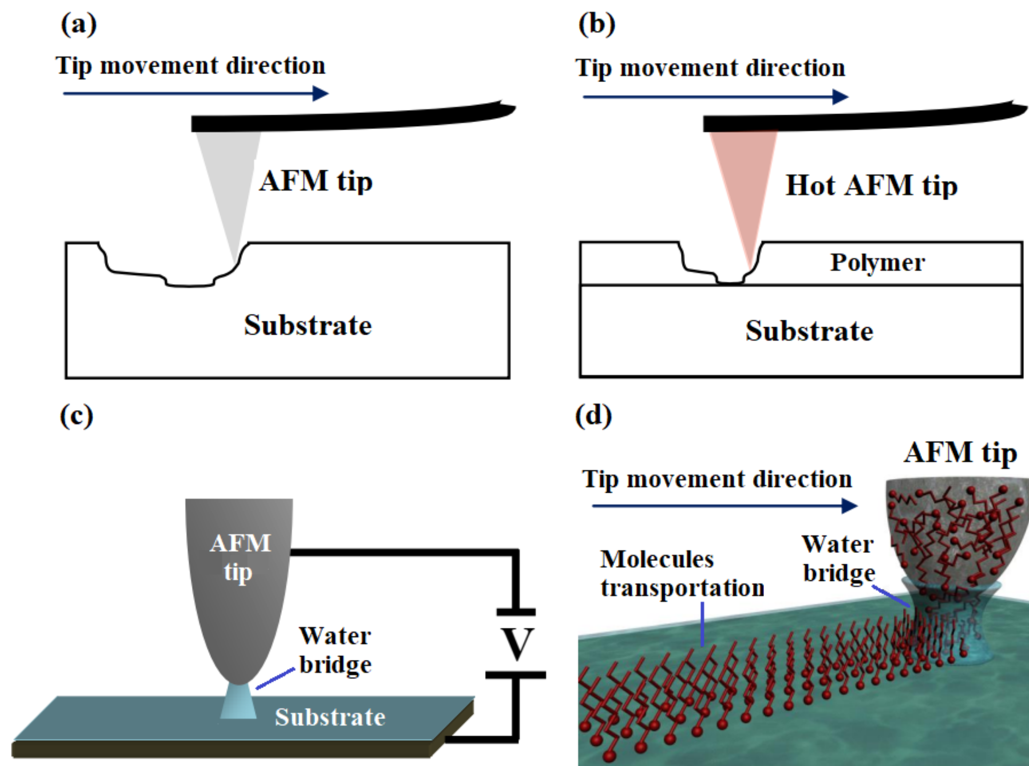

Figure 2.5 Outline of the SPM lithography processes. (a) m-SPL. (b) t-SPL. (c) o-SPL. (d) DPL.

2.6.2 Status and challenges

SPL methods are widely used in patterning metals, semiconductors, and polymers. Many scholars initially employed the existing AFM system to fabricate 2D arbitrary nanostructures by controlling different feedback gain and scanning speed. For example, Hyon *et al*. achieved a sub-20 nm width nano line with nearly 1 nm depth on the GaAs surface [101]. Wendel *et al*. successfully manufactured 16 nm holes array

with 55 nm periodicity on GaAs/AlGaAs substrate in ambient conditions [102]. Afterward, Schumacher *et al.* continued to use this approach to machine GaAs/AlGaAs heterostructure with 50 ~ 100 μN contact force under 100 μm/s scanning speed for obtaining a channel barrier and insulated gate [103]. These works opened the application market for single-electron transistor fabrication with single-gate and quantum electronic nanocomponents integration production. This approach can also be integrated with other nanolithography techniques, such as lift-off process, wet chemical etching, and dry etching. Notwithstanding, it is harder to realize the kind of complicated 2D and 3D nanostructures fabrication with the simple AFM platform. Because of this, some researches were performed by incorporating the high-level control system into the commercial AFM system to accomplish the complicated 2D and 3D nanostructures [104 -107].

The thermomechanical SPL was employed first for data storage applications [108]. Up to date, they were utilized to fabricate a wide variety of materials [109-118]. This method was used to create 55 nm pitch nanostructures on the silicon substrate with high resolution and low LER [119]. Furthermore, Ryu Cho *et al.* revealed the optimal mechanical force to be 25 ± 6 nN and the best tip temperature to be 550−700 °C during fabricating nanopatterns on a silicon substrate [120]. Besides, a hybrid method was employed, combining thermomechanical SPL and laser machining, to obtain a single-electron transistor with a 50 nm insulated gate [121].

A lot of o-SPL researches focuses on the processing of functional devices. In 2010, R. V. Martinez *et al.* utilized o-SPL to accomplish a single crystal silicon FET (field effect transistor) using a nano line with a width of 9.5 nm [122]. The nano line transistor has succeeded in immunological examination application, and the on/off

current ratio is up to 10^5. Later, many researchers investigated the applicability of this method for transition metal dichalcogenides application. Espinosa *et al.* carried out the fabrication on MoS_2 substrate and obtained a 200 nm nanochannel successfully [123]. Their results show that the conductive channel can be downscaled from micrometres scale to nanometres scale without weakening the overall conductivity of the MoS_2.

Besides, the transistors depending on MoS_2, have had a wide application in the non-volatile memory cells [124] and medical biosensors for cancer sensitive identification [125]. Dago *et al.* also obtained nanostructures of 1 nm height and sub-20 nm width on the multiple layers of WSe_2 [126]. These results indicate that the o-SPL is a straightforward approach for the 2D transition metal fabrication. Lorenzoni *et al*. studied the possibility of 3D fabrication with o-SPL. They obtained an array of nanodots with a high aspect ratio on 6H-SiC substrate via changing voltages up to 10 V and selecting different pulse times [127]. Their results illustrate the new fabrication possibility for 3D nanostructures. Furthermore, the o-SPL was successfully used to embed the nanoparticles into the SiO_2 layer [128].

Since the first invention of DPL by Piner *et al.* [129], this technique became a versatile and powerful platform to pattern and functionalize a surface. The applicability of this process was extended over time by introducing the input of electrical, thermal, and mechanical energy. The introduction of electrochemical dip-pen nanolithography (e-DPL) facilitates the patterning organic small molecules. This method was employed to fabricate conductive nanostructures, such as poly(thiophene) nanowires on semiconducting and insulating surfaces [130], gallium nitride/gallium oxide heterostructures [131] and immobilization of biological molecules (Histidine-tagged proteins) on a metallic nickel surface [132].

In 2006, Nelson *et al.* used thermal DPL to obtain the sub-80 nm indium metal lines on the glass substrate mixed with borosilicate [133]. This technique provides a novel approach for circuit repair. Similarly, these methods have been utilized to pattern the Fe_3O_4 nanoparticle composites [134] and graphene nanoribbons [111]. Besides, it was revealed that the ink transport and feature size could be controlled by changing the tip temperature [135]. Moreover, DPL has undoubtedly been developed to be multiplex [136]. Chen *et al.* have developed a precursor for the formation of multi-metallic nanoparticles downscaling to the nanometer level [137]. They exploited the PEO-*b*-P2VP as the matrix carrying the five kinds of the metal nanoparticle to create sub-10 nm polymetallic alloy hemisphere nanostructures.

Although the SPM based lithography methods have demonstrated remarkable nano-fabrication capabilities, they must overcome some challenges to improve throughput and productivity. In order to enhance the processing efficiency, extensive efforts have been made to enable them for parallel processing [138, 139]. Minne *et al.* [140] proposed an o-SPL system to operate an array of 50 cantilevered probes in parallel at high speed. IBM developed a data storage system using this concept, called Millipede, which could be achieved with a depth of 1 nm and with a spacing of 18 nm between tracks and 9 nm within a track, leading to a storage density of more than 1 Tbit/in.^{2} [141].

In 2006, DPL demonstrated parallel operation by using an array of 55000 tips over one square centimeter area [142]. Besides, this parallel operation helps to fabricate multiplexed patterns. However, the scale-up of a typical single-cantilever AFM system to large cantilever arrays faces some difficulties due to the complexity in the optical set-up, signal processing, and restrictions on cantilever geometries [143].

The integration of actuators and sensors into the individual cantilevers is required to implement the fully controlled parallel systems.

Indeed, the multi-probes systems are complicated than a single probe system. The software and hardware compatibility, array architecture, control strategy, and instrumentation requirements are the main factors that should be taken into consideration [144]. Furthermore, to make them suitable for the industrial application, some other limiting parameters, such as the interference of each probe, reliability of a large number of probes, the pattern uniformity, and the resulting high processing temperature need to be improved.

Although a substantial number of researches has been carried out to overcome the roadblocks for achieving the wide-area-operation high-speed AFM system [145, 146], more effort still be needed to realize innovative high-speed AFMs for industrial uses. Another challenge is the feature size dependency on the probe dimension. The lateral width of the nanostructures is confined to the tip radius, and it is challenging to achieve a smaller size. Sharp tips can be used to overcome this problem. However, these sharp tips introduce tip-wear problem during the machining process and do not help to improve the processing efficiency. Therefore, the achievement of the smaller features while ensuring the improved processing efficiency is a thought-provoking question to realize industrial-scale production.

2.6.3 Advantage and disadvantage

SPL methods are simple, direct, and possesses excellent control ability. They can be performed under the conditions of ultra-vacuum, atmosphere, liquid, low temperature, ambient temperature, and high temperature. They do not require

complicated machines. Moreover, thermal SPL methods can effectively reduce tip wear. Nonetheless, the limitations of these methods are the lifetime and the stability of the tips. The oxidation process is simple, and the achieved oxide material has the characteristics of insulation and corrosion resistance and thus can be compatible with the existing nanoelectronics machining process.

Despite material patterning diversity, the o-SPL methods require the samples which are highly oxidizable. In addition to that, it is difficult to obtain large-area high-accuracy nanostructures due to the drift, hysteresis lag, and nonlinearity problems of the piezoelectric actuator of the SPM itself. The DPL can deposit not only a variety of nanoparticles and nanocomposites but also is a real maskless nanofabrication approach. This method is versatile in terms of ink or substrate materials. It can fabricate complex multi-component assemblies without any cross-contamination [147]. Moreover, the feature size is independent with the tip speed and the contact force. Nevertheless, the main drawback is the slow processing speed when they use for patterning of large areas.

2.7 Nanoelectrode lithography

2.7.1 Mechanism

Nanoelectrode lithography is a resistless nanoimprinting approach that uses a conductive stamp with nanostructures. Under a humid environment, a voltage is applied between the stamp and the target substrate. Once the surfaces of the stamp are in contact with the substrate, current flows between them. The intense electric flux from the protrusive parts of the stamp to the substrate results in anodic oxidation of the substrate surface corresponding to the protrusive parts of the stamp with the

moisture present between the stamp and the substrate. Subsequently, the substrate is etched to achieve nanostructures like other methods. The NEL process is illustrated in Figure 2.6.

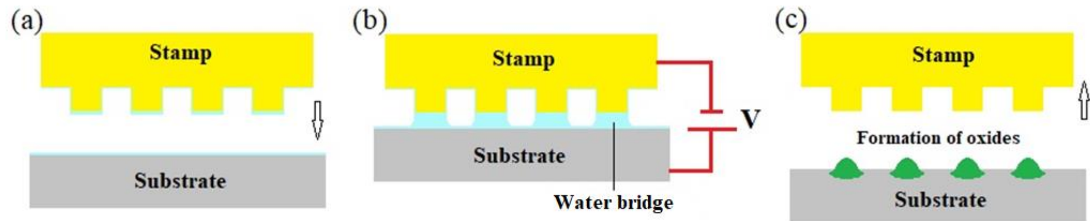

Figure 2.6 Diagram of the NEL process steps.

A number of studies have suggested possible oxide-growth mechanisms of the NEL process involves some physical and chemical processes, such as condensation, electric field effects, ionic transport, water dissociation, and oxidation. In the humid environment, a significant amount of water molecules is adsorbed on both stamp and substrate surfaces. When the surfaces of the stamp are in contact with the substrate, the vicinity of both surfaces can trigger spontaneous capillary condensation, and a water bridge is formed between them [148]. The diameter of the bridge can be several hundreds of nanometers. The water bridge provides the oxygen species, which is necessary for the oxidation process. It also facilitates the pathway for the electrical field to induce the oxidation.

The applied electric field also influences the formation of the bridge. Generally, a positive voltage (continuous or pulse) is applied between the substrate and the stamp. The strong electric flux from the protrusive parts of the stamp to the substrate results in the decomposition of water molecules into oxyanions (OH^-, O^-) and protons (H^+). These ions penetrate the substrate to form an oxide film on the surface. The possible oxidation reaction mechanism has been proposed by Sugimura

et al. [149]. At the anode (surface of the sample) the oxidation is carried out according to the following reaction:

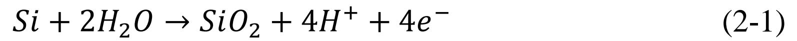

$$Si + 2H_2O \rightarrow SiO_2 + 4H^+ + 4e^- \quad (2\text{-}1)$$

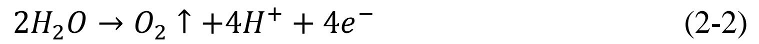

$$2H_2O \rightarrow O_2 \uparrow + 4H^+ + 4e^- \quad (2\text{-}2)$$

Meanwhile, the generation of hydrogens occurs at the cathode to complete the electrochemical reaction:

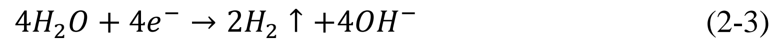

$$4H_2O + 4e^- \rightarrow 2H_2 \uparrow + 4OH^- \quad (2\text{-}3)$$

Reaction at water:

$$4H^+ + 4OH^- \rightarrow 2H_2O \quad (2\text{-}4)$$

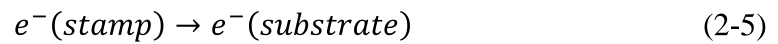

$$e^-(stamp) \rightarrow e^-(substrate) \quad (2\text{-}5)$$

Moreover, the same oxidation mechanism has been proposed in some other studies as follows [150-152]:

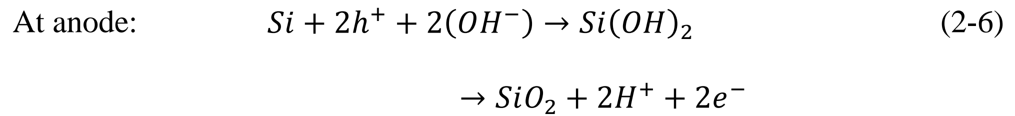

At anode: $$Si + 2h^+ + 2(OH^-) \rightarrow Si(OH)_2 \rightarrow SiO_2 + 2H^+ + 2e^- \quad (2\text{-}6)$$

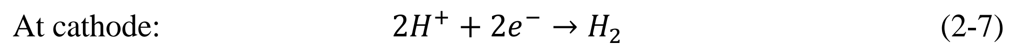

At cathode: $$2H^+ + 2e^- \rightarrow H_2 \quad (2\text{-}7)$$

For a GaAs substrate, the proposed chemical reactions are shown below:

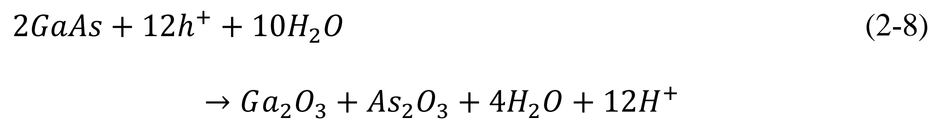

$$2GaAs + 12h^+ + 10H_2O \rightarrow Ga_2O_3 + As_2O_3 + 4H_2O + 12H^+ \quad (2\text{-}8)$$

Therefore, the general reaction mechanism for a metallic surface is proposed as:

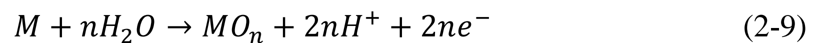

$$M + nH_2O \rightarrow MO_n + 2nH^+ + 2ne^- \quad (2\text{-}9)$$

To understand the reaction mechanism, a schematic model was proposed by Bloeß *et al.* [153]. This model shows the two major parts: water supply and water consumption (shown in Figure 2.7).

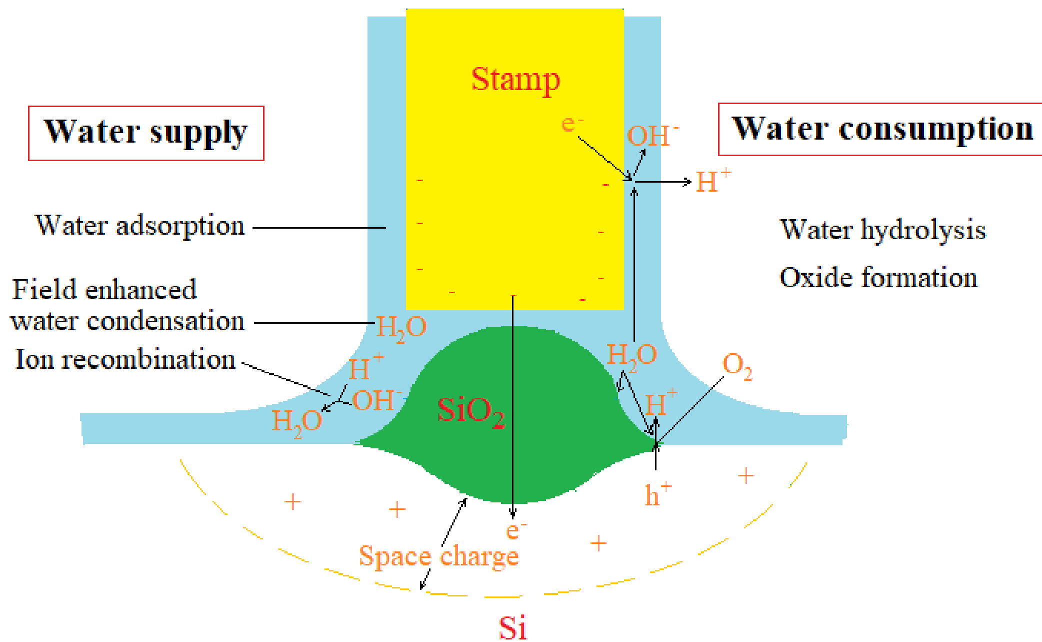

Figure 2.7 Schematic of the oxidation nanocell [153].

The electric field can induce the water condensation, and the water molecules are decomposed into protons (H^+) and oxygen gas (O_2). The hydrolysis of the water also produces the hydroxide ions (OH^-) in the bridge. As there is a small gap between the stamp and the substrate, it is expected that the H^+ and OH^- ions generated from reaction 2.1-2.3 can recombine spontaneously. However, for the same reason, direct electron tunneling (reaction 2.5) has also to be considered during the initial states of nanooxidation. The electric field drives the hydroxide ions to the Si/SiO_2 interface and then reacts with the holes to produce silicon dioxide, SiO_2.

2.7.2 Status and challenges

After the first demonstration of the NEL process by Mühl *et al.* [154], many pieces of research have been performed to make this technology viable for nanofabrication applications. R. Garcia's group and A. Yokoo's group performed

some initial experiments in 2003 and successfully transferred the pattern on a silicon substrate using a SiC stamp (shown in Figure 2.8a) and polycarbonate stamp (shown in Figure 2.8b), respectively [4, 5]. They also confirmed that fabricated oxide patterns could work as a mask, and nanostructures can be achieved by applying wet and dry etching (shown in Figure 2.8c, d).

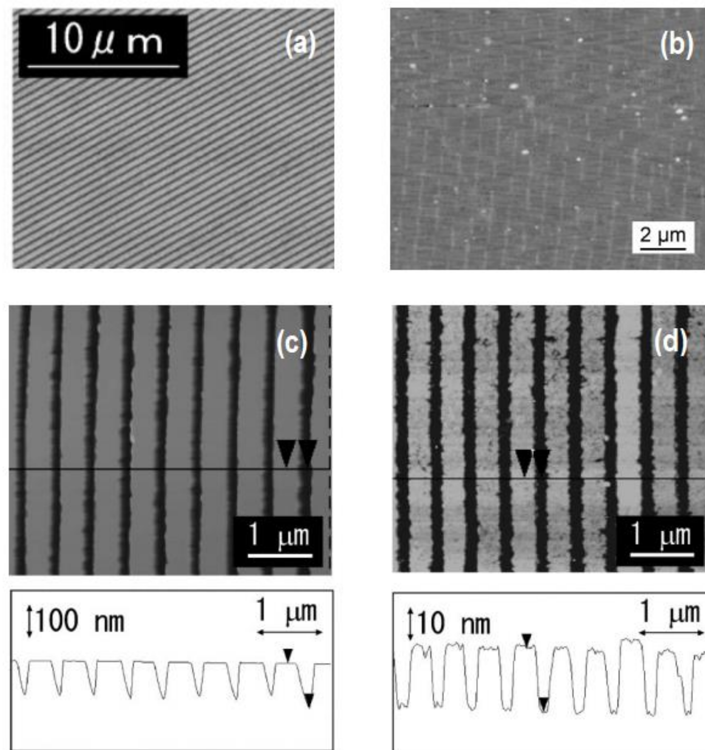

Figure 2.8 (a) SEM image of silicon substrate after oxidation using SiC stamp [5]. (b) SEM image of silicon substrate after oxidation using a DVD stamp [4]. (c) AFM image and the profile of a silicon surface after KOH etching. (d) AFM image and the profile of a silicon substrate after dry etching using fluorocarbon gas.

Since then, a few studies have been carried out to investigate the mechanism and to explore the new application areas. Albonetti *et al.* performed XPS measurements (Mg Kα source; hν = 1253.6 eV) to identify the chemical composition on the silicon sample after anodic oxidation and compared the changes with a native

oxide silicon sample [7]. Their experiment confirmed the presence of C, O, Si, and SiO_2 at the oxidized silicon surface (shown in Figure 2.9). The presence of carbon on the surface is because of the contamination.

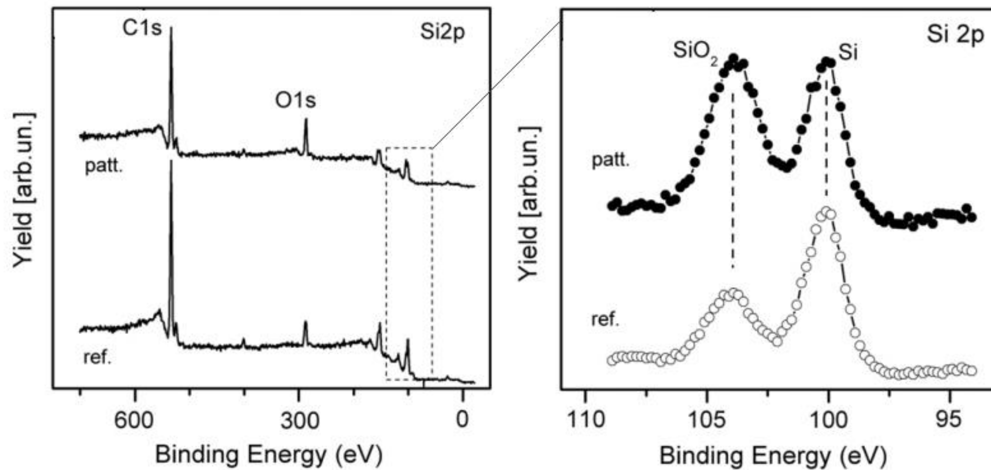

Figure 2.9 XPS spectra measurement [7].

Some kinetic studies have also been conducted to examine the parametric effect on the oxidation process [5, 7]. They showed that the growth of the oxides has a linear dependency on the duration of the oxidation process and the relative humidity. Higher oxides are obtained with higher relative humidity and longer times. One of the advantages of the NEL method is revealed as reproducibility. The same stamp can be used so many times as it does not show any relevant degradation due to its breaking strength. Multiple patterns on different substrates have been realized by using two consecutive patterns on the same sample [7, 155]. The process was repeated with the same stamp rotated 90 degrees. Thus, a crossed oxide pattern was fabricated (shown in Figure 2.10).

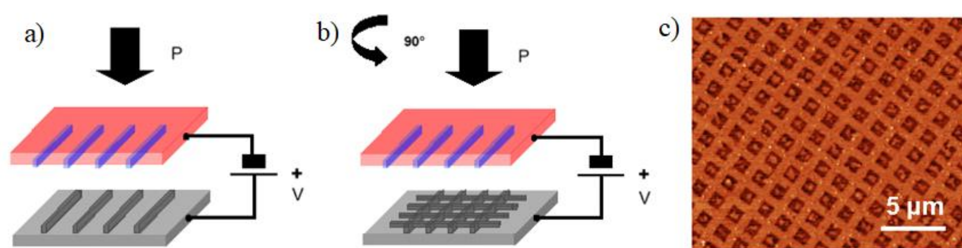

Figure 2.10 Process of multiple patterning [7]. a) First patterning. b) Second patterning. (c) AFM image of the pattern after two successive oxidations.

Nanoelectrode lithography can be sufficient in producing templates for the growth of molecular architectures such as sexithienyl [156], Tetrathiafulvalene [8], and antibodies [11]. Sexithienyl molecules (T6) were deposited onto arrays of parallel lines fabricated by NEL. Similarly, Tetrathiafulvalene (TTF) nanoparticles solution was deposited over the silicon oxide pattern, where electrostatic interactions drive the nanoparticles towards the SiO_2. Besides, the patterned pentacene surfaces by NEL have been used to preferentially binding of anti-BSA [11]. Some researchers also used this technique for the fabrication of controlled nanostructures of colloidal nanoparticles (gold) onto self-assembled monolayers (SAMs) [157, 158]. Therefore, controlled patterning of these molecules can effectively be achieved with this method (shown in Figure 2.11).

There are some challenging issues, such as misalignment and uniformity, that need to be solved. Losilla *et al.* suggested that the oxidation process could be enhanced by inserting a thin polymer layer between the stamp and the sample surface [8]. This polymer film (PMMA) is deformed under an external load, adapting the gaps to obtain a homogeneous pressure over the entire surface. Therefore, it improves the uniformity and increases the life of the stamps. They also showed that the best result was obtained with a 25 nm film of PMMA (shown in Figure 2.12). Another approach has been

proposed to improve the pattern uniformity, where flexible conductive molds (FCMs) are used [6]. FCMs were made of flexible insulating patterns with the metal film deposited on top of them. Successful pattern transfers were achieved on both uneven surface and flat surface with these stamps, which also showed improved transfer uniformity.

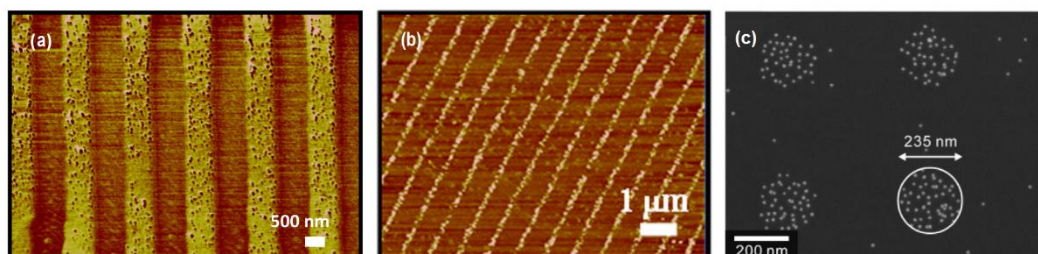

Figure 2.11 AFM/SEM images of Template growths. (a) deposition of the TTF derivative [8]. (b) deposition of anti-BSA antibodies [11]. (c) Au nanoparticle arrays [158].

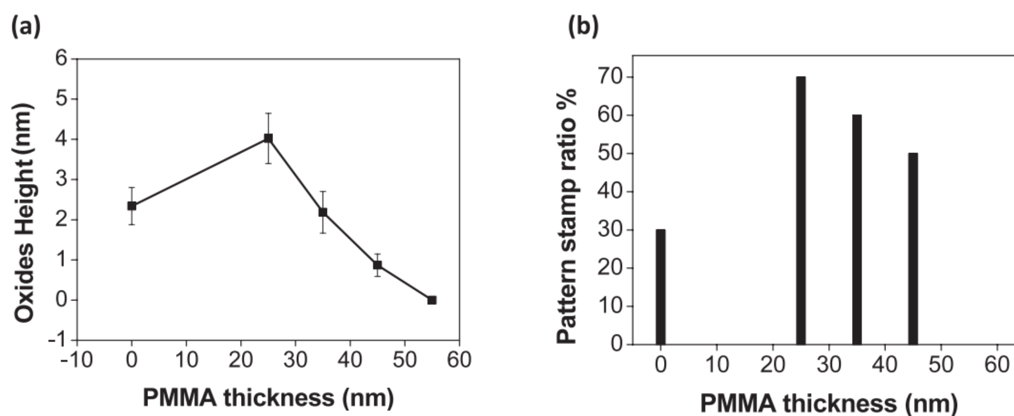

Figure 2.12 (a) Variation of oxide height with the thickness of the PMMA layer. (b) Percentage of the patterned area as a function of the PMMA thickness [8].

2.7.3 Advantages and disadvantages

As the NEL process is capable of generating three important elements: dielectric barriers, masks and templates or patterns, a wide variety of electronic and mechanical nano-devices can be manufactured with this technique. In addition, the NEL process can be beneficial to be used in combination with other methods, such as photolithography, electron beam lithography, or chemical etching processes for device manufacturing. Moreover, a long list of devices has already been manufactured by the local oxidation process, including storage memories, conductive nanowires, field effect transistors, single-electron transistors, generation of localized quantum dots, microlenses, patterns for the growth of biomolecules and conjugated materials and masks resistant to specific etching. Therefore, the NEL process could be a promising technique to manufacture these devices.

Nevertheless, the main drawback of this method is the requirements of electrically conductive stamps and samples, which are oxidizable. Although the NEL process is much faster than the other oxidation process, the throughput is still limited due to the size of the stamp. Besides, the use of larger stamps arises some challenging issues, such as uniformity and parallelism.

2.8 Comparison

Table 2.1 summarises the comparison of the patterning capabilities for various lithography techniques. Each technique has its own strengths and limitations. Although these lithography techniques show the promising capability to meet future demand, they need further improvement in some aspects. In terms of resolution, most of the next generation lithography methods can achieve sub-10 nm resolution. Figure 2.13 reflects the throughput and resolution relationship of these nanofabrication approaches and compares them with current DUV photolithography.

Although EBL methods have relatively higher resolution, they are limited by low throughput. The lithography method for HVM require throughputs of more than 10^{12} μm^2 h^{-1} (>100 wafers per hour) [159]. Slow blanking speed is one of the major issues for the EBL's system speed, and the system complexity makes it difficult to improve. Though the recent improvement in parallel beam system (FLX-1200) increased the throughput, currently, it only manages to provide a modest throughput of 1 wafer per hour. Similarly, SPL techniques need to increase the throughput, possibly using a matrix of tips for parallel writing to be useful in industrial applications.

Again, the throughput-resolution relationship indicates the EUVL, NIL, and DSA techniques are getting closer to the industrial requirements. On the other hand, the NEL method still needs to improve both the throughput and resolution to meet future demand. Suitable design of the stamp protrusions and the excellent control of the distance between stamp and substrate could allow NEL to fabricate the nanostructures with sub-10 nm resolution. Also, a roller based NEL process could be a possible solution to increase throughput.

Table 2.1 Comparison of NGL techniques.

Items	EUVL	EBL	UV-NIL	SPL	NEL	DSA
Resolution (nm)	<10 [160]	<5 [161]	<10 [66]	<10 (m-SPL) [144] <20 (t-SPL) [163] <15 (o-SPL) [164] <50 (DPL) [159]	100 nm line width with 370 nm hf [5] 200 nm line width with 150 nm hf [169]	<10 [170]
Throughput (μm^2 h^{-1})	1.53×10^{13} [19]	$<9\times10^{10}$ with Mapper's FLX-1200 [53]	8.1×10^{12} [69]	$\sim2.4\times10^{3}$ (m-SPL) [165] 10^{5} (t-SPL) [144] $\sim10^{2}$ (o-SPL) [126] $<10^{4}$ (DPL) [166]	3×10^{9} [7] 5.4×10^{9} [5] 9×10^{10} [6]	1.35×10^{13} [171] 1.20×10^{10} [172]
Machining capability	2D, 3D	2D, 3D	2D, 3D	2D, 3D	2D	2D, 3D
Environmental conditions	High vacuum	Vacuum	High vacuum or ambient	Vacuum or ambient	Ambient	Ambient
Litho speed	Fast	Slow	Fast	Fast	Slow	Fast
Overlay (nm)	<2 [19]	≤ 5 [54]	<3 [68]	<5 [167]	---	<2 [173]
Defect density (cm^{-2})	<1 [14]	<1 [162]	<1 [63]	<1 [168]	---	<0.2 [82]
Principle	Chemical	Physical	Physical, Chemical	Physical, Chemical	Electrochemical	Chemical
Cost	Higher start-up cost	High	Low	Low	Low	Low

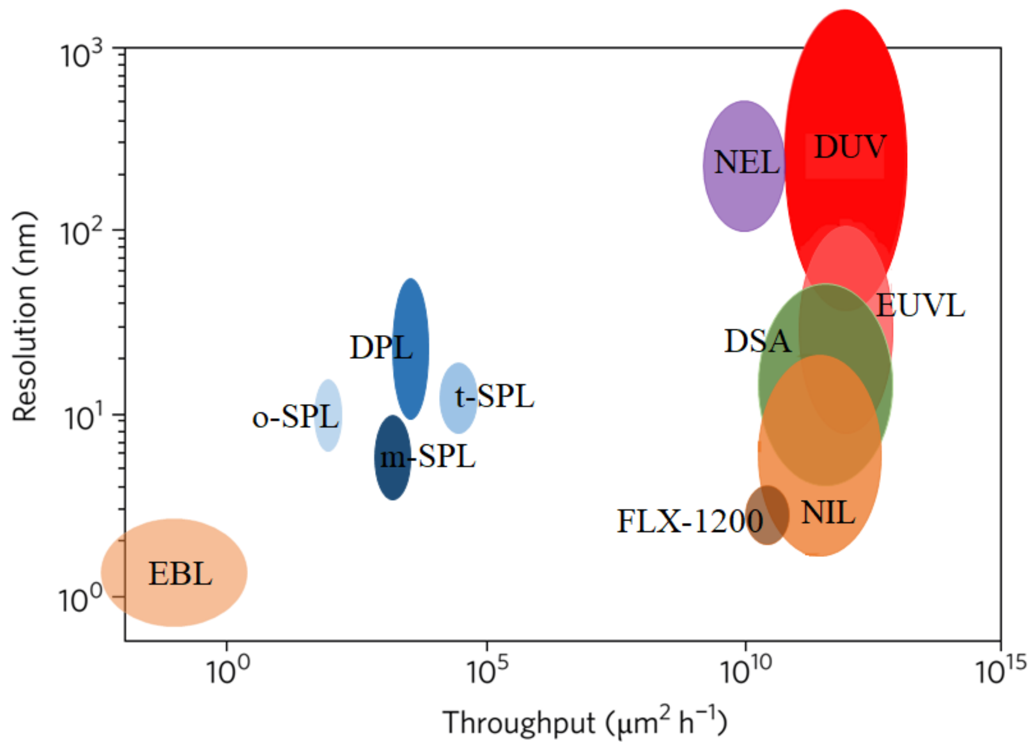

Figure 2.13 Resolution and throughput in nanolithography.

High overlay accuracy is one of the significant issues in NGL techniques. Within 2020, the required overlay is anticipated to be 3–4 nm for DRAM, flash, and logic devices [174]. All these lithography techniques can achieve an overlay accuracy of ≤5 nm. For better overlay accuracy, a lot of technology improvements are required, such as overlay control accuracy for tools, the metrology to precisely measure alignment and image placement accuracy.

However, the probability of defects increases with the enhanced resolution. Although it is difficult to improve defect density due to the contact nature in the NIL process, substantial researches are taking place to improve it close to the required value. Along with other issues, defectivity is still the main challenge to these techniques' implementation into various commercial device manufacturing situations as an NGL solution. In recent years, defect density in DSA has been improved

significantly from 24 defect-cm^{-2} to 0.2 defect-cm^{-2} [80, 82]. Improvements of defect density in all the techniques are still needed to meet the industrial requirement of 0.01 defects-cm^{-2}.

Finally, yet importantly, the deciding factor for the lithography techniques is its cost efficiency rather than its technical performance. EUVL infrastructure and tools are costly, and large numbers of mask steps required make the technique relatively expensive. Nonetheless, substantial researches are going on to make EUVL viable as a cost-effective manufacturing process. EBL lithography is also costly due to its expensive electronics. However, due to the widespread use of focused beams of charged particles for nanopatterning, these maskless lithography techniques are prevalent for lab-scale applications given its affordable cost. On the contrary, the process cost is relatively very low for DSA, NIL, and NEL processes. NIL currently realizes overall, a 28% cost advantage over ArFi lithography [175]. Therefore, NIL, NEL, and DSA are the promising low-cost techniques for future patterning nodes.

All the NGL technologies are in their development phases and still need further work. The extensive support from the chip makers and the substantial research investment put the EUVL slightly ahead of the other NGL techniques. Indeed, each technology is different and aimed at different applications. Therefore, a combination of tools and techniques could be the solution for future nanofabrication.

2.9 Molecular Dynamics simulation approach

Numerical methods are now widely used in the field of both basic and applied research. These methods essentially help to interpret the experimental data and understand the phenomena that are difficult to observe experimentally. The current improvement in capabilities of high-performance computing has strongly contributed

to the efficient calculation with unprecedented detail and accuracy at the atomic level. Molecular Dynamics (MD) has become one of the most effective computer simulation tools. It simulates the motions of particles by calculating their movement over time using the Newtonian laws of classical mechanics.

2.9.1 Principle of molecular dynamics

In 1957, molecular dynamics simulation was first used to study the macroscopic properties of materials by Alder and Wainwright [176]. After that, the molecular dynamics method has achieved great improvements and has been used significantly in many fields to simulate a number of thermodynamic and physical properties of solids, liquids, and gases. In molecular dynamics, the system is defined by the position of its atoms in the space. Numerical integration of Newton's second law of motion helps to obtain the information related to each atom. The law is presented as follows:

$$a_i = \frac{d^2 r_i}{dt^2} = \frac{F_i}{m_i} \qquad (i = 1, \ldots\ldots N) \tag{2-10}$$

where m_i is the mass of the atom, a_i is its acceleration, r_i is the position vector, and F_i is the force acting on it due to the gradient of the potential function and any other forces.

In the system, the atom's position and the initial velocity must be specified before starting the simulation. Generally, the initial position depends on the system structure, and the velocities are selected according to a Maxwell-Boltzmann distribution at the desired temperature. The first step of the simulation is to calculate the forces acting on each atom of the system. The source of the forces can be the

external force, electric field, and potential energy function. The interatomic bonding forces are defined by the appropriate potential energy function. Then, the equations of motion are integrated for each atom using a different algorithm, such as Verlet [177] or Leap-Frog algorithm [178]. Nowadays, the Verlet algorithm is commonly used for extremely short time intervals (1- 100 ps). The new positions and the velocities are updated for each atom of the system. The physical quantities of interest of the system, such as pressure, temperature, and energy, are calculated and saved. Finally, the iteration step moves forward, and the loop of the molecular dynamic can resume. A simplified schematic of the molecular dynamics' algorithm is presented in Figure 2.14.

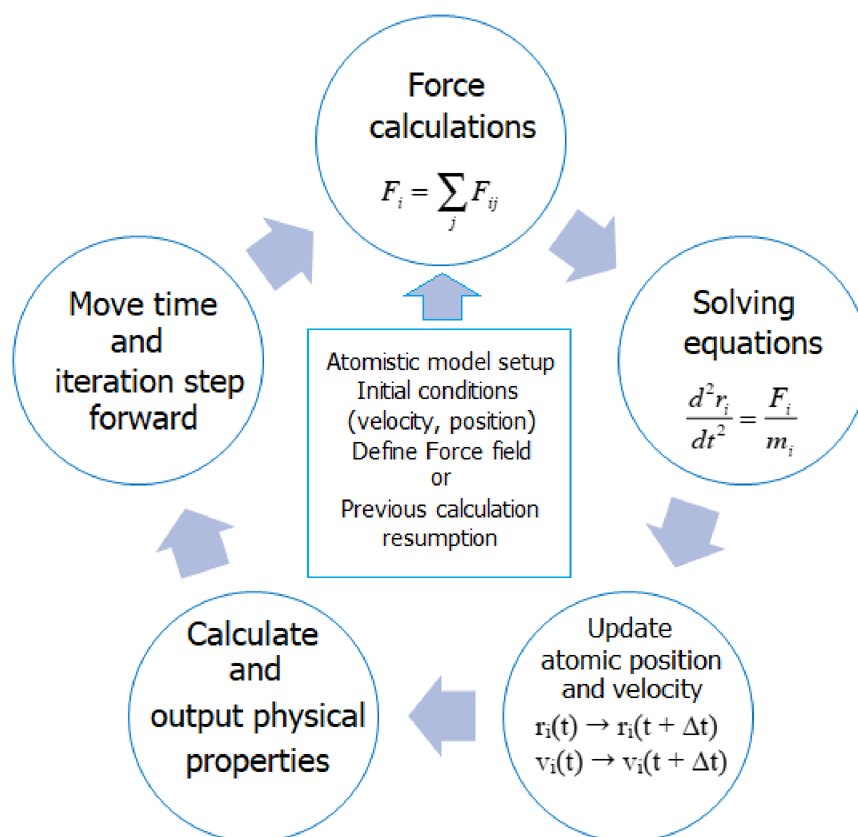

Figure 2.14 Schematic of molecular dynamics.

2.9.2 Ensembles

An ensemble is a collection of microstates of the system's molecules, which consists of different molecular states and an identical thermodynamic state. There are different ensembles with different characteristics. The commonly used ensembles are: the micro-canonical ensemble (NVE), the canonical ensemble (NVT), the isothermal-isobaric ensemble (NPT) and the isoenthalpic-isobaric ensemble (NPH), where N is the number of atoms, V is the volume, E is the energy, T is the temperature, P is the pressure and H is the enthalpy of the system. Ensemble NVE is used to represent an isolated system that has constant energy. It is achieved by solving the standard Newton's equations without any temperature and pressure control. On the other hand, ensemble NVT is obtained by controlling the thermodynamic temperature, where the system is no longer isolated but in connection with a heat bath or thermostat. There are several thermostats used in MD simulations such as Andersen thermostat [179], Berendsen thermostat [180], and Nosé-Hoover thermostat [181, 182]. The ensemble NPT permits control over both the temperature and pressure, whereas the ensemble NPH allows control over both the pressure and enthalpy of the system.

2.9.3 Boundary conditions

The appropriate choice of the boundary condition (BC) is essential in MD simulations. Due to the limited capabilities of computers, Periodic Boundary Condition (PBC) is the most effective BC method of simulating the atoms. It can represent a system with an infinite number of atoms by simulating only a small number of atoms. In PBC, the atoms can exit one end of the box and re-enter the other end so that the number of atoms in one cell remains constant. However, the PBC must be

utilized to both faces of a dimension. There are several non-PBCs such as fixed, shrink-wrapped, and shrink-wrapped with a minimum value. For shrink-wrapped boundary condition, the face position is set to incorporate all the atoms in that dimension (shrink-wrapping).

2.9.4 Potential energy function/force field

In molecular dynamics, the interaction between atoms is governed by a potential energy function. This potential energy function initiates the quantum interactions between electron shells, which necessarily implies the physical properties of the atoms. The potential energy function also determines the forces exerted on the atoms by calculating its gradient. Therefore, the choice of a potential energy function can affect the quality of the simulation results. Again, the simulation time also depends on the complexity of the potential function.

Table 2.2 shows a list of available MD potential energy functions that are successfully used in biomolecules, polymers, materials, chemistry, mesoscale, and hybrid systems. Pairwise empirical potential functions (Morse, Born-Mayer, Lennard-Jones potentials, etc.) are not able to reproduce the Cauchy pressure, which is a quantity that reflects the nature of the bonding at the atomic level of a material. To overcome this limitation, many-body potentials were introduced in the early 1980s. Some of them have already been used for silicon, such as Modified Embedded-Atom-Method (MEAM) [183], Stillinger-Weber (SW) [184], and Tersoff potential [185-188]. However, some potential functions provide more accuracy, but they are sometimes computationally very expensive.

Table 2.2 List of MD potentials.

Group	**Potentials**
Pairwise potentials	Lennard-Jones, Buckingham, Morse, Born-Mayer
Charged pairwise potentials	Coulombic, Point-dipole
Many-body potentials	Embedded-atom method (EAM), Modified EAM (MEAM), Embedded ion method (EIM), Adaptive intermolecular reactive empirical bond order (AI-REBO), Charge optimized many-body (COMB), Tersoff, Stillinger-Weber, Reactive force field (ReaxFF).
Coarse-grained potentials	DPD, GayBerne,
Mesoscopic potentials	Granular, Peridynamics
Long-range electrostatics	Ewald, PPPM, MSM
Implicit solvent potentials	Hydrodynamic lubrication, Debye force-field compatibility with common CHARMM, AMBER, OPLS, GROMACS options

Stillinger-Weber (SW) is one of the earliest potentials employed for a realistic atomic-scale simulation of silicon. It includes a linear combination of two- and three-body contributions to model the solid and liquid forms of silicon. Because of its simpler functional form, it behaves smoothly in the case of highly strained silicon [189]. However, it does not describe well several situations, such as the modeling of dislocation core structure [190, 191], the brittle-ductile transition in nanowires [192, 193], and the propagation of cracks. Besides, this potential cannot accurately generate amorphous silicon [194, 195].

The interaction framework was specially designed in MEAM potential so that it can combine various kinds of chemical elements, including metals and

semiconductors. Several MEAM potentials have already been developed and utilized for the atomistic simulation of silicon [196-199]. However, these MEAM potentials were proved insufficient to represent the properties of silicon accurately. This is due to the inadequate number of local geometries used in these potentials, and not considering the crystal stability [200].

The Tersoff is the most frequently used bond order potential for the silicon that has a relatively low computational cost. It can capture the essence of quantum-mechanical bonding and appropriately describe a wide range of structural properties such as lattice constant, elastic constant, and vacancy formation energy [201, 202]. However, the Tersoff potential function does not correctly describe the melting point, heat conductivity, and the dimer properties of silicon [202, 203].

Recently, a reactive force field (ReaxFF) has been developed to describe the bond formation or bond breaking and considers the calculation of the electronic structure [204]. The ReaxFF can predict quite accurately both the physicochemical properties and the thermal reactivity of complex chemical structures. The computational speed of these new potentials is comparatively faster. Therefore, the calculation of a large number of atom trajectories can be performed efficiently, which is necessary to model a complex mechanism such as surface oxidation of metals or semiconductors. This capability makes it an appropriate and useful tool to simulate a system containing a large number of atoms in an acceptable computational duration. Therefore, this potential could be a superior semi-empirical approach for describing silicon.

ReaxFF has already successfully applied to a wide range of chemical environments, including metallic and non-metallic elements (shown in Figure 2.15)

[205]. In recent years, ReaxFF MD simulations have been utilized to investigate the thermal oxidation of Si surfaces, including nano-oxidation [206-208], initial stage oxidation [209-211], and dry-oxidation [212]. Among these works, the oxidation processes were systematically studied, as well as the temperature effect, orientation effect, interfacial interaction, and stress evolution.

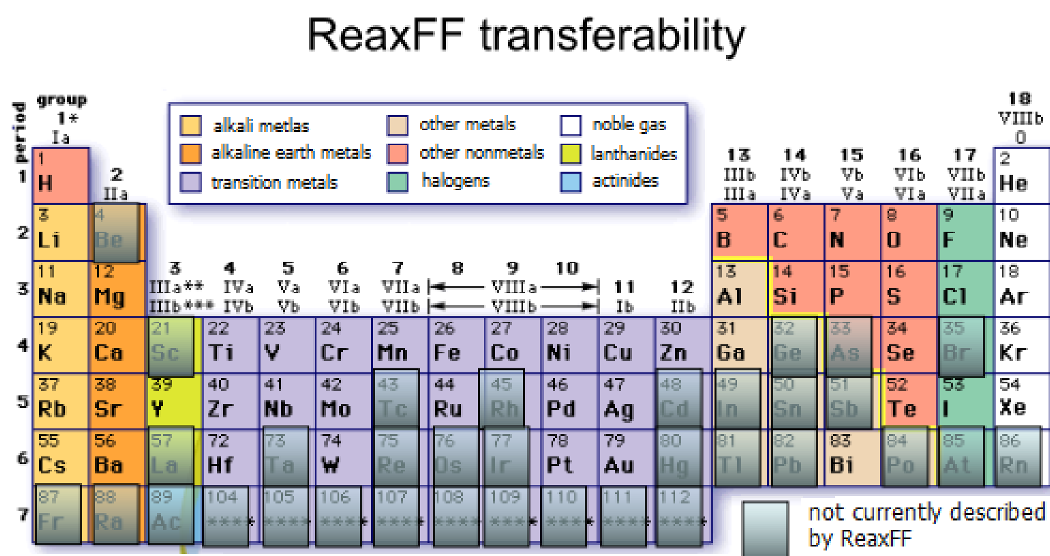

Figure 2.15 Chemical elements currently described by the ReaxFF potential [205].

2.9.5 Previous simulation studies on the oxidation process of Silicon

Up to date, a few MD simulations were performed to obtain an in-depth understanding of the oxidation process and microstructure evolution in the NEL process. Tobias Cramer *et al.* performed MD simulations on the formation of a water bridge induced by an electric field on a hydrophilic silicon surface [213]. They showed that an electric field changes the shape of the water drops to form a water bridge between the stamp and the substrate (shown in Figure 2.16a). They also described a molecular explanation for the threshold voltage and the hysteresis behavior observed in the formation of a nanoscale liquid bridge. The height of the water bridge increases

over time and depends on the electric field (shown in Figure 2.16b). They found the threshold electric field for the bridge formation to be about 1.2 V/nm. Christopher D. Daub *et al.* used MD simulation to explain the sensitivity of the contact angles of the water droplets to the applied electric field [214].

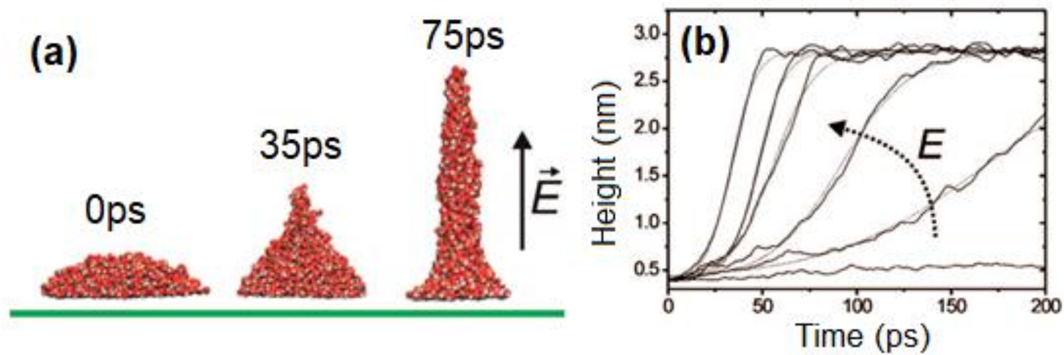

Figure 2.16 (a) MD evolution of water molecules in the presence of an external electric field. (b) Height of the water bridge as a function of time for six values of the electric field (2.25, 2.0, 1.75, 1.5, 1.25, and 1.0 V/nm). The dotted lines present the fit to the sigmoidal function [213].

Besides, some other methods were also employed to investigate the local oxidation mechanism. Notargiacomo *et al.* utilized the superposition principle to identify the critical control parameters that are responsible for the formation of uniform oxide patterns: lines and rectangular layers [215]. In 2012, a simulator for nano oxidation was developed in a Level Set environment by using the empirical equations [216]. This simulator was used to simulate the height and half-width of a nanodot, or nanowire produced with AFM oxidation. Recently, Theogene and his group have used the finite element method to analyze the electric field distribution on the silicon sample [217].

2.10 Summary

For many years, nanolithography technology has contributed to the advance in the nanomanufacturing industry and is influencing the future of nanoscience and technology. Flexibility, high throughput, high resolution, high reliability, high-efficiency, and low-cost are the requirements for the nanolithography techniques to meet future demand. Conventional photolithography has been the main lithography technique that meets the current throughput demand for the semiconductor industry but comes with its resolution limit. In the last decade, considerable effort has been made in the development of nanolithography techniques for mass production of integrated circuits. Through this chapter, the overall status of the potential next generation lithography techniques has been provided, which is summarized as follows:

- EUVL is expected to be available shortly with high-resolution capability, but its adoption in the HVM industry remains uncertain. The EUVL infrastructure needs substantial progress, including source reliability, LER/LWR improvement, and defectivity. More studies are required to develop the issues related to the cost of ownership. EUVL can be more cost-effective by enabling new integration schemes through other techniques (planarization, DSA). It can also include multipatterning (Double expose), LELE process to prepare this technique for next-generation patterning in the future.
- Although EBL and FIBL techniques have high-density ultrahigh-resolution patterning capability, patterning speed significantly limits their application within low volume production. To attain high performance from these techniques, the tool, the resist parameters, and the overall lithography process must be optimized.

- NIL has demonstrated the potentials to achieve the increasing demand for high volume production. Despite the huge commercial success, there are still many challenges that lie in NIL fabrication processes. Defectivity and overlay accuracy remain the main concerns, and further improvements are required to meet the industrial requirements.
- DSA is considered as a promising patterning option that can reduce multi-patterning strategies. Despite being made satisfactory progress, some issues related to defectivity, placement accuracy, and tool design need to be adequately investigated. Besides, the challenges of DSA integration into the fab flow and designing chips around the technology also need to be addressed before the complete implementation in manufacturing.
- SPL techniques are not only a powerful tool in research laboratories, but they can be useful for industrial applications with the possibility of using multi-tips nanofabrication.
- NEL process is still developing continually through academic studies. Uniformity and large-area fabrication are the two major concerns for this process. However, several unique advantages, such as the ability to pattern a wide range of materials and the ability to work in a range of environmental conditions, make this process a promising nanolithography technique for next-generation applications.
- All these techniques are still being developed to reach the roadmap requirements and are expected to come across as a novel next generation lithography technique.

Moreover, the concept and the background of the MD simulation methodology were also described in detail. Finally, an overall review of the previous simulation study on the NEL process was presented. The previous study has mainly concentrated

on water bridge formation. Therefore, other aspects related to the NEL process, such as oxidation mechanism and parametric effects, are worthy of study to perform in a molecular dynamics simulation platform.

Chapter 3 Modeling of the NEL Process

3.1 Introduction

The oxidation process of nanoelectrode lithography is almost instantaneous (<10 picoseconds), which makes the experimental study difficult especially, the observation of the early stage oxidation. Molecular Dynamics (MD) techniques can be instrumental in studying the oxidation mechanism and characterizing the structure of the oxide film. After the development of a new reactive force field (ReaxFF), it is possible to study the reactivity of materials by using a ReaxFF MD simulation via a sophisticated bond-order potential. Therefore, ReaxFF MD simulations have been performed in this thesis to explore the reaction mechanism and parametric effects.

3.2 MD simulation scheme

The sequence of steps involved in an atomistic MD simulation of the NEL oxidation process is shown in Figure 3.1. At first, the molecules (e.g., silicon, water) being studied are built, and the initial geometries are set. This step can be performed by using a molecule builder program (e.g., Materials Studio) or directly obtained from a data set. After that, some parameters are specified, such as the boundary conditions, electric field intensity, and force field. An equilibration program is performed to achieve a thermodynamical equilibrium state that means where the thermodynamic properties appear to converge. Simulations are performed by using the equilibrated system to compute the properties of interest. Finally, the properties are analyzed from the simulation trajectory. All these steps are normally repeated for different models or different simulations.

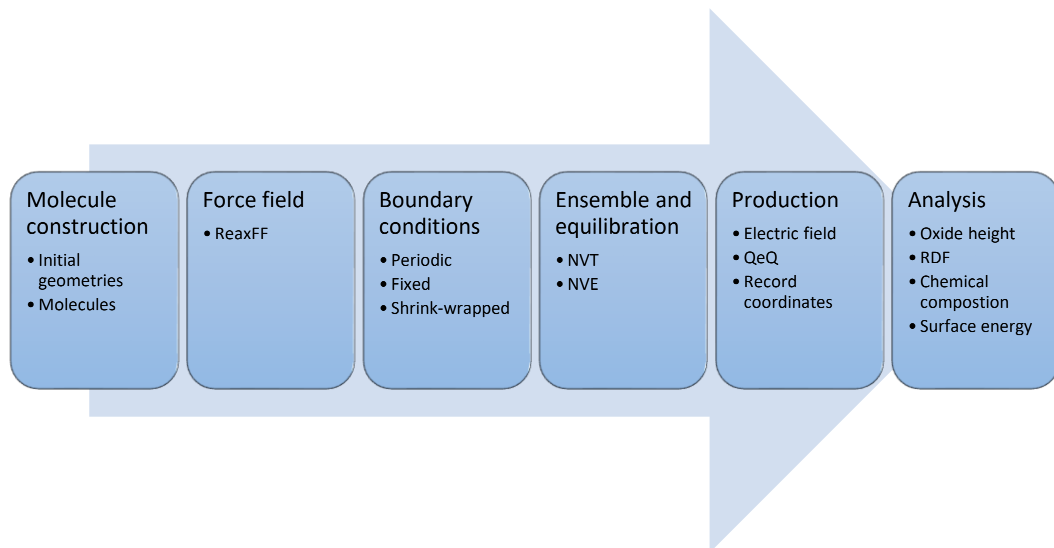

Figure 3.1 Sequence of steps for MD simulations.

3.3 Modeling of the systems and simulation procedure

In order to construct the simulation model, a silicon substrate is considered with the desired size. A 10-Å-thick water layer, which corresponds to a relative humidity of ~90% [218], is placed on top of the Si substrate. A reflecting wall is introduced to confine the water molecules on the top of the substrate. The external electrical field is applied between the Si substrate and the reflecting wall in order to mimic the presence of a conductive stamp on the top of the system. Periodic boundary conditions are applied along both the x and y directions, and a shrink-wrapped boundary condition is applied along the z direction. The side view of the simulation model is illustrated in Figure 3.2. Atoms with orange color represent the silicon. Red and white atoms are Oxygen and Hydrogen, respectively.

It must be mentioned here that the formation of a surface native oxide is a common incidence in silicon. The oxygen reacts with the silicon under the atmospheric environment to produce an oxide layer of 1-2 nm thickness [219, 220]. Generally, the etching with HF is performed to remove the surface native oxide before the fabrication

process. However, there is still a chance to form a very thin native oxide layer (0.6 nm) again after the etching process as the silicon is very prone to oxidation in the ambient conditions. The literature suggests that the native oxide layer does not have any significant influence on the oxidation mechanism and the kinetics of the local oxidation lithography process [5, 221, 222]. The dissociated ions (OH^- and O^{2-}) are diffused through the native oxide layer with the help of applied electric field and the anodic oxidation occurs at the Si/SiO_2 interface [221, 222]. Therefore, the native oxide layer has been omitted in the simulation models to avoid the complexity of the simulations.

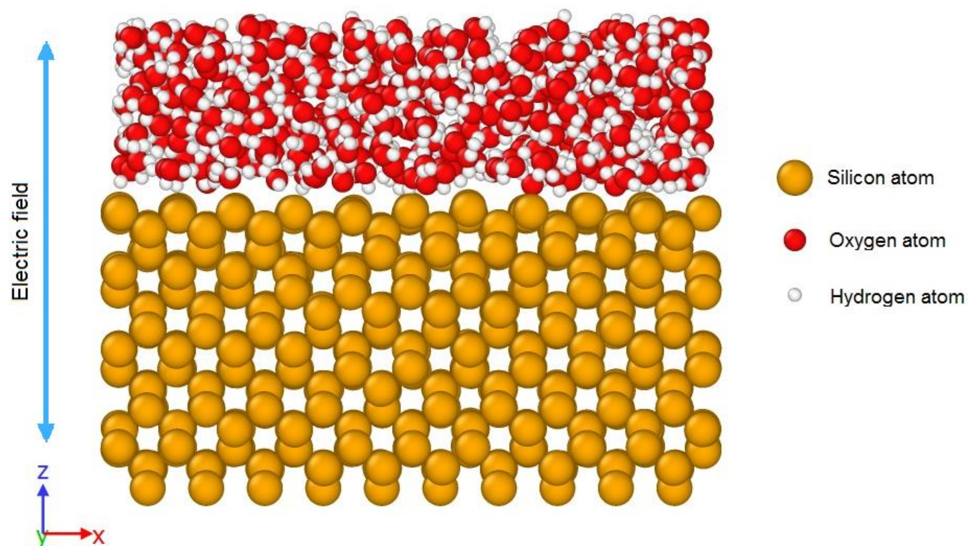

Figure 3.2 Simulation model.

In this thesis, the silicon substrates are chosen with low Miller indices, namely (100), (110) and (111), which are the dominant substrates and structural materials in Integrated Circuits (IC) and device fabrications. Therefore, they have been an excellent model to illustrate some of the fundamental aspects that are involved in the oxidation process. Monocrystalline Silicon substrates are grown from a cubic crystal system

having a diamond cubic structure with a lattice spacing of 5.430710 Å. Four equally spaced neighbors symmetrically surround each silicon atom in a tetrahedral arrangement. This arrangement is the same wherever the zone within the crystal. Figure 3.3 shows the crystal planes for the three different crystallographic orientations of silicon.

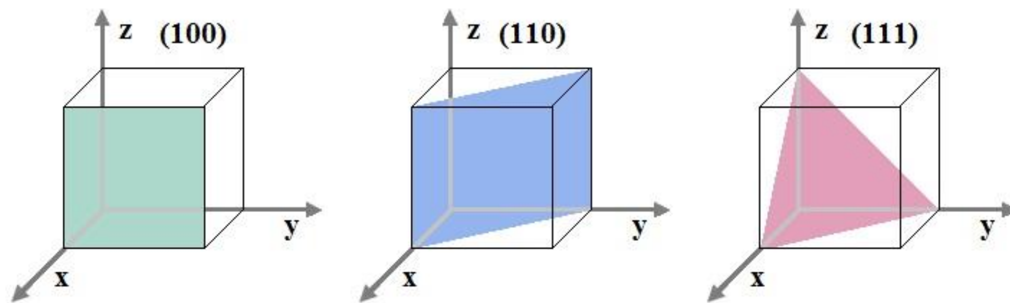

Figure 3.3 Crystal planes of the silicon substrates.

Si (100) plane is used to study the NEL oxidation mechanism under an applied electric field in a humid environment at room temperature. In these simulations, the structural and morphological features related to the growth of the oxide film are assessed. In addition, Si (100), (110), and (111) planes are used to investigate the substrate orientation effects in the NEL process. The details of these models are summarized in Table 3.1. The side views of the three systems are shown in Figure 3.4.

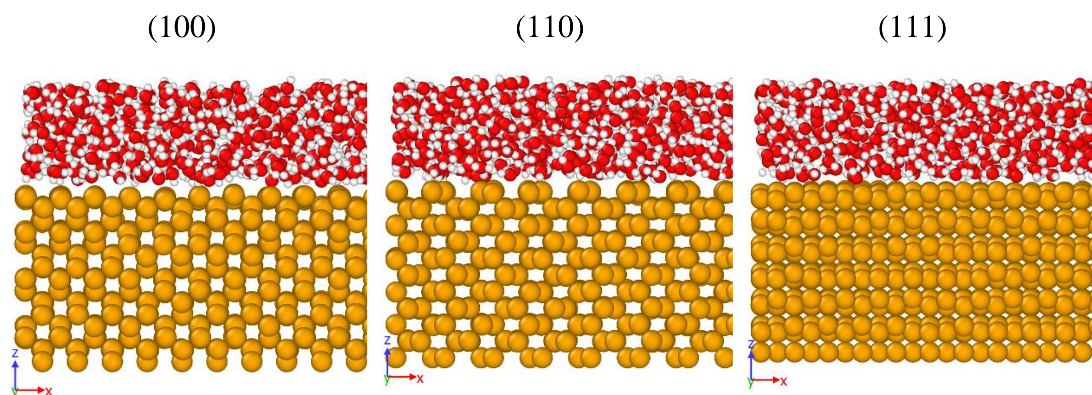

Figure 3.4 Simulation models: Si (orange), O (red), and H (white) atoms.

Table 3.1 Characteristics of the simulated systems.

Crystallographic orientations	Simulation box dimensions (Å)	Number of Si atoms	Number of Si atoms/ML	Areal density of Si atoms		Number of water molecules
				(no./cm^2)	Relative to (110)	
(1 0 0)	L_x: 38.4009 L_y: 38.4009 L_z: 36.4537	1500	100	6.78 x 10^{14}	0.707	490
(1 1 0)	L_x: 38.0149 L_y: 38.4010 L_z: 36.5681	1540	140	9.59 x 10^{14}	1	485
(1 1 1)	L_x: 38.4009 L_y: 39.9072 L_z: 36.1740	1560	120	7.83 x 10^{14}	0.816	505

All the MD simulations are conducted by using the "Large-scale Atomic/Molecular Massively Parallel Simulator" (LAMMPS) code developed at Sandia National Laboratories [223] with a modification done by O. Assowe *et al.* [224]. The details of the modification have been discussed in the section 3.5. To optimize the performance, LAMMPS can be implemented to run in parallel applying the universal MPI (message-passing interface) library. For the parallel run, it is necessary to assign the simulation region for each processor. LAMMPS utilizes spatial-decomposition techniques in this regard, where all the processors share the results, and the "ghost" atom information. All the LAMMPS simulations for this thesis are performed with parallel processing on High-Performance Computing (HPC). The visualization of the atomic trajectories is also carried out using the "Open Visualization Tool" (OVITO) [225]. It can calculate coordination number and radial distribution function, displacement vector, charge distribution, and so many.

The silicon substrates are relaxed first to stable the configuration at room temperature (300 K) in NVT ensemble with the Berendsen thermostat for 50 picoseconds with a damping constant of 25 femtoseconds. All other simulations use the NVT ensemble with the Nose-Hoover heat bath at a time step of 0.1 femtoseconds, and the temperature is controlled to be 300 K with a damping constant of 10 femtoseconds.

3.4 Potential energy function employed in MD simulations

The new reactive force field (ReaxFF) is used for all the simulations. Although the quantum chemical (QC) based methods can be applied to all the chemical systems, regardless of connectivity, they are not suitable for simulating the large-scale system (>100 atoms) due to their computational expense. On the other hand, the conventional empirical force field (EFF) based methods have the ability to realize much larger systems, but they cannot accurately describe the reactive systems. ReaxFF bridges the gap between these two methods.

3.4.1 ReaxFF potential principle

ReaxFF employs a bond length/bond order relationship to make a smooth transition from nonbonded to single, double, and triple bonded systems [226]. Bond orders are calculated at each iteration of the dynamics. The potential energy includes a summation of internal terms (length of bonds, angles of bonds), and external energies (Van der Waals interactions, electrostatic). The internal terms enable it to maintain the covalent geometry of the system, and the external terms represent the interactions between the unbound atoms.

Equation 3.1 shows the ReaxFF energy terms that are comprised of various sources [227]. The atomic interactions represent the valence interactions refer to the bond order (BO) and the noncovalent interactions.

$$E_{ReaxFF}\left(\{r_{ij}\},\{r_{ijk}\},\{r_{ijkl}\},\{q_j\},\{BO_{ij}\}\right) = E_{bond} + E_{lp} + E_{over} + E_{under} + E_{val} + E_{pen} + E_{coa} + E_{tors} + E_{conj} + E_{hbond} + E_{vdWaals} + E_{Coulomb} \quad (3\text{-}1)$$

The energy terms include valence terms, such as bond energy (E_{bond}), lone-pair energy (E_{lp}), overcoordination energy (E_{over}), undercoordination energy (E_{under}), valence angle (E_{val}), penalty energy to reproduce the stability of systems with two double bonds sharing an atom in a valence angle (E_{pen}), angle conjugation (E_{coa}), torsion conjugation (E_{conj}), torsion energy (E_{tors}) and hydrogen bond energy (E_{hbond}). In ReaxFF, the total energy depends on the relative position between atom pair (r_{ij}), between triplets of atoms (r_{ijk}), and quadruplets of atoms (r_{ijkl}). It also depends on the atomic charge distribution (q_j), and the bond order (BO_{ij}) between a pair of atoms. Non-covalent interactions include van der Waals energy ($E_{vdWalls}$), and Coulomb interaction ($E_{Coulomb}$).

Each of these above energy terms corresponds to an analytic function whose parameters are trained against quantum chemical results. Thus, it confirms the accuracy of the chemical reactions and can deal with a relatively larger system for a longer time scale [208]. A more detailed description of each energy term is presented in references [228, 229]. Some of these terms related to this thesis are described in the next sections.

3.4.2 Calculation of bond order and bond energy

An important element of the ReaxFF is the bond order to describe the covalent bonds. This allows the ReaxFF potential to define and manage connectivity changes during reactions. This function is decomposed in terms of three exponential functions corresponding to the sigma (σ), pi (π), and double pi (π-π) bonds. The BO calculation involves two steps: (i) computing instantaneous BOs (BO'_{ij}), (ii) Correction of each instantaneous BO with over-coordination, and under-coordination terms. The bond order, BO'_{ij}, is calculated as a sum of σ, π, and double-π bond contributions, as shown below:

$$BO'_{ij} = BO_{ij}^{\sigma} + BO_{ij}^{\pi} + BO_{ij}^{\pi\pi} = exp\left[P_{bo1}\cdot\left(\frac{r_{ij}}{r_0^{\sigma}}\right)^{P_{bo2}}\right] + exp\left[P_{bo3}\cdot\left(\frac{r_{ij}}{r_0^{\pi}}\right)^{P_{bo4}}\right] + exp\left[P_{bo5}\cdot\left(\frac{r_{ij}}{r_0^{\pi\pi}}\right)^{P_{bo6}}\right] \quad (3\text{-}2)$$

where $r_{ij} = |\mathbf{r}_{ij}| = |\mathbf{r}_i - \mathbf{r}_j|$ refers to the distance between the atoms i and j ($\mathbf{r}_i$ is the position of the ith atom) with i, j = 1, ..., N (N being the total numbers of atoms).

As the values of the exponential terms depend on the inter-atomic distances, they become negligible at longer distances. These bond orders are updated at each iteration and subsequently corrected to produce correct atomic valences. The bond energy is also contributed from the sigma (σ), pi (π), and double pi ($\pi\pi$) bonds. It is obtained with:

$$E_{bond} = \sum_i \sum_j \left[-D_e^{\sigma}.BO_{ij}^{\sigma}.exp\left\{P_{be1}\left(1-\left(BO_{ij}^{\sigma}\right)^{P_{be2}}\right)\right\} - D_e^{\pi}.BO_{ij}^{\pi} - D_e^{\pi\pi}.BO_{ij}^{\pi\pi}\right] \quad (3\text{-}3)$$

where BO_{ij} refers to the bond order between the atoms i and j, D_e and P_{be} are the calibrated parameters for different bonds. While the chemical bonds break, the bond order BO_{ij} and the bond energy tend to be zero. Similarly, all other valence terms that depend on the bond order also tend to be zero. Because of this, a smooth transition of energy is possible.

3.4.3 The energy of nonbonded atoms

ReaxFF computes nonbonded interactions (van der Waals and coulomb) for each pair of atoms. Van der Waals interactions are defined by a function that includes both short-range repulsions and long-range attractions. With ReaxFF, the Coulomb energy term is presented as follows:

$$E(q) = \sum_i \left[\chi_i q_i + \eta_i q_i^2 + Tap(r_{ij}).k_c \frac{q_i q_j}{\left(r_{ij}^3 + \gamma_{ij}^{-3}\right)^{1/3}} \right], \quad \sum_{i-1}^{n} q_i = 0 \quad (3\text{-}4)$$

where q_i and q_j refer to the charges of atoms i and j, respectively. k_c, χ and η represent the dielectric constant, the electronegativity, and the hardness of each atom, respectively. γ_{ij} refers to a parameter for the smeared Coulombic function. $Tap(r)$ is a polynomial taper function of 7th order, which depends on the inter-atomic distance.

3.4.4 Polarization of charges

In ReaxFF, the charge distribution on atoms depends on their environment, and the atomic charges change dynamically in time. The calculations of the atomic charges

are carried out by electronegativity equalization method (EEM) considering the charge-neutrality constraint, $\sum_i q_i = 0$. This method was previously reported in [230, 231]. Calculation of the charges by the ReaxFF method is presented as follows [226]:

$$\frac{\partial E}{\partial q_1} = \chi_1 + 2q_1\eta_1 + C.\sum_{j=1}^{n} \frac{q_j}{\left(r_{1,j}^3 + \left(\frac{1}{\gamma_{1,j}}\right)^3\right)^{\frac{1}{3}}} \tag{3-5}$$

$$\frac{\partial E}{\partial q_2} = \chi_2 + 2q_2\eta_2 + C.\sum_{j=1}^{n} \frac{q_j}{\left(r_{2,j}^3 + \left(\frac{1}{\gamma_{2,j}}\right)^3\right)^{\frac{1}{3}}} \tag{3-6}$$

$$\cdots\cdots\cdots\cdots\cdots\cdots\cdots\cdots$$

$$\cdots\cdots\cdots\cdots\cdots\cdots\cdots\cdots$$

$$\frac{\partial E}{\partial q_n} = \chi_n + 2q_n\eta_n + C.\sum_{j=1}^{n} \frac{q_j}{\left(r_{n,j}^3 + \left(\frac{1}{\gamma_{n,j}}\right)^3\right)^{\frac{1}{3}}} \tag{3-7}$$

$$\sum_{i=1}^{n} q_i = 0 \tag{3-8}$$

where,

χ: atom electronegativity

η: atom hardness

γ: shielding parameter

r: interatomic distances

q: atom charge

Electronegativity and hardness are updated at each iteration according to a charge equilibration (QEq) model, as described in [232]. This model encompasses

electrostatic energy minimization by allocating partial charges as a function of electron affinity and atom radius. These parameters are optimized against QM-charge distributions.

3.5 Introduction of the electric field in the code LAMMPS / ReaxFF

To introduce the electric field into LAMMPS, the coulomb energy term (Eq (3.4)) has been modified in the ReaxFF potential by Assowe *et al.* [224]. The modification utilizes the formula proposed by Chen and Martinez [233]. They consider atom polarization, charge conservation, electronegativity differences using the charge-fluctuation model. An electric field has been integrated into the Coulomb energy, *E(q)*, which eventually allows the calculation of electrostatic properties, such as multipolar moments and polarizability. The modified coulomb energy equation is of the form:

$$E(\mathbf{q}, E^{v}) = E(\mathbf{q}) - \mathbf{q}.\sum_{v} \mathbf{R}_{v} E^{v} \tag{3-9}$$

Where $\mathbf{q}$ is the atomic charge, and $\mathbf{R}_v$ is their spatial positions (The bold notation refers to the vectors and matrices). E ($\mathbf{q}$) refers to electrostatic energy without the electric field, as described in Eq. (3.4). E^v is the external electric field where ν denotes the directions of space.

The electronegativity (χ) of the atoms has also been modified considering the new atomic charge distribution and the electric field.

$$\chi_i \rightarrow \chi_i - \sum_{v} \boldsymbol{R}_{iv} E^{v} \tag{3-10}$$

These modified equations have been used in ReaxFF code files, *reaxc_nonbonded.cpp* and *fix_qeq_reax.cpp*.

In the file *reaxc_nonbonded.cpp:*

my_en.e_pol += KCALpMOL_to_EV * [(chi * q + (eta / 2.) * q^2) – q * (x[0] * EX + x[1] * EY + x[2] * EZ)]

where KCALpMOL_to_EV denotes the conversion factor from electron-volt to Kcal/mol.

The above coding is equivalent to:

$$E(\mathbf{q}, E^v) = 23.02 \times [E(\mathbf{q}) - \mathbf{q}.\sum_v \mathbf{R}_v E^v] \tag{3-11}$$

In the file *fix_qeq_reax.cpp:*

B_s[i] = -chi[atom->type[i]]

B_s[i] += (x[i][0] * EX + x[i][1] * EY + x[i][2] * EZ)

These coding lines represent the equation (3-11).

In addition, **fix efield** command has also been used to add a force to all the atoms due to an external electric field being applied to the system. The force is of the form:

$$\overline{\mathbf{F_i}} = \mathrm{q_i}.\bar{\mathbf{E}} \tag{3-12}$$

3.6 Validation of the modified LAMMPS with ReaxFF

3.6.1 Force field validation

The ReaxFF parameters used in this thesis were developed by Jialin Wen *et al.* [234] based on the combination of the Si/Ge/H force field [235] with the water force field [236]. For validation, the surface energy, cohesive energy, and the lattice constant have been calculated and compared with other results. Surface energies were computed

for the low-index orientations (100), (110), and (111) of silicon substrates. The calculation procedures are as follows:

1) At first, a perfect silicon system with PBC is created considering the stacking periodicity (number of lattice planes in the repeat stacking unit) [237] along the different orientations. Then, the minimization of the atom's positions is performed, and the energy E_0 is obtained.

2) The same procedure is followed to build the system with the same dimensions. The periodicity along the z-direction is removed to create two symmetrical free surfaces (i.e., shrink-wrapped boundaries along that direction). Then minimization of the atom's coordinates is performed, and the energy E_1 is obtained.

3) The surface energy is calculated from the following expression:

$$E_{surf} = \frac{E_1 - E_0}{2A} \text{ J m}^{-2} \tag{3-13}$$

where A is the surface area.

The results are tabulated in Table 3.2 with other results obtained by using various potentials, DFT calculations, and experiments. Table 3.2 shows that the present ReaxFF potential produces the cohesive energy, which is very close to the experimental value, and other potential values. This potential also produces the surface energies for three crystallographic orientations, which are closer to DFT calculations. The lattice constant is computed as 5.314 Å, which is similar to the value found by Psofogiannakis *et al.* [235].

Table 3.2 Cohesive energy and surface energy of silicon computed with different potentials, DFT calculations, and experiments.

Property	ReaxFF	Tersoff [238]	MEAM [199]	SW [184]	DFT	Experiment
Cohesive energy (eV)	4.56	4.63 [238]	4.63 [238]	4.33 [238]	4.84 [239]	4.63 [242]
Surface Energy {100} (J m^{-2})	2.55	2.19 [238]	1.74 [238]	2.36 [238]	2.36 [240]	1.36 [243]
Surface Energy {110} (J m^{-2})	1.81	1.36 [238]	1.41 [238]	1.67 [238]	1.75 [240]	1.43 [243]
Surface Energy {111} (J m^{-2})	1.48	1.11 [238]	1.2 [238]	1.36 [238]	1.57 [241]	1.23 [243]

This potential had also been validated by Jialin Wen *et al.* [234]. They computed the water-binding energy to be 20 kcal/mole, which is very close to the DFT result (22.5 kcal/mole). For the water dissociation reaction, the water dissociation barrier was calculated about 10 kcal/mole, which is also in good agreement with the DFT results. In addition, the radial distribution functions (RDFs) were computed for crystal silicon, amorphous silica, and H_2O, which are consistent with both computational results and experimental results. They have used this force field successfully to investigate the interaction of silicon with water, and the tribochemical wear mechanism of silicon [208, 234].

3.6.2 Validation of the introduction of the electric field

To check the energy conservation in NVE over time, the calculation is performed with a slab of Si (100), adding a layer of water on top of it. The Si slab and the water layer contain 900 atoms and 226 molecules, respectively. The size of the simulation box is 38.4 Å x 38.4 Å x 19.3 Å. The system is periodic, according to X and Y, and fixed according to Z. The electric field is oriented along Z and is parallel to the dipole moments of the water molecules. The calculations have been performed for 10 ps in NVT to thermalize the system to 300 K and 5 ps in NVE to check the total energy conservation. From Figure 3.5, it has been noticed during thermalization that the energy fluctuates while converging. Then the total energy of the system is conserved in NVE whatever the value of the electric field. The energy of the system increases with the field due to the contribution of the electric fields. The temperature of the system fluctuates around 300 K in NVT and increases in NVE (shown in Figure 3.6).

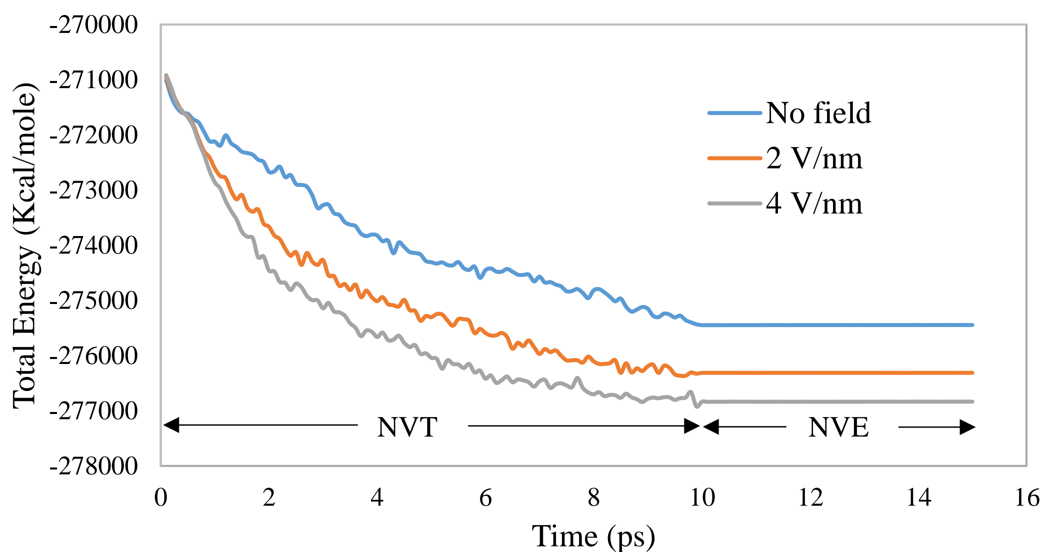

Figure 3.5 Evolution of the total energy of the system over time for different values of the electric field.

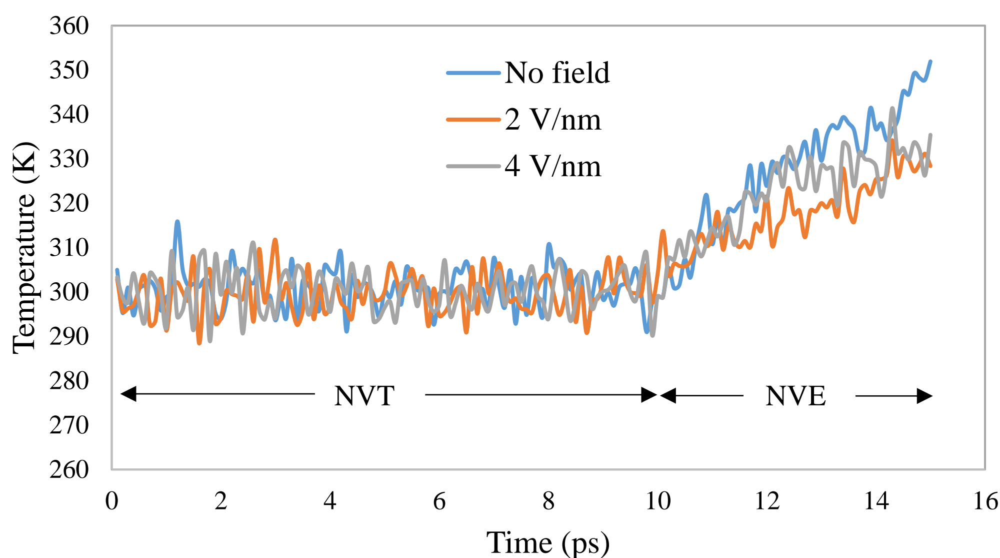

Figure 3.6 Evolution of the system temperature over time for different values of the electric field.

3.7 Summary

This chapter described the MD simulation methodology used for the NEL oxidation process in detail. The choice of a potential energy function is an important consideration for an accurate MD simulation. ReaxFF interatomic potential function was adopted to describe the interactions between atoms. To introduce the electric field in LAMMPS/ReaxFF, the necessary modification has been performed and discussed in detail. The validation of the LAMMPS/ReaxFF has been done, which suggests that the simulation method works well to investigate the oxidation process. Then, the models were relaxed for 50 ps at a temperature of 300 K. All the simulations were conducted on an HPC service, and OVITO was used to visualize and post-process the atomistic data.

Chapter 4 MD Simulated Study for the NEL Oxidation Process

4.1 Introduction

The NEL oxidation of silicon involves a number of simultaneously occurring processes, such as molecular adsorption and dissociation, ion recombination, ion transportation, oxide formation, all of which are influenced by the electric field intensity and the relative humidity. Despite numerous simulation efforts on exploring the effect of the electric field on water bridge formation and the NEL oxidation mechanism, the process has not been fully investigated at the molecular level. A good understanding of the oxidation process, especially the early stage oxidation process and the parametric effects, would aid in acquiring a broad picture of the nanoelectrode lithography of silicon, which can help to enhance the performance and optimize the parameters. This chapter provides the MD simulation results regarding the oxidation mechanism of Si (100) and the parametric influence on oxide growth, such as electric field intensity and the relative humidity.

4.2 Analysis of the oxidation process

An electric field of 2 V/nm has been applied between the reflecting wall and the substrate to understand the oxidation mechanism as the minimum electrical field required to polarize and pull the water molecules adsorbed on the surface towards the stamp is ~1.3 V/nm [244]. Figure 4.1 shows the snapshot details at the end of the simulation (400 ps) at 300 K, which indicates the formation of an oxide film. The adsorption and the dissociation of water on the Si surfaces have also been observed.

To explain the oxidation process, only a few water molecules on the silicon surface are visualized in Figure 4.2 and Figure 4.3.

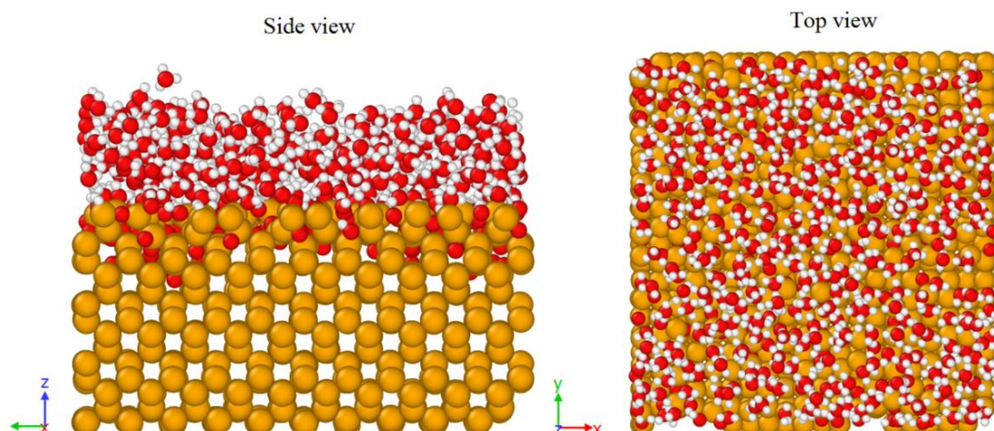

Figure 4.1 Side view and top view of the system after 400 ps of simulation.

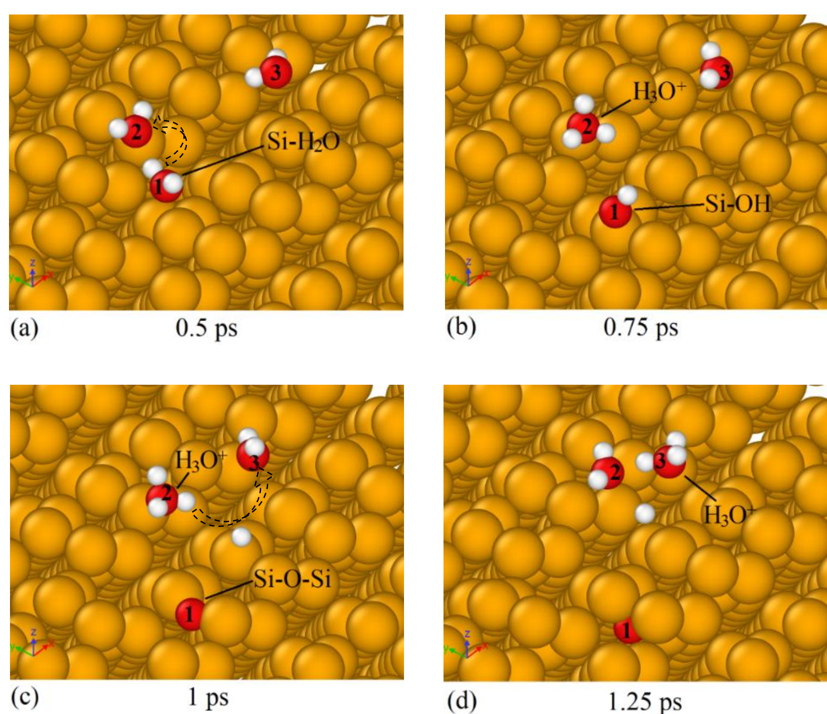

Figure 4.2 The interaction between H_2O and Si (100) substrate surface. (a) Three water molecules in which one water molecule (numbered 1) adsorbed on the Si substrate surface. (b) Dissociation of water and the formation of Si–OH and H_3O^+. (c) Proton transfer process between two adjacent water molecules.

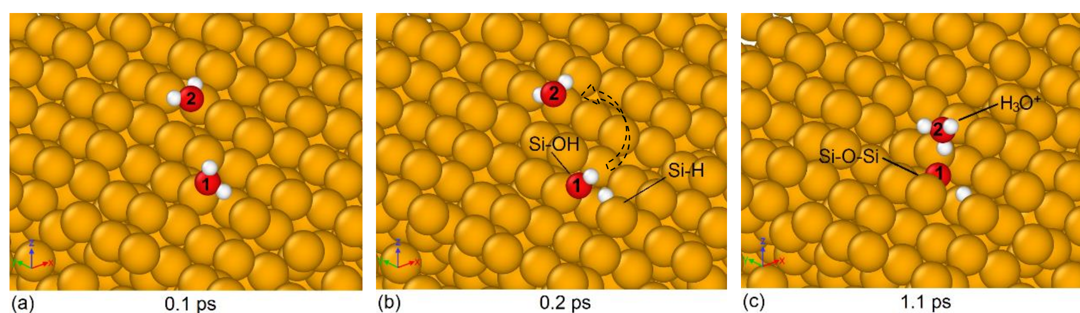

Figure 4.3 (a) Two water molecules on the Si surface. (b) Formation of Si−H and Si−OH. (c) Bond breaking of Si−OH to form Si−O−Si and H_3O^+ formation.

After 0.5 picoseconds, the water molecule (numbered 1) is adsorbed on the silicon surface shown in Figure 4.2(a). Then the water molecule is dissociated into ions (OH^- and H^+) to form a Si–OH bond. The proton (H^+) goes to a nearby water molecule (numbered 2) to form hydronium, H_3O^+ (shown in Figure 4.2b). The average charges of OH^- and H_3O^+ are observed to be −0.237 *e* and +0.285 *e*, respectively. Subsequently, there is a breaking of Si–OH bond, and the oxygen atom is occupied the space between the silicon atoms that leads to the formation of Si–O–Si bond (shown in Figure 4.2c). Again, the proton is transferred from the second water molecule to the third one, as shown in Figure 4.2(d). There is an increase in the average charges of the surface silicon atoms while the chemical reactions occur. For an arbitrary silicon atom, the charge is +0.125 *e* at 0.5 picoseconds where it increases to +0.237 *e* just after bond breaking with an OH^- at 0.6 picoseconds.

It is also observed that the water molecule can be dissociated directly, which forms Si–H and Si–OH bonds, as demonstrated in Figure 4.3 (a, b). After a period (at 1.1 ps), the hydroxyl of Si–OH decomposes into an oxygen atom and a hydrogen atom. The oxygen atom then combines with the silicon atoms to form Si–O–Si bond (shown in Figure 4.3c). The hydrogen atom also combines with a water molecule to form the

H_3O^+. The above-explained oxidation processes were also previously observed experimentally for thermal oxidation of silicon (100) surface [245, 246]. This oxidation process is being repeated over time that develops an oxide film on the silicon surface.

Figure 4.4 depicts the evolution of the thickness of the oxide film throughout the simulation, which displays several layers of oxide height. The oxide growth experiences a rapid surge at the very beginning and reaches more than 2 Å within 2 picoseconds. Then the oxide height shows a steady but significant increase over the period until a quick rise at 13 picoseconds to reach the first significant layer (~4.8 Å). The Si/O stoichiometry is found to be 4.45 at 11 picoseconds. Then the Si/O stoichiometry decreases gradually to 2.54 at 15 picoseconds, which means the more filling of oxygen atoms in this layer. After that, the oxidation process seems to be slowed down. This layer continues with a little fluctuation in oxide height until 315 picoseconds, and then there is an abrupt escalation to reach the next layer (~6 Å). Higher Si/O stoichiometry is found in this layer than that of the previous layer, and it also shows the same decreasing behavior.

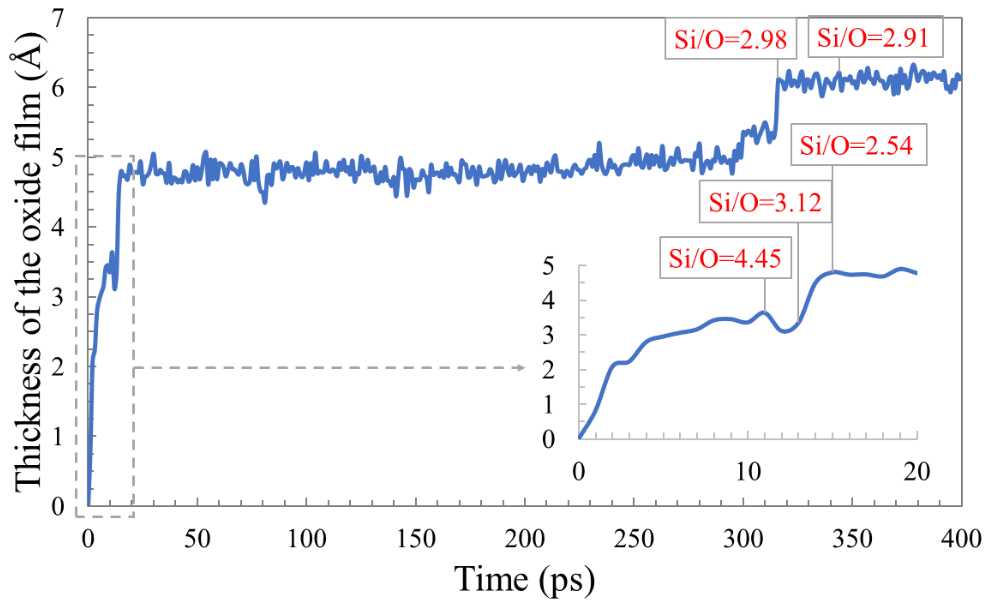

Figure 4.4 Evolution of the oxide film for an electric field of 2 V/nm.

Many studies have been performed to provide a physical explanation for the slowness of the oxide growth observed in the oxidation process. According to Dagata *et al.,* the reason for the slowness is the accumulation of ionic charges of the oxides after its creation that affects the charge diffusion in the water bridge [150]. Avouris *et al.* have proposed that large stresses are developed due to the density mismatch between silicon and SiO_2 [151]. The increase in the stress eventually increases the activation energy for oxidation, which in turn acts as a barrier to the oxide growth. Moreover, some researchers also revealed that the electric field within the oxide film decreases with the increase of the oxide thickness [222, 247]. The adsorbed oxygen and the initial oxidized silicon at the silicon-oxide interface generate an electric potential (Mott potential), which effectively reduces the energy barriers for ionic diffusion through the oxide. As the oxide thickness increases, the additional effect of the Mott potential lessens, and hence decreases the electric field within the oxide film

[248]. When the electric field is no longer sufficient (reaches a critical value) for the ionic diffusion, the oxide growth self terminates [222].

The number of chemical compositions developed during the simulations is shown in Figure 4.5. It is seen that the number of water molecules decreases over time while the number of ions (OH^-, H_3O^+, O^-, H^+) increases, which is evident as the water molecules dissociate into ions. There is a rapid increase in the number of ions at the beginning, which represents the quick oxide growth, as explained in Figure 4.4. After 11 picoseconds, the amount of OH^- starts to decrease gradually over time. The OH^- combines with the silicon surface and then releases proton, which eventually facilitates the formation of the oxide film. The proton recombines with the water molecules that gradually increases the number of H_3O^+ over time. After 20 picoseconds, the oxidation process continues with a slow oxidation rate.

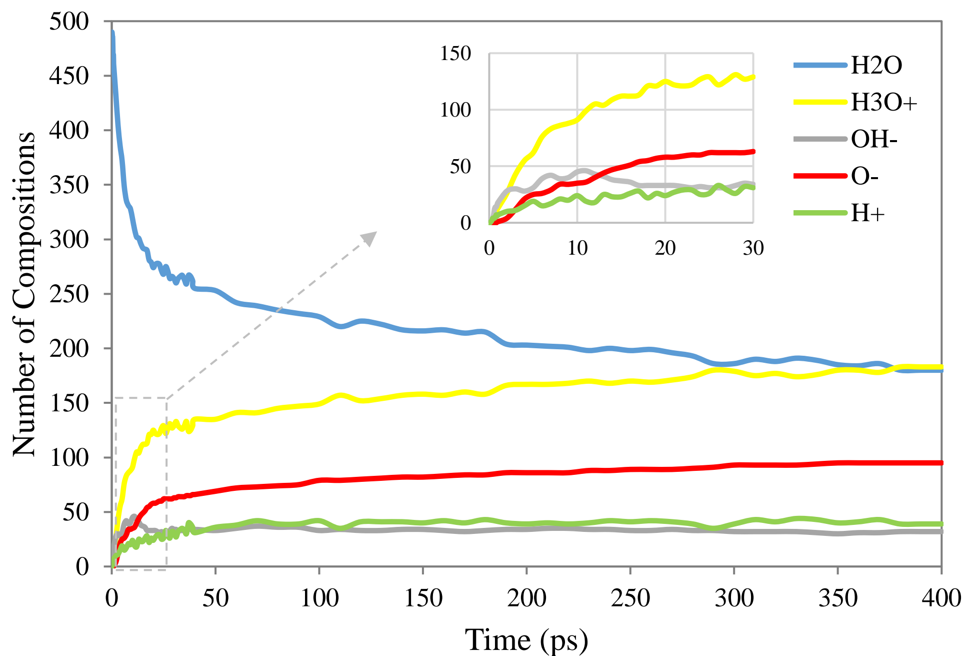

Figure 4.5 Evolution of the chemical compositions for an electric field of 2 V/nm.

The partial radial distribution functions (RDFs) are used to characterize the structure of the formed oxide film. Figure 4.6 shows the partial RDFs for the entire oxide film with inset with the RDFs for the central part of the oxide film at the end of the simulation. The Si–Si distances and the nearest-neighbor O–O are observed to be 2.325 Å and 2.675 Å, respectively. These values are quite close to the experimental results: 2.35 Å for the Si-Si distance and 2.65 Å for the nearest-neighbor O-O [249]. A second peak for the Si–Si partial RDF appears at 3.825 Å, which also agrees with the simulation results [194]. For the mean Si–O bond length, the position of the first peak is found at 1.575 Å, which is very close to the experimental values of ~1.61 Å [250, 251]. After the first peak, several plateau-shaped revealing non-defined orders are observed, which indicates an amorphous structure.

To confirm the formation of the amorphous structure, the ability of the applied potential function to crystallize the oxide from an amorphous phase is being checked first. To do this, a large sphere of SiO_2 has been heated to 4000 K, which is above the melting temperature (~ 2000 K). The temperature has been increased in successive ramps. The reason to choose the sphere shape is to prevent the "geometrical" constrains due to the periodic boundary conditions. After melting, it has been cooled down slowly to see if there is any recovery of a crystalline SiO_2 phase. The radial distribution function, g(r), at 4000 K shows that the system is almost one of a liquid (shown in Figure 4.7). When the melted system gets cooled down to 300 K, a crystalline state is recovered that is a sphere with several grains of SiO_2. The g(r) after cooling is shown in Figure 4.8. Therefore, the potential can recover a crystalline state from a melt and able to crystallize SiO_2 during oxidation. Therefore, the structure of the oxide film

seems to be amorphous. Dagata *et al.* also concluded the same finding based on the stress and space charge [150].

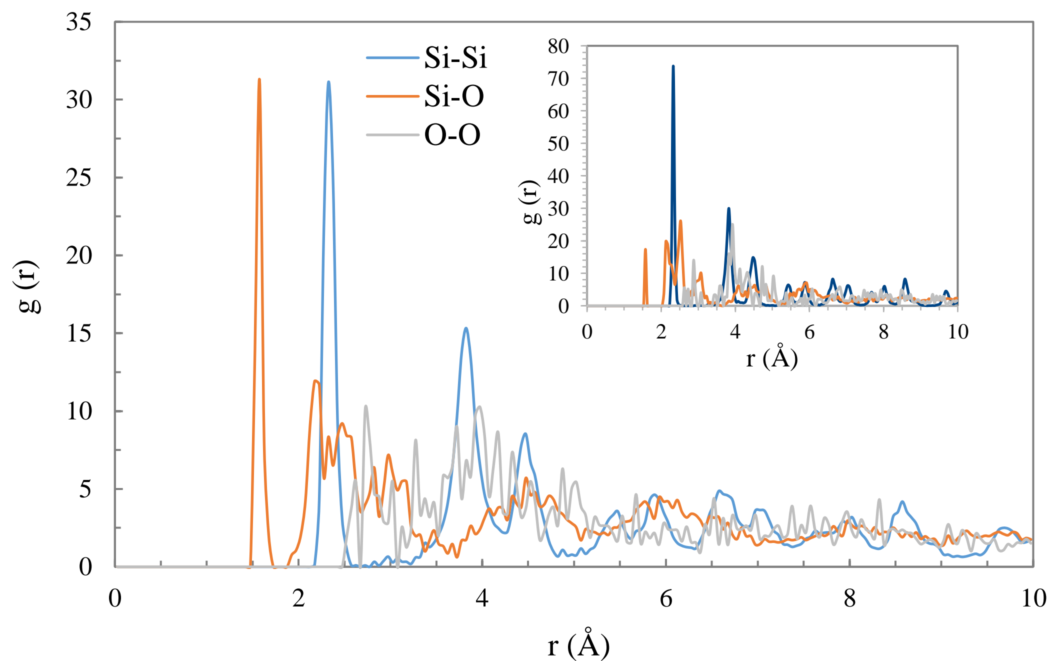

Figure 4.6 Partial radial distribution functions in the oxide film.

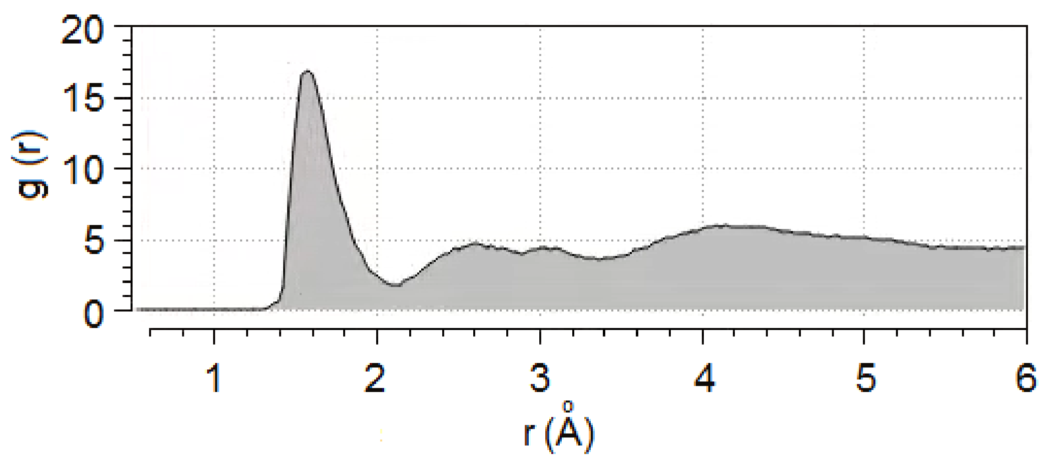

Figure 4.7 g(r) after melting.

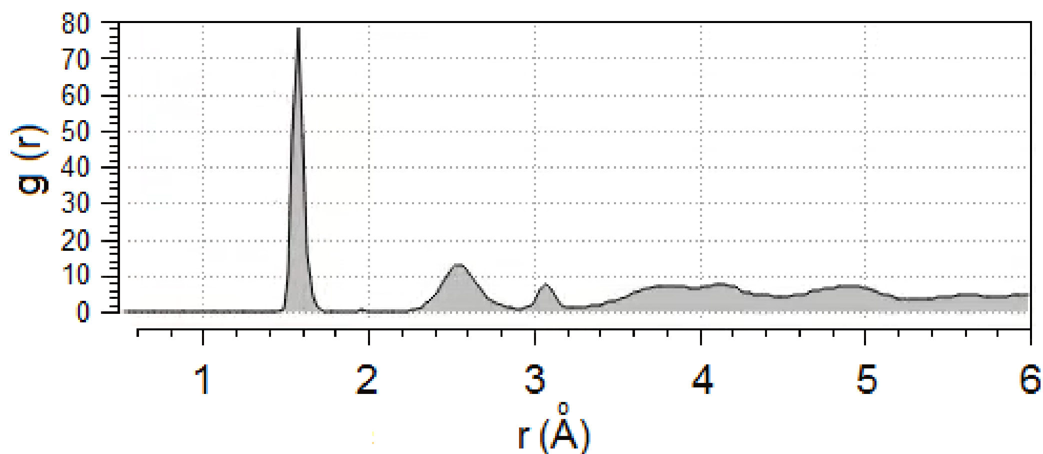

Figure 4.8 g(r) after cooling.

The oxygen distribution in the oxide film along the z direction has also been studied, which is shown in Figure 4.9. The number of O atoms is summed every 0.4 Å sized bin. The zero position of z refers to the initial surface position. The maximum number of oxygen atoms is found at a depth of around 1.6 Å. The density of the oxygen shows less in the deeper positions of the oxide film. Few atoms have penetrated the surface as deep as around 6 Å.

The atomic charge distribution at the end of the simulation is shown in Figure 4.10. The charges of the silicon atoms outside the oxide film fluctuate slightly around 0 *e* while the oxygen atoms and the hydrogen atoms have a charge of fluctuating around -0.70 *e* and +0.30 *e,* respectively. These charges are very close to the charges obtained for the bulk of water. It is observed that the charges of the oxidized silicon atoms increase from the bottom part to the upper part of the oxide film, and the maximum charge is found ~+0.77 *e* at around 22.5 Å. The average charge of the oxygen atoms in the oxide film is found to be ~-0.45 *e* with a minimum value of ~-0.41 *e* at around 17 Å.

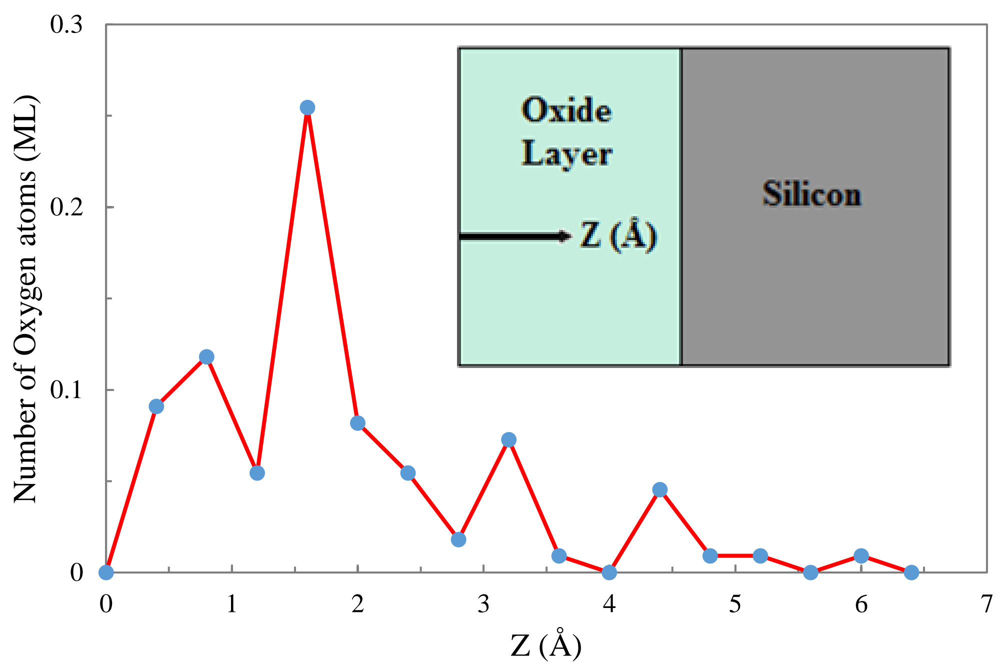

Figure 4.9 Oxygen atoms distributions below the Si surface at 400 ps. Z is the depth below the surface, and its origin is taken as the initial surface position.

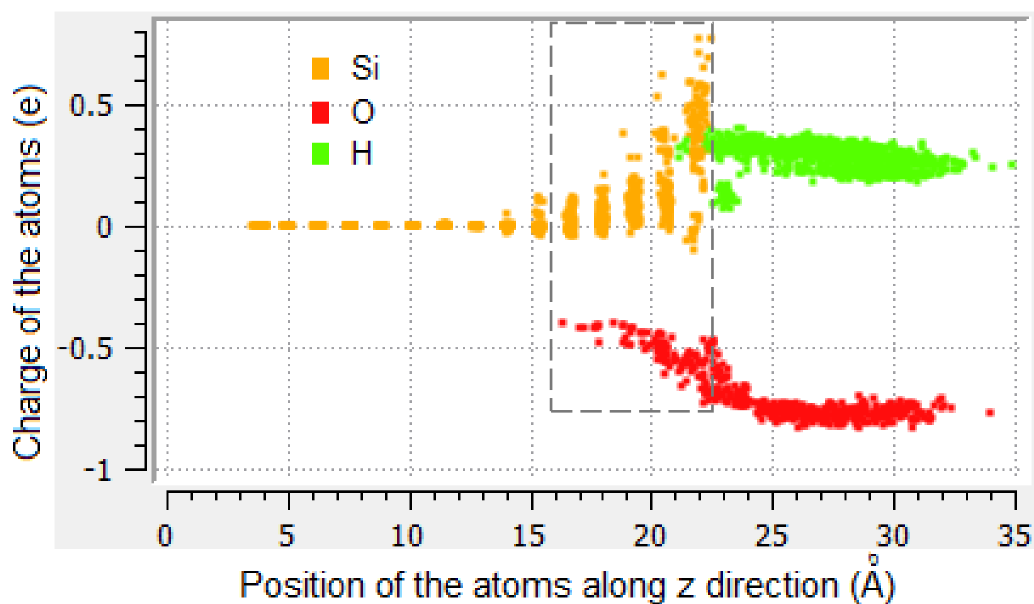

Figure 4.10 Distribution of atomic charges after 400 ps.

4.3 Effect of the electric field

The dependence of the oxide height as a function of the oxidation time for different values of the electric field is presented in Figure 4.11. The electric field has been varied from 1.5 V/nm (threshold value is 1.3 V/nm) to 7 V/nm. All the curves show similar characteristics, as explained in section 4.2. A fast growth of the oxide film is observed at the very beginning then it slows down. About 60% of the total oxide thickness is achieved within the first 20 picoseconds. It has been noticed that increasing the field intensity speed up the process and the kinetics of the reaction, especially at the beginning. After that, the oxide height grows layer by layer fashion. The thickness of the oxide film shows a linear dependency on the electric field intensity (Figure 4.12). This result agrees with the observations of Montserrat Calleja *et al*. [219], which shows that the thickness of the oxide layer on silicon (100) surface increases linearly with the electric field. Again, Stievenard *et al.,* [252] theoretically explained this linear oxide growth with bias voltage based on the Cabrera-Mott theory of metal thin film oxidation [253]. They showed that the electric field increases the ionic diffusion.

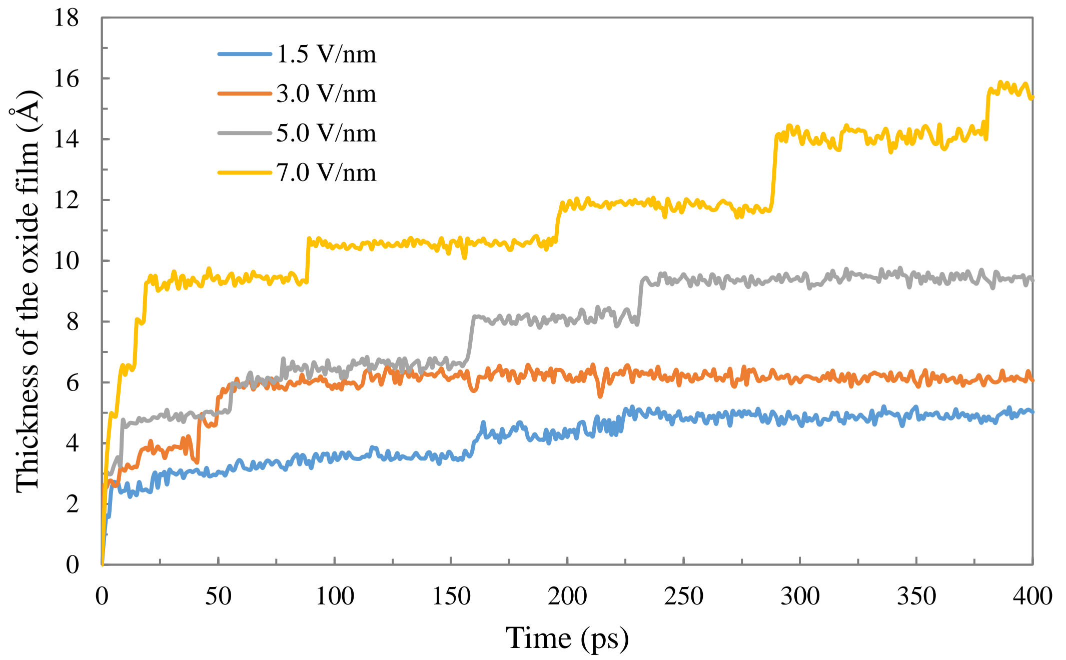

Figure 4.11 Evolution of oxide film thickness for various electric field intensities.

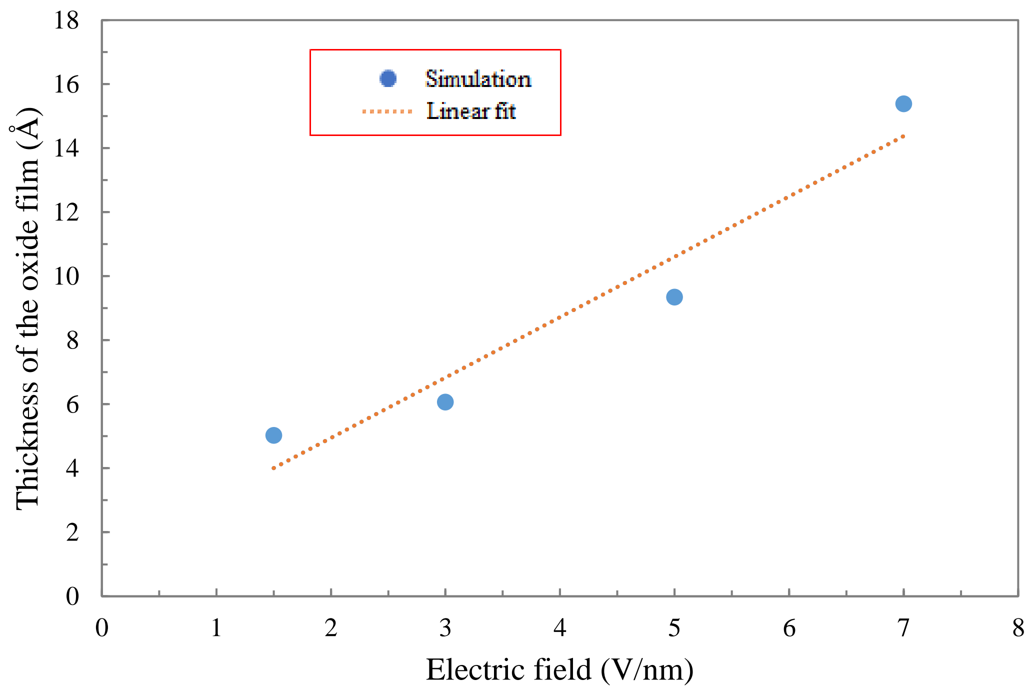

Figure 4.12 The thickness of the oxide film as a function of the electric field at 400 ps.

The progression of the H_2O and H_3O^+ over time for the various electric fields is presented in Figures 4.13 and 4.14. More dissociations of the water molecules occur when the electric field is higher. The same feature is observed for the formation of H_3O^+. Increasing the electric field, it promotes the formation of H_3O^+ from protons and H_2O. It has also been observed that the number of oxygen atoms present in the oxide film follows an identical trend for all the electric fields (Figure 4.15).

Since the oxide structure is stoichiometric and mainly composed of silicon and silicon dioxide (SiO_2) as described in chapter 2, the O/Si ratio should be near 2. From Table 4.1, it can be seen that the O/Si stoichiometry values calculated for the second monolayer in the oxide film at 400 ps are far away from the value of the native oxide. The probable reason for this could be the short MD run, which produces thinner oxide film. Sigmon *et al*. explained that the O/Si ratio varies as a function of oxide thickness, and the O/Si stoichiometric is less than 0.5 for a thinner oxide film (<14 Å) [254].

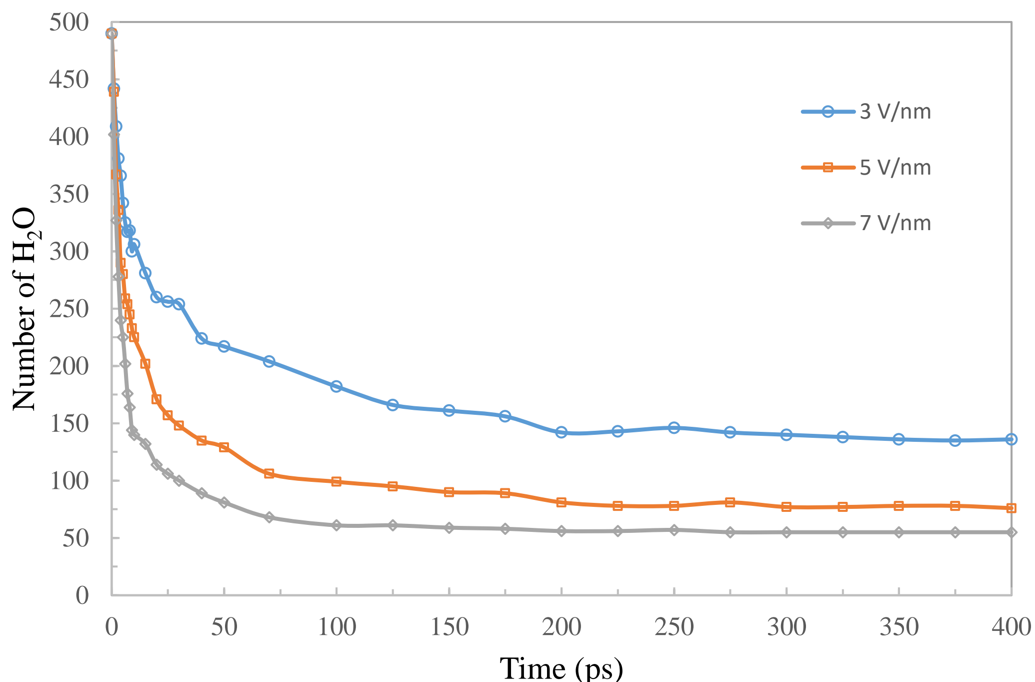

Figure 4.13 Evolution of the H_2O molecules time for the different electric fields.

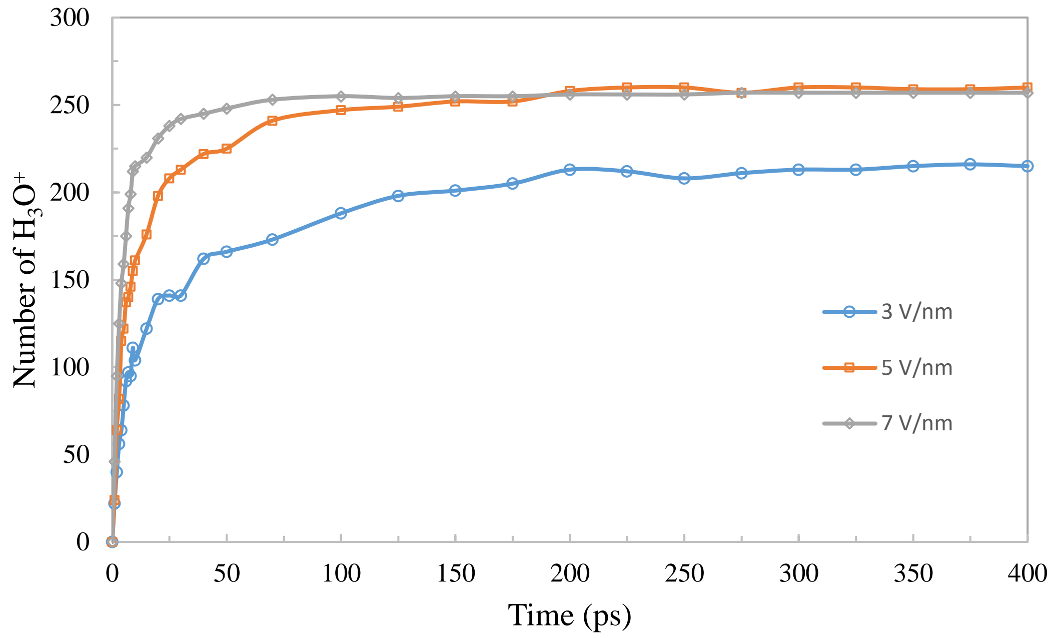

Figure 4.14 Evolution of the H_3O^+ over time for the different electric fields.

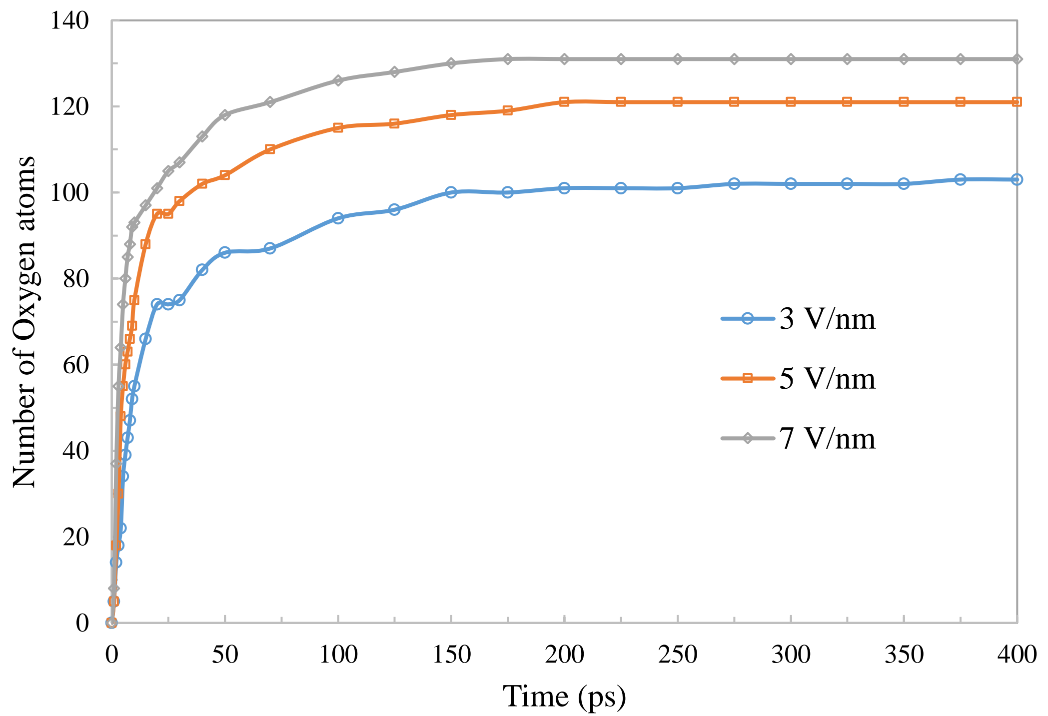

Figure 4.15 Evolution of the number of oxygen atoms over time in the oxide film for the different electric fields.

Table 4.1 O/Si stoichiometry in the oxide film.

	Native oxide	3 V/nm	5 V/nm	7 V/nm
(O/Si) ratio	2.00	0.50	0.50	0.60

The pair correlation functions g (r) (Figure 4.16) show that the Si-O bonds have a first peak at 1.575 Å for all electric-field intensities. A second peak appears to emerge at 2.225 Å for the electric field of 3 V/nm, whereas a second peak appears to emerge at 2.175 Å for the electric fields of 5 V/nm and 7V/nm. All these observations lead to the conclusion that the oxide films have an amorphous structure, and the structural and chemical properties of the oxide films do not depend on the electric fields.

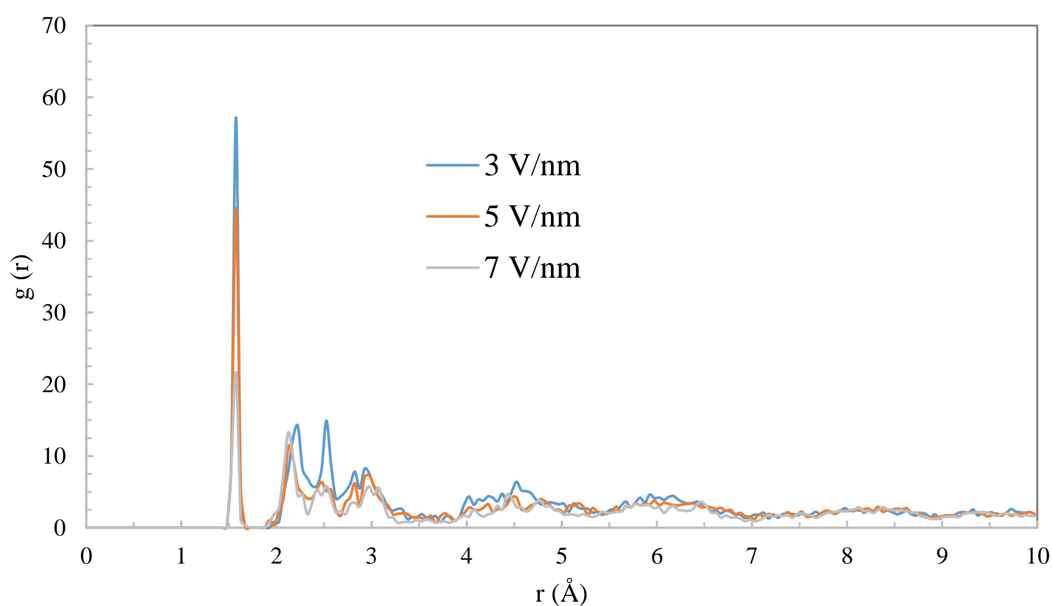

Figure 4.16 RDF of Si-O pairs in the oxide film for different electric fields after 400 ps.

4.4 Effect of the relative humidity (RH)

Another parameter that plays an important role in the NEL process is relative humidity. The thickness of the water layer adsorbed on the surface depends on the relative humidity (RH). M. Luna *et al.* studied the effect of the relative humidity on the thickness of the adsorbed water and established a relationship between them [218]. They found that the thickness of the adsorbed water layer increases with the relative humidity, and the increment is higher for the larger RH values. Considering the formulation given by them (see appendix A), the simulation models are constructed with the silicon substrates covered by the different water layers. Then the oxide growths concerning the relative humidity during the oxidation process are observed. Table 4.2 shows the thickness of the adsorbed water layer for the constructed simulation models. By applying an electric field of 5 V/nm for a time of 400 picoseconds, Figure 4.17 represents the evolution of the oxides with respect to the different relative humidity (20% to 90%).

Table 4.2 The thickness of the water layers for different simulation models.

Relative Humidity (~%RH)	Water layer thickness (Å)
20	0.94
30	1.10
40	1.25
50	1.88
60	2.50
70	3.13
80	5.00
90	10.00

The oxidation occurs in various humid environments, and the RH values influence the height of the oxide film. Since higher humidity provides a large amount of adsorbed water, it produces a high concentration of oxyanions under the influence of an electric field. The oxyanions under the stamp and the lateral oxyanions diffusion on the Si surface affect the oxide growth considerably [255].

Figure 4.18 shows two different characteristics of oxide growth for various RH values. In the range of 20-40% RH, there are no significant changes in oxide height. This is because the amount of adsorbed water on the surface does not vary much for the lower values of RH. Beyond 40% RH, a linear characteristic of the oxide growth with the relative humidity is observed. The height of the oxide film rises from 2.8333 Å to 9.3503 Å on varying the RH (40% to 90%) with a growth factor of 0.13 Å/%. The same behavior was experimentally observed by Cristiano Albonetti *et al.* [7].

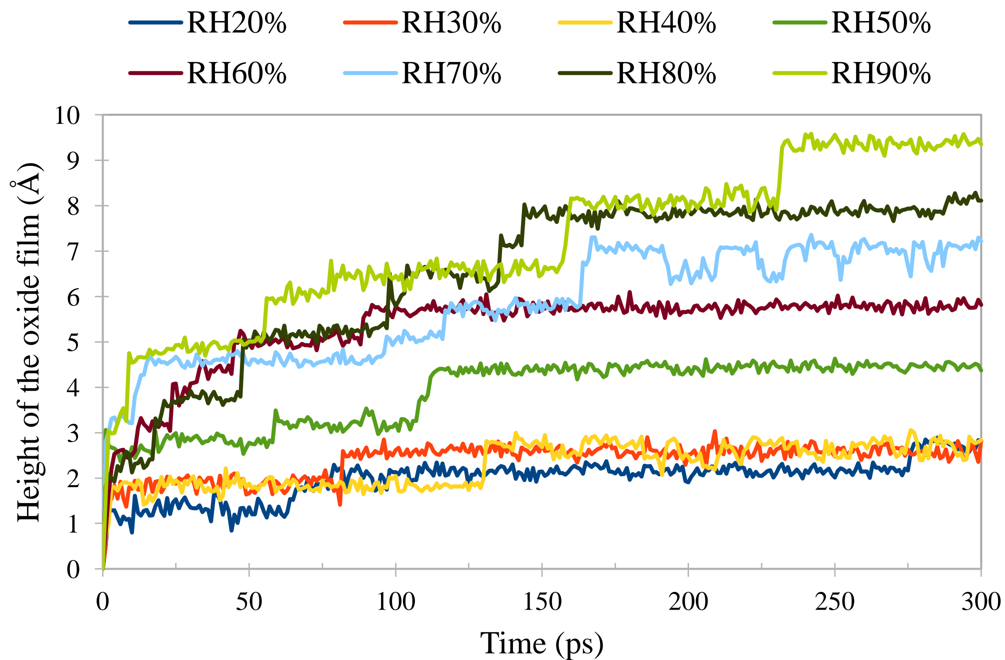

Figure 4.17 Evolution of oxide film for different relative humidity (RH) with an applied electric field of 5 V/nm.

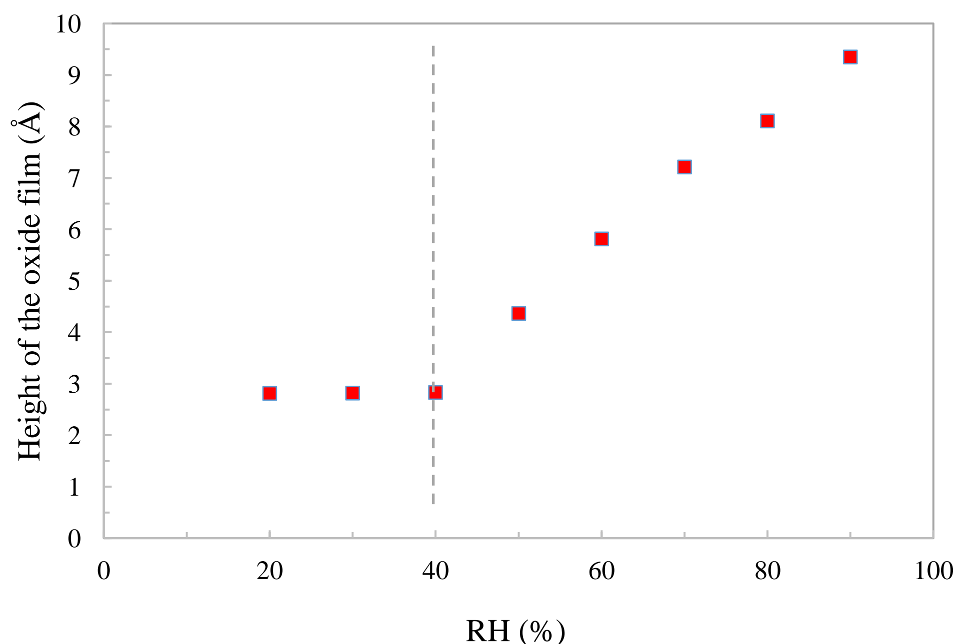

Figure 4.18 The height of the oxide film as a function of the relative humidity with an applied electric field of 5 V/nm.

4.5 Summary

The ReaxFF MD simulation results explain the oxidation process of silicon (100) with an applied electric field, which is the main mechanism of nanoelectrode lithography. The adsorption of the water molecules on the Si surfaces and their dissociation into OH^- and H_3O^+ at the first stage of the process are also observed. Again, the OH groups are adsorbed on the Si surfaces, and then dissociate to release the O atoms, which form the Si–O–Si bonds, making the surfaces oxidized. The higher oxidation rate is found at the very beginning, and the rate slows down over the period. The accumulation of the oxygen atoms in the oxide film is found in a layer by layer fashion. The number of the oxygen atoms is observed less in the deeper positions of the oxide film, and the RDF analysis suggests the oxide film as an amorphous structure. The charge distribution of the atoms has also been analyzed. It is observed

that there is a linear dependence of the oxide thickness with the intensity of the electric field. The higher electric field can make the surface more oxidized. A similar characteristic is also observed for the higher RH values. These results are in good agreement with the experimental observations.

Chapter 5 MD Simulated Study of Substrate Orientational Effects on NEL and Experimental Validation

5.1 Introduction

In the previous chapter, the reactive force molecular dynamic study of the NEL process has been investigated where the oxide growth mechanism and the influence of the electric field and the relative humidity have been assessed. However, the orientation-dependent investigation, which is an important parameter in the kinetic mechanism for the oxidation process, is still missing. In the case of thermal oxidation, a number of experimental studies have revealed that the crystal orientation has a dominant effect on the oxidation process [256-259]. They showed that the orientation of the substrate surface renders a complex effect on the thermal-oxidation rate. Hence, the choice of crystallographic orientation of the substrate surface becomes more critical in nanofabrication industries. In this chapter, ReaxFF MD simulations are employed to investigate the substrate orientation effects in the NEL process, which include the comparison between the substrates with different orientations in terms of oxidation kinetics, charge distribution, oxide film structure, and growth characteristics under different electric field intensities. Finally, the AFM experiments are carried out to validate the simulation results.

5.2 Analysis of the oxidation kinetics

An electric field of 7 V/nm (i.e., 7 V bias voltage) has been applied between the reflecting wall, and the substrate for a duration of 400 ps at 300 K. After the end of the simulation, some adsorption and dissociation of water on the Si surfaces have

been observed which finally formed an oxide film (shown in Figure 5.1). The first penetration of oxygen atom to form Si-O-Si bond occurs at 1.1 picoseconds in Si (100) surface, whereas at 1.4 picoseconds in Si (110) surface and 1 picosecond in Si (111) surface (shown in Figure 5.2). From Figures 5.3 and 5.4, it can be noticed that the adsorption and the dissociation of water for the three surfaces have identical trends. In the early stages, the reactions take place very fast. After that, the oxidation process becomes slow due to the ionic charges of the oxides, as explained in chapter 4.

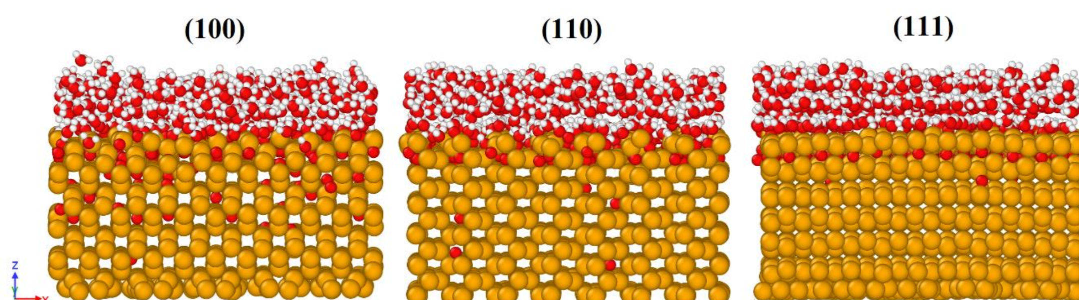

Figure 5.1 Side views of the three systems after 400 ps at 300 K.

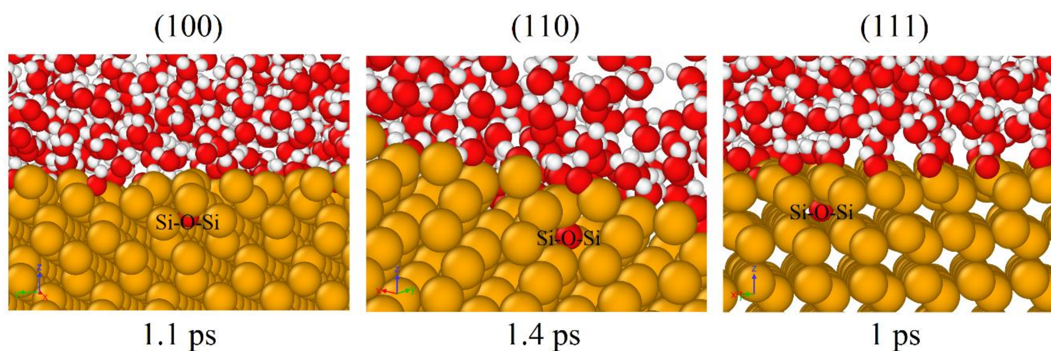

Figure 5.2 First formation of Si−O−Si.

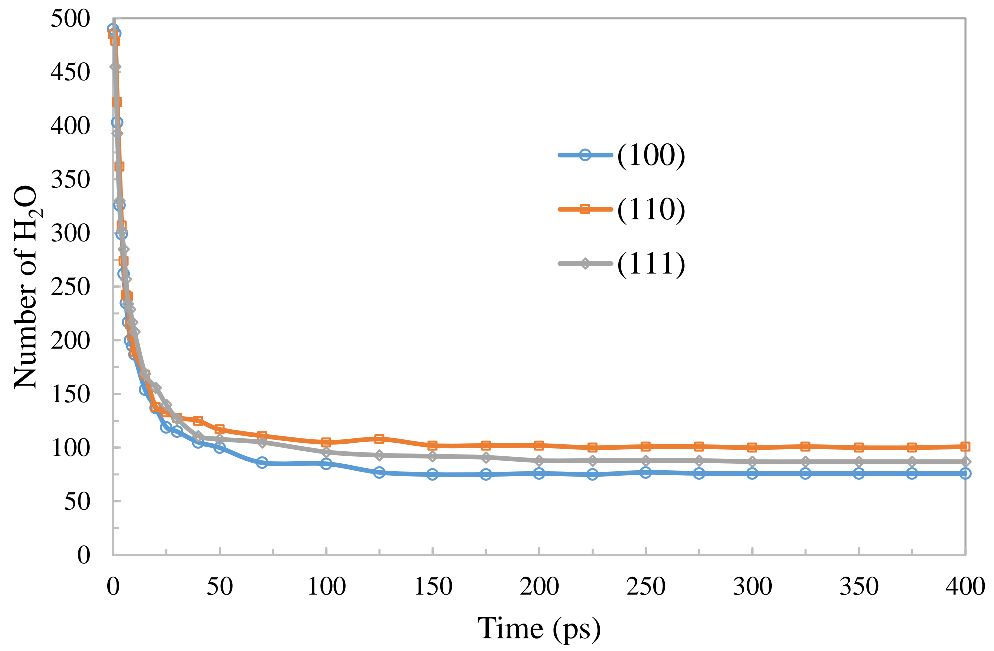

Figure 5.3 Number of H_2O in the three systems.

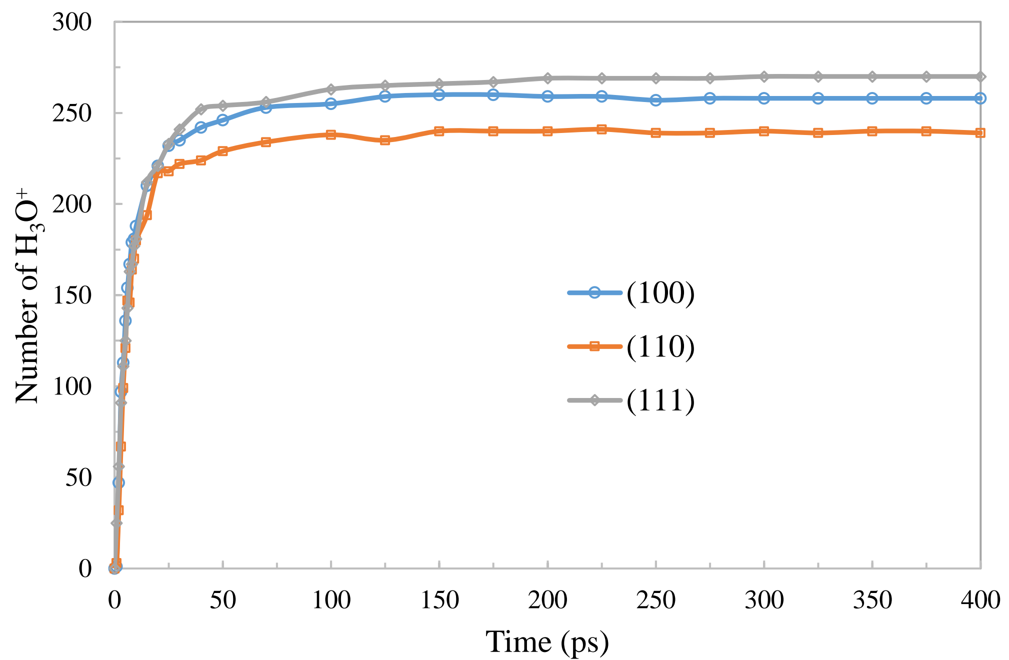

Figure 5.4 Number of H_3O^+ in the three systems.

The same characteristics can be explained in Figure 5.5, which depicts the evolution of the thickness of the oxide film for the three silicon substrates throughout

the simulation. The oxide thickness is determined as the difference between the position (along z) of the deepest oxygen atom in the oxide film and the position of the silicon atom at the top. For all three cases, there is a quick increase in oxide growth at the very beginning and reaches more than 2.7 Å within 5 picoseconds. Then the oxide thickness shows a steady increase in a layer by layer fashion.

Once the oxygen atom reaches a certain depth, there is no more forward penetration until this layer is saturated. Hence, oxygen atoms fluctuate at this layer until its concentration in oxygen atoms reaches a certain value, after which oxygen atoms start to move to the next layer. It is also observed that the (110) substrate yields the highest oxide film thickness, whereas the (111) substrate yields the lowest oxide film thickness. At the end of the simulation, the thickness of the oxide films yields the order T(110) > T(100) > T(111). However, this order can be changed at lower electric field intensities that are discussed in section 5.3.

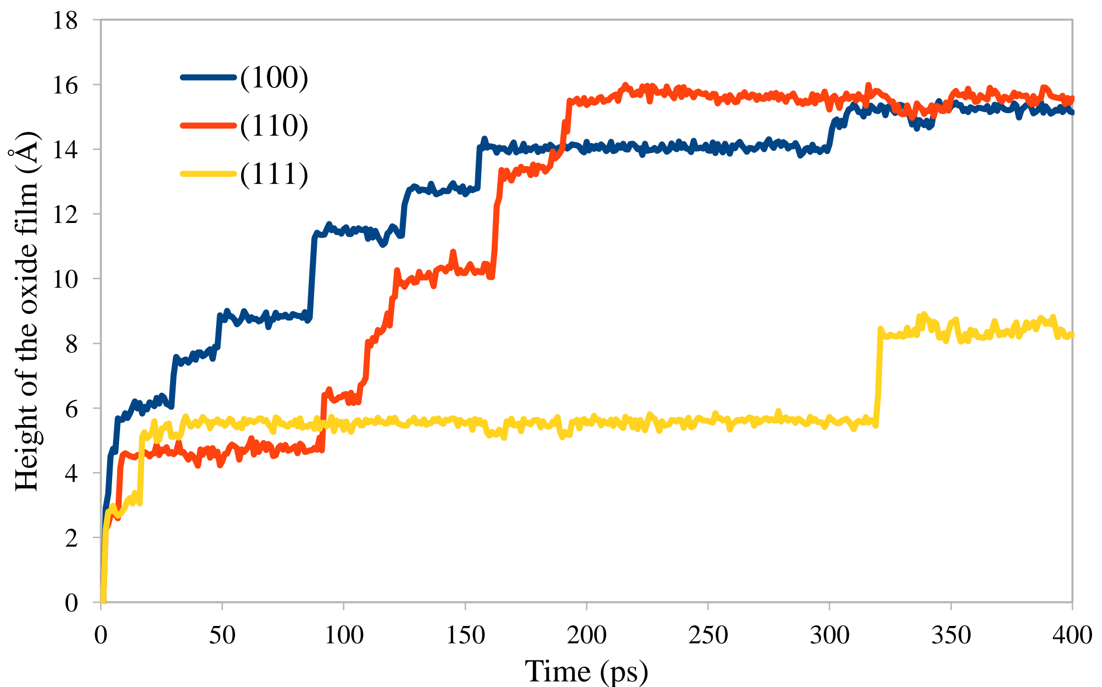

Figure 5.5 Evolution of oxide films for an electric field of 7 V/nm at 90% RH.

As two types of adsorption (molecular and dissociative adsorption) are observed, one has a significant contribution to the interaction process. From Figure 5.6, it is observed that molecular adsorption contributes more to the interaction process for the substrate (100) and (110), whereas dissociative adsorption dominates for the substrate (111). As shown in Figure 5.7, the three systems have quick oxidation at the beginning and then relatively slow oxidation. At the end of the simulations, they exhibit the order (100) > (111) > (110) in terms of the number of oxygen atoms (ML) diffused in the oxide film.

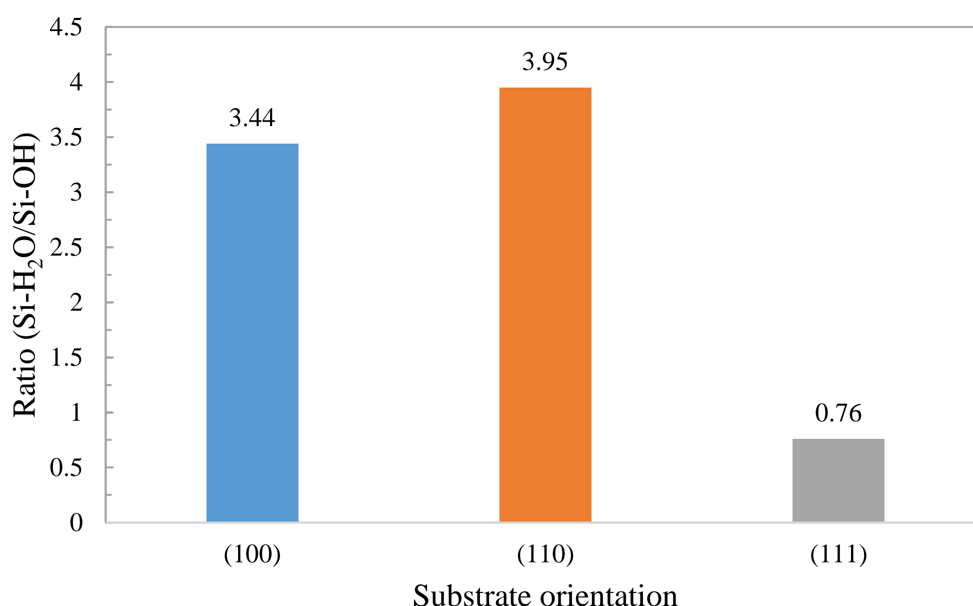

Figure 5.6 Ratio of the Si−H_2O number to the Si−OH number. The data are average of the last 100 ps.

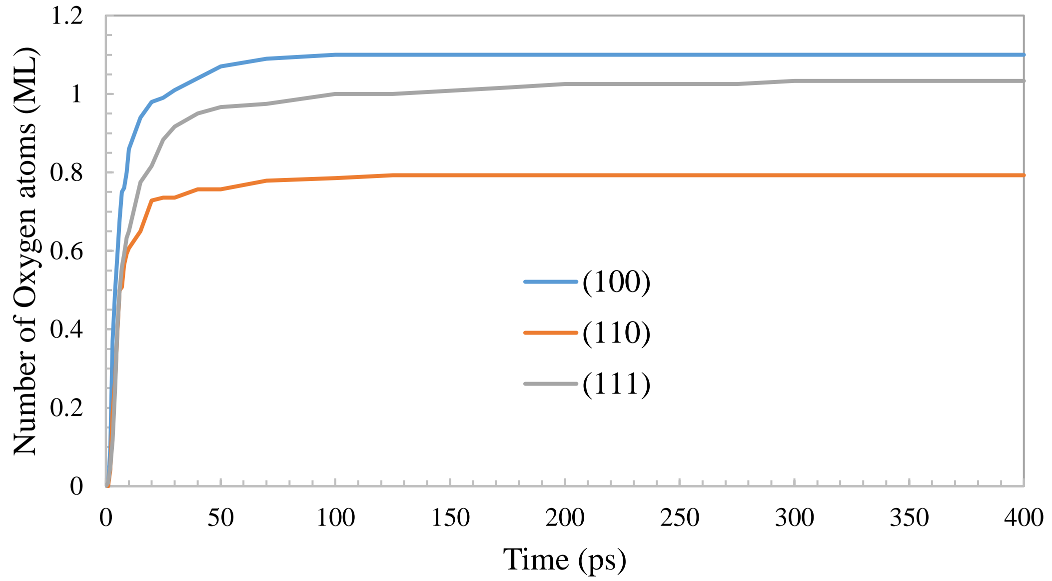

Figure 5.7 Evolution of the number of oxygen atoms over time in the oxide film.

The partial radial distribution functions (RDFs) are useful parameters to characterize the structure of the oxide films. From the partial RDFs shown in Figure 5.8, the first peaks for the mean Si–O bond length has been observed at a position of 1.575 Å, which is very close to the experimental values of ~1.61 Å [250, 251]. After that, some shapes with non-defined orders have been noticed, which suggests the structure of the oxide films is amorphous for all three silicon substrates. Figure 5.9 shows the oxygen distribution inside the oxide films where the oxygen atoms are counted every 0.4 Å sized bin. The zero position of z refers to the initial surface position and the numbers to the depth below the initial surface. The highest number of oxygen atoms (ML) is located at a depth of 0.8 Å, 1.6 Å, and 2.4 Å for the substrate (100), (110), and (111), respectively.

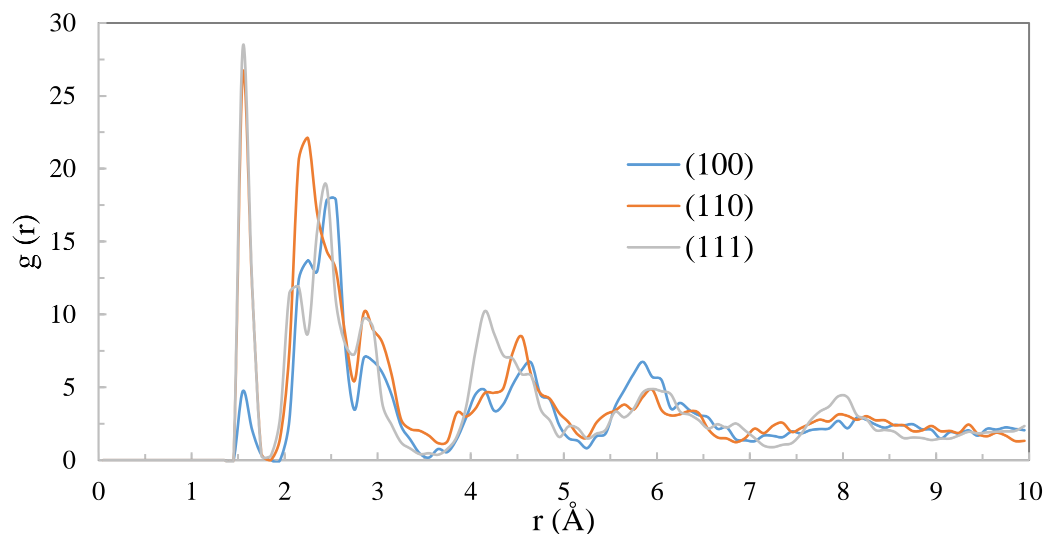

Figure 5.8 Partial radial distribution functions in the oxide film.

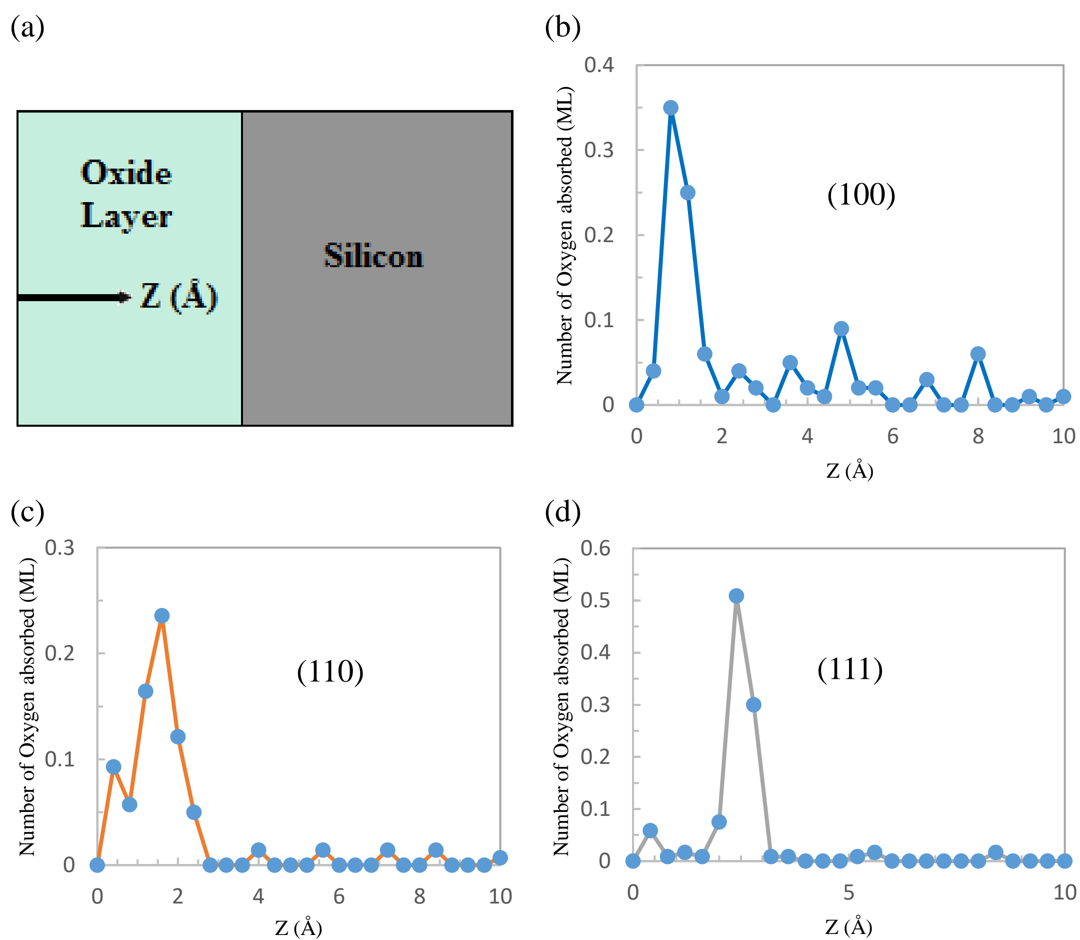

Figure 5.9 Oxygen atoms distributions inside Si substrates along the z direction at 400 ps.

The charges of the atoms outside the oxide film follow the same characteristics for all three crystallographic orientations. At the outside of the oxide films, the silicon atoms have the charges of around 0 *e*. The charges for the oxygen atoms (around -0.70 *e*) and the hydrogen atoms (around +0.30 *e*) are found very similar to the charges in bulk water. In the oxide zone, the silicon atoms have higher charges as the oxygen atoms surround them. From the charge distribution of the Si atoms (shown in Figure 5.10), it is observed that some of the top-surface silicon atoms in (100) and (110) planes are oxidized with the charges close to 0.63 *e*, while the top-surface silicon atoms have charges close to 0.45 *e* in (111) substrate. The average charge of the oxygen atoms in all three oxide films is found to be ~-0.45 *e*.

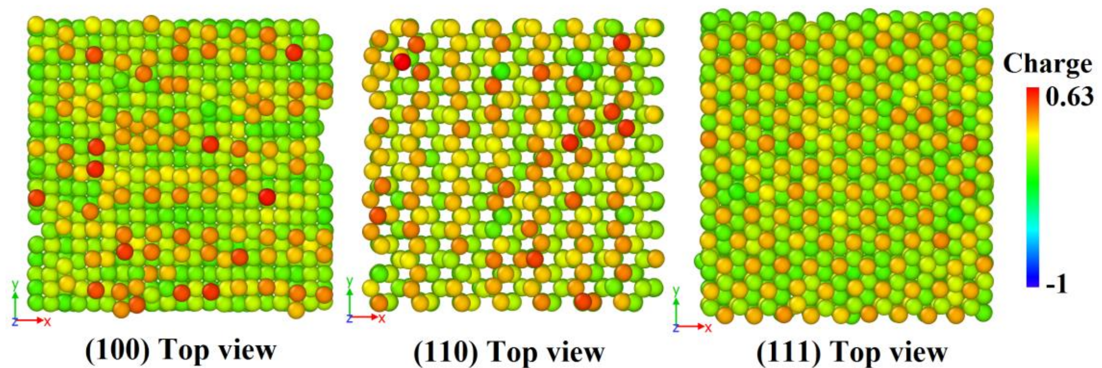

Figure 5.10 Mulliken charge distributions of the Si atoms for three crystallographic orientations at 400 ps.

5.3 Influence of applied electric field

The substrates present interesting features under different applied electric fields. Figure 5.11 shows the initial oxygen diffusion rates (number of oxygen atoms diffused per second into the oxide layer due to water dissociation), which are calculated for the first 5 picoseconds period. The (100) substrate has the highest initial

diffusion rate for either of these three electric fields, whereas the (111) substrate has the lowest initial diffusion rate at lower electric fields (3 V/nm and 5 V/nm). At a higher electric field (7 V/nm), the substrate (111) has a slightly larger initial diffusion rate to the substrate (110).

Again, there is a crossover in oxide thickness to T(110) > T(100) at 7 V/nm, while the other orientation maintains the same order (shown in Figure 5.12). At lower electric field intensities, the order yields T(100) > T(110) > T(111). The initial oxygen diffusion rate and the thickness of the oxide film increase with the increase of the electric field intensity. These types of behaviors have previously been observed for thermal oxidation of various crystallographic orientations of silicon [257-259].

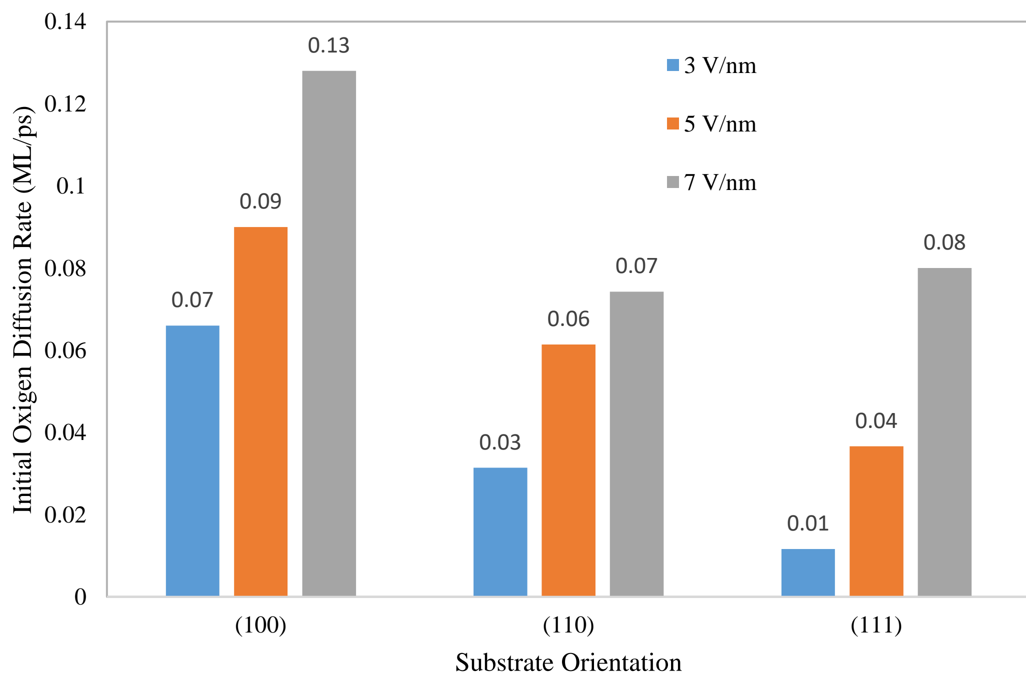

Figure 5.11 Rate of initial oxygen diffused in the surfaces for different electric fields.

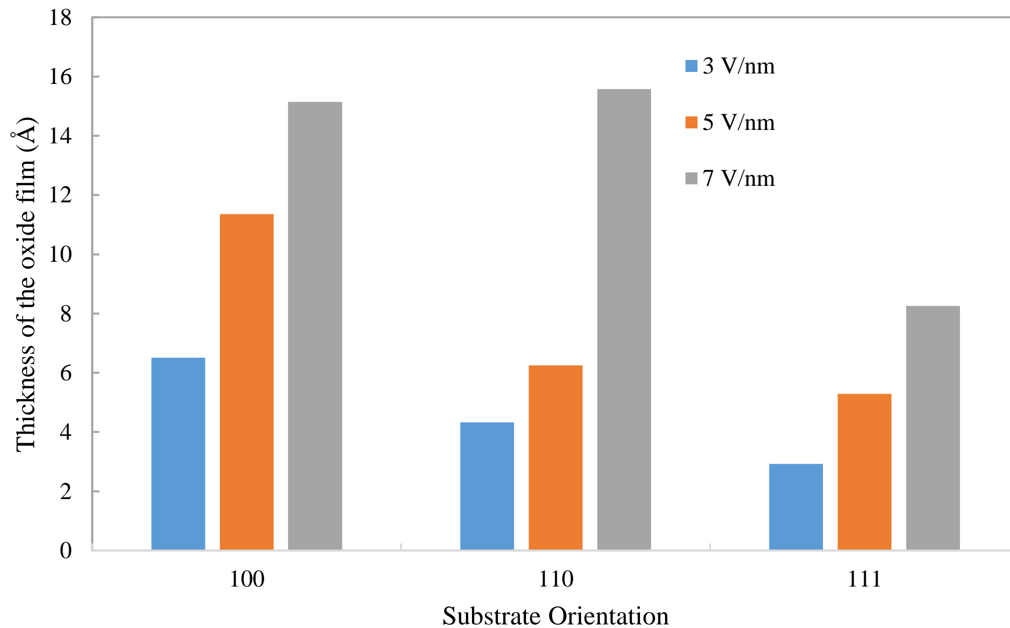

Figure 5.12 Thickness of the oxide films for different electric fields.

It can be seen that there is a correlation between the thickness of the oxide films and the substrate surface energies, which have been calculated in chapter 3 for three different oriented silicon surfaces with the ReaxFF potential function. As can be seen that the surface energy exhibits the same order as the order of the oxide film thickness, confirming that surfaces with higher surface energy are more reactive at lower electric field intensity (3 V/nm and 5 V/nm).

5.4 Experimental results

The experimental observation of the oxide growth for the ultra-short period is unfeasible. However, the oxidation experiment by using a commercial AFM (Bruker DI 3100, USA) with additional circuits to apply voltage pulses provides insights on the oxidation kinetics of low index silicon surfaces. A doped n-type silicon tip coated with Cr-Au has been used. The height and the radius of curvature of the AFM tip were

~20 μm and <50 nm, respectively. The silicon samples were Si (100) with a resistivity of $\rho \sim$ 10–15 Ω-cm, Si (110) with a resistivity of $\rho \sim$ 1–30 Ω-cm and Si (111) with a resistivity of $\rho \sim$ 1–20 Ω-cm. All the nanofabrication and observations were done in the AFM contact mode at room temperature.

Few short oxide lines have been generated on each sample by applying 7 V pulses and 3 μm/s of tip velocity at a relative humidity of 70% (the highest permitted value for the used AFM system). It should be noted here that an electric field of 7 V/nm used in the simulation refers to the bias voltage of 7 V as the gap between the reflecting wall and the Si substrate is 1 nm. Figure 5.13 shows the AFM topographic images and line profiles of the fabricated short oxide lines on different silicon substrates. The oxide height for (110) plane is found to be the largest (2.28 nm), while the height for (100) plane is found to be the lowest (1.49 nm). The (111) plane exhibits an oxide height of 1.73 nm. The same growth order has also been observed for a lower relative humidity of 44% and an applied bias of 12 V (shown in Figure 5.14). The averaged values were measured from the three arbitrary short lines for each sample. This result suggests that the variation in the relative humidity does not change the order of the substrate's orientations in terms of the oxide thickness. In addition, the literature does not show any substance to the assertion that resistivity of the substrate has an impact on the anodic oxidation process. Therefore, considering these facts, the thickness of the oxide films yields the order $T(110) > T(111) > T(100)$.

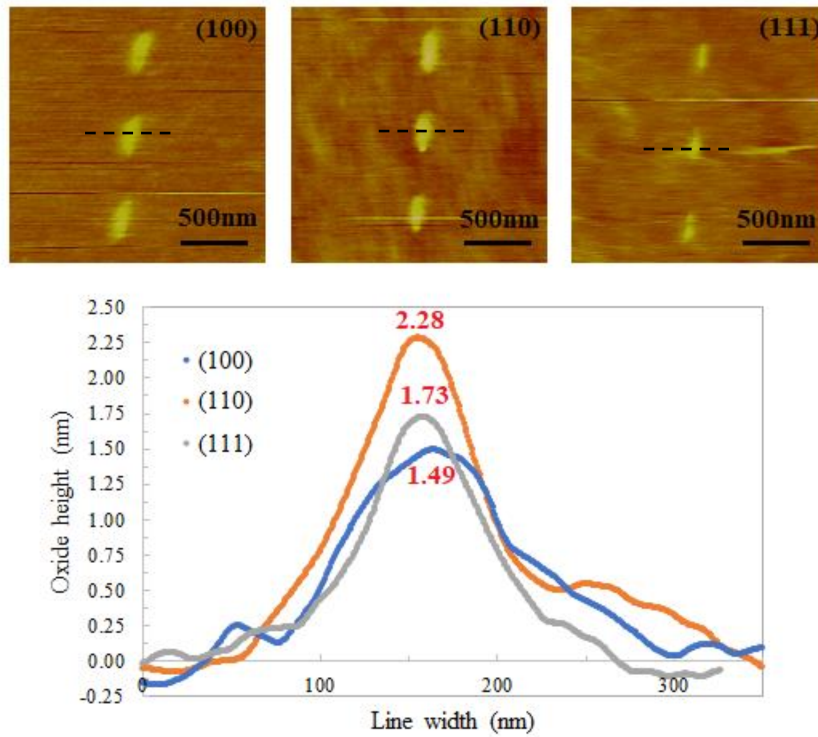

Figure 5.13 AFM images of nanostructures on different substrates and height cross-section along the lines marked in the images.

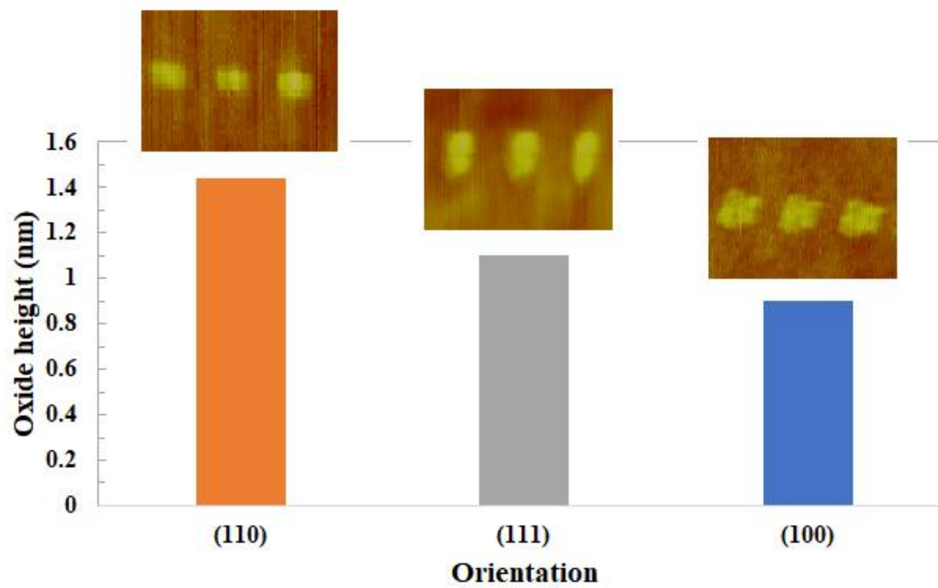

Figure 5.14 The oxide height for different substrates obtained with a bias of 12 V and 44% RH.

5.5 Possible explanation for the order of oxide growth

Previous studies on the orientation effect for thermal oxidation of silicon proposed some mechanisms which explain how the crystal orientations affect the oxide growth [257, 258, 260]. They established a correlation between the initial order of the growth and the density of atoms on planes parallel to the surface. It has been observed in section 5.2 that the water molecules react with the silicon at the interface and the oxygen atoms inserted to the Si-Si bonds, which eventually formed Si-O-Si bonds. The reaction sites are the silicon bonds at the surface, and therefore, the oxidation growth is proportional to the concentration of the reaction sites (areal density). Considering the number of reaction sites, the oxidation growth should follow the same order to the areal density of Si atoms, where the (110) plane has the highest areal density of Si atoms, followed by the (111) plane and then the (100) plane (shown in Table 3.1).

The activation energy could be another parameter that can influence the oxidation growth. The substrate with less activation energy has more oxidation growth and vice versa. J. R. Lagenza explained the phenomena and investigated the activation energy for different orientations [260]. It is expected that the parallel bonds react easily while the bonds with an angle to the surface react less readily. This is because of a steric hindrance offered by the silicon atom's position in the vicinity of the bond. Consequently, the reaction between the water molecule and a silicon bond depends on their relative positions. As the parallel bonds require less energy to react, the substrate plane with more parallel bonds has less activation energy. The plane (110) has parallel bonds, while the other two substrates have none. Again, the (100) plane has the bonds with a larger angle to the surface plane than that of the (111) plane. Considering these two observations, the activation energies follow the order $E(100) > E(111) > E(110)$.

As the areal density of atoms and the activation energy depend on the substrate orientation, these two parameters could be the main reasons for the variation of the oxide growth. Based on these two parameters, the oxide growth should follow the order T(110) > T(111) > T(100). The experimental results show that the oxide growth follows this order with a small difference between (100) and (111). From the MD simulation results, it has been seen a reverse order for these two substrates, while the (110) substrate remains the largest at 7 V/nm electric field. However, the differences between simulation and experimental measured values possibly relate to the empirical potential as well as different time and spatial scales of the process. Indeed, the atomic potential does not describe the surface reconstruction of the Si substrate. This would have changed the reactivity (surface energy) of the considered orientations as well as the order of the oxide growth. Further MD studies at longer simulation time are required to investigate these varieties of behaviors and to study which factors are responsible for these irregularities. Nevertheless, it requires very long computation times.

5.6 Summary

The effects of crystallographic orientations of substrates on the NEL oxidation process has been investigated for the (100), (110) and (111) surfaces of single-crystal silicon through ReaxFF MD simulations and experiments. Simulation results revealed that molecular adsorption of H_2O contributes more to the interaction process for the substrates (100) and (110), whereas the dissociative adsorption dominates for the substrate (111). The RDF analysis suggests the oxide film as an amorphous structure for all three crystallographic orientations. This study further demonstrated that the thickness of the oxide film exhibits the order T(100) > T(110) > T(111) at lower

electric field intensities. A crossover occurs at higher electric field intensity (7 V/nm) for the substrates (100) and (110). Besides, it is found that there is also a slight crossover in the initial oxygen diffusion rate to R(111) > R(110) at 7 V/nm. The initial order at lower electric field intensities was R(100) > R(110) > R(111). The oxygen diffusion rate and the thickness of the oxide film increase with the increase of the electric field intensities. AFM oxidation experiment shows the different order of the oxide thickness for the (100) and (111) with a small difference. However, molecular dynamics simulations were performed for 400 picoseconds only, while experimental investigations show large-scale features. Therefore, further studies are required with a long simulation run time to elucidate some of the many unknowns concerning the origin of the anomalous features.

Chapter 6 Nanoelectrode Lithography by Flat Stamps

6.1 Introduction

One of the essential factors in the NEL system is the requirement of a conductive layer deposition on the stamps. Previous studies show that the researchers have used several stamps with multiple protrusions in NEL experiments. They used a layer of gold/platinum to make these patterned surfaces conductive. However, the use of gold/platinum as a conductive layer of the stamps makes them a bit expensive. Other conductive materials such as brass can be useful as the stamps due to their high elastic modulus and high breaking strength. They can also reduce the process steps such as deposition of the conductive layer. In this chapter, a prototype of the NEL system is developed. A new type of conductive stamp is fabricated and used in the NEL experiments to examine their applicability. It is also shown how the oxidation is improved by placing the hydroxyl-terminated polystyrene (PS-OH) layer on the sample surface.

6.2 NEL system prototype: design and implementation

Figure 6.1 shows the panoramic view of the prototype system developed to perform the NEL experiments. This system enables to do lithographic experiments in a short time, which consists of several elements given below:

6.2.1 Three axes translational displacement

The lithographer has three axes system, which allows three degrees of movement commonly refer to X axis, Y axis, and Z axis. The resolution of the

movement of each axis is 0.5 µm. All the movements of the three axes are controlled by using a computer through a controller.

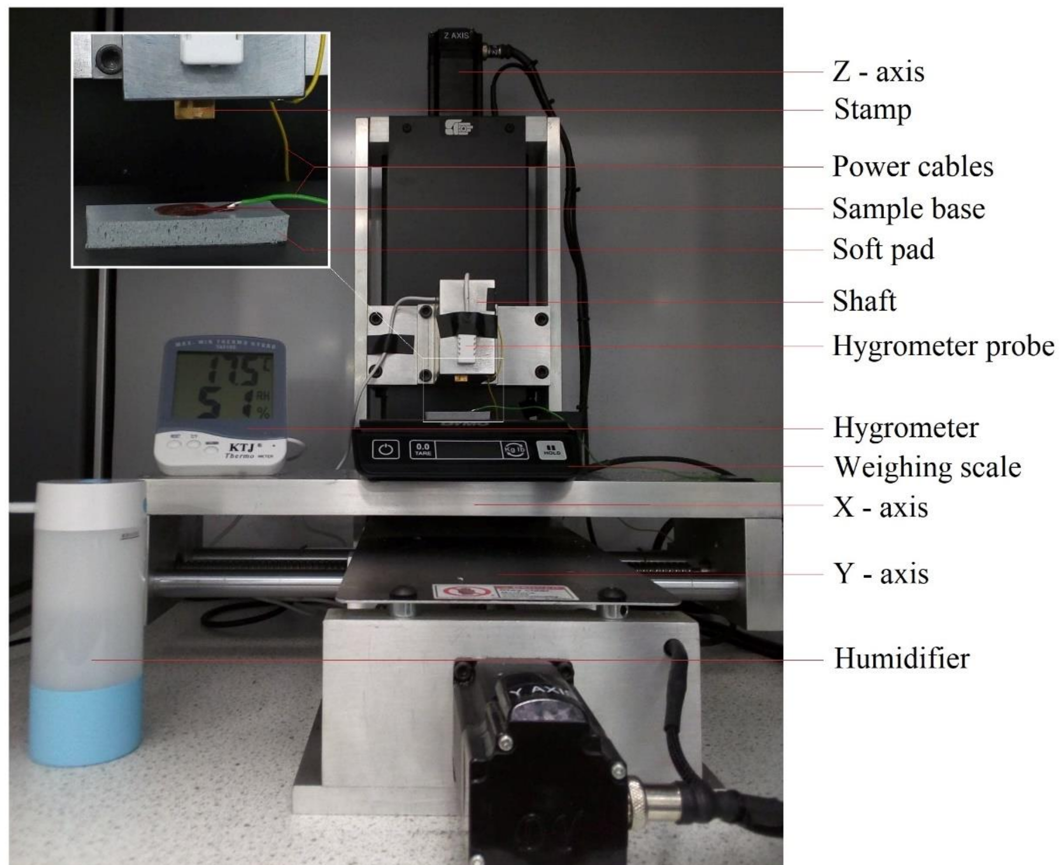

Figure 6.1 Panoramic view of the NEL prototype system.

6.2.2 Sample metal base

The sample is placed on a metal base using silver conductive paint to provide good electrical contact between the silicon substrate and the base (Figure 6.2). The metal base has two degrees of freedom. It can move along the X and Y axis. These movements allow the correct positioning of the sample relative to the stamp. The metal base is connected to the positive terminal of the power supply via a cable. A rubber pad is used under the sample base to allow a homogeneous distribution of the pressure applied to the sample.

6.2.3 Stamp holder

The stamp is located at the top part of the system with a shaft. The shaft so as the stamp can approach the sample along the Z axis with submicrometric precision. This movement allows contacting between the sample and the stamp. The stamp is connected to the negative terminal of the power supply through a cable.

6.2.4 Humidity controlling and measurement

The mechanical system is placed in an enclosure, and a humidifier is used to maintain the required humidity. The hygrometer (±1% accuracy) measures the relative humidity value.

6.2.5 Power supply and weighing scale

A DC power supply is used to apply the voltage between the stamp and the sample. A weighing scale is placed under the sample base to measure the force exerted to the stamp.

6.2.6 Computer control

A controller (Minitech) with a Mach3 (artSoft, USA) software is used to control the three axes movement. This controlling system is usually used in a micro-milling system. The interface of the control software is shown in Figure 6.3. The movement can be controlled manually by using various types of jogging (Continuous or step mode) or programmed controlled defined by a G Code part program.

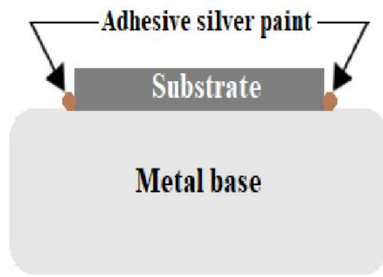

Figure 6.2 Sample metal base.

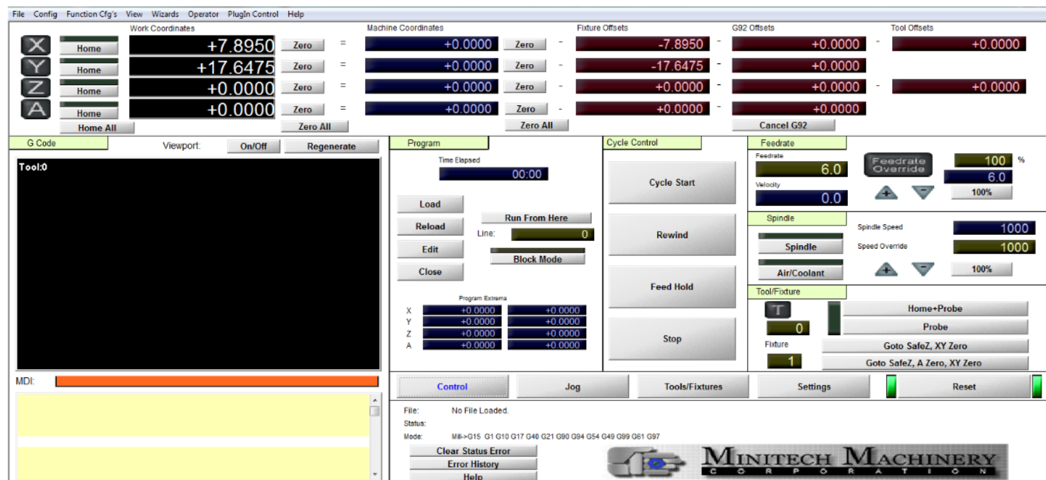

Figure 6.3 Software interface.

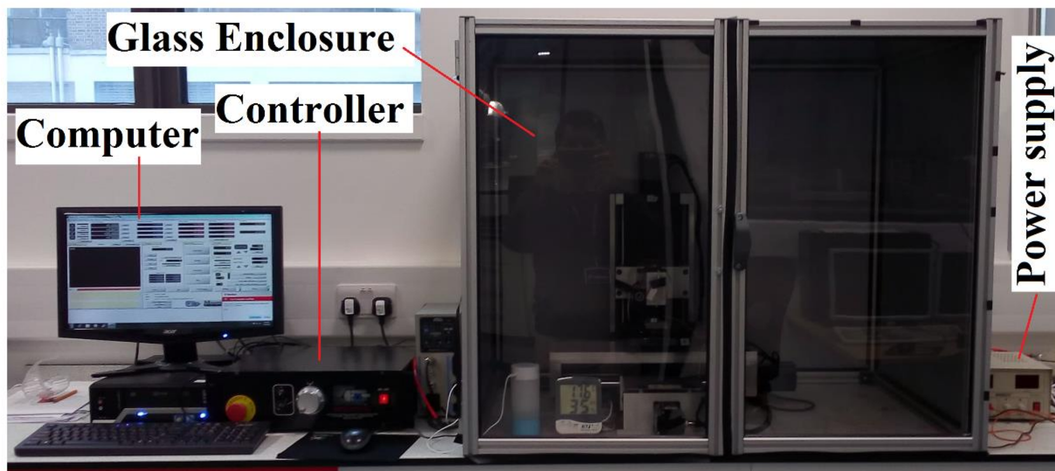

Figure 6.4 System enclosure, power supply, and the Computer control system.

6.3 Stamp preparation

Polycarbonate DVDs (Digital Versatile Disk) can easily be prepared as they have prefabricated nanostructures on them. They are excellent stamps for NEL experiments and have previously been used by many researchers [5, 8, 156]. On the other hand, Brass is a copper-zinc alloy, with copper (60 - 63%), zinc (35.5%), Fe (max 0.35%), Pb (2.5 -3.7%) and other components (max 0.5%). Good corrosion and wear resistance, excellent electrical and thermal conductivity make brass materials suitable for electric and electronic industries. Therefore, a polycarbonate (DVD) stamp is chosen to verify the capability of the implemented NEL system by comparing it with the previous results. Then an experiment is carried out with brass stamp to observe their feasibility in the NEL system.

6.3.1 Preparation of the polycarbonate stamp

To make a polycarbonate stamp, a blank commercial DVD-R has been used. The blank DVD-R composed of spiral guide grooves with a periodicity of 780 nm, a 350 nm linewidth at half height, and a 100 nm depth. The DVD-R has two polycarbonate substrates that are united by a reflective metal layer (aluminium), as shown in Figure 6.5. The two substrates have been separated first. Then the polycarbonate with the conductive metal layer has been cut with the desired size by using a sharp scissor. There is a deformation at the edge of the stamp after cut by a scissor. Hence, the size of the stamp has been made larger than the substrate to avoid edge-related defects. To clean the stamp, it has been immersed in an ethanol solution for 3 minutes in ultrasound. It has been then rinsed with deionized water and dried with compressed N_2 gas. The stamp surface was inspected by a tapping mode atomic

force microscope (DI Dimension 3100) with a doped n-type silicon tip (coated with Cr-Au). The height and the radius of curvature of the AFM tip were ~20 μm and <50 nm, respectively. All the AFM images were acquired with this AFM in the remaining chapters. Figure 6.6 shows the images of the stamp and the profile of the motifs.

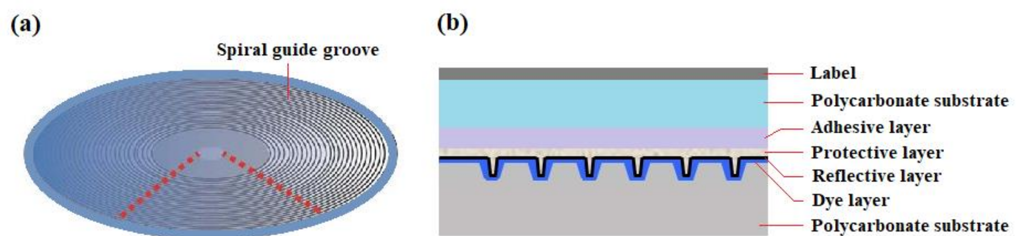

Figure 6.5 Schematic of a conventional DVD-R. (a) Spiral guide grooves. (b) Internal structure.

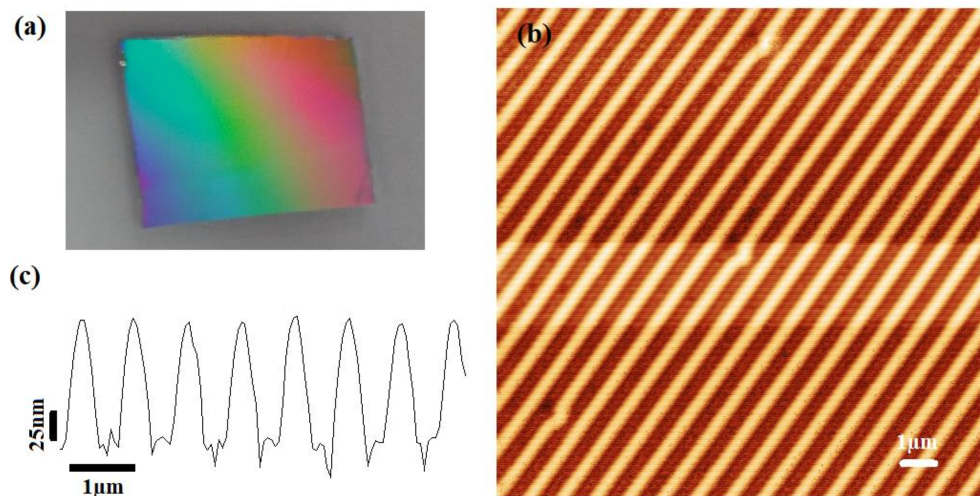

Figure 6.6 (a) Image of the stamp peeled off from a DVD-R. (b) AFM image shows the surface morphology of the motifs. (c) Profile of the motifs.

6.3.2 Fabrication of brass stamp with SPDT process

Single-point diamond turning (SPDT) has been exploited to fabricate the structures on the brass surfaces. The machining processes were carried out on a 3-axis ultra-precision diamond turning machine, which is equipped with an aerostatic bearing spindle and linear slides. The workpiece is clamped on the spindle by vacuumed air. Two different single-crystal diamond tools from Contour Fine Tooling were used in the facing cut to generate an ultra-precision substrate surface and nanostructures on the surface, respectively. The diamond tool used for the facing cut has a nose radius of 0.5 mm, a rake angle of 0˚, and a clearance angle of 15◦, respectively. A zero-rake sharp point diamond tool (V-shaped) was used for the fabrication of microstructures. The tool geometry and the machining conditions are listed in Table 6-1. No coolant lubricant was used during the machining process. As shown in Figure 6.7, the turning was performed on the brass stamp with a dimension of 10 x 10 x 5 mm^3. The shape of the structures was spiral lines with 2 μm apart.

Table 6.1 Machining condition and tool geometry.

Conditions	Flat turning	Patterning
Tool material	Diamond	Diamond
Workpiece material	Brass	Brass
Tool radius	0.5 mm	0.1 mm
Rake angle	0 degree	0 degree
Clearance angle	15 degree	57 degree
Feed rate	2 μm/rev	2 μm/rev
Depth of cut	2 μm	2 μm
Spindle speed	500 rpm	500 rpm

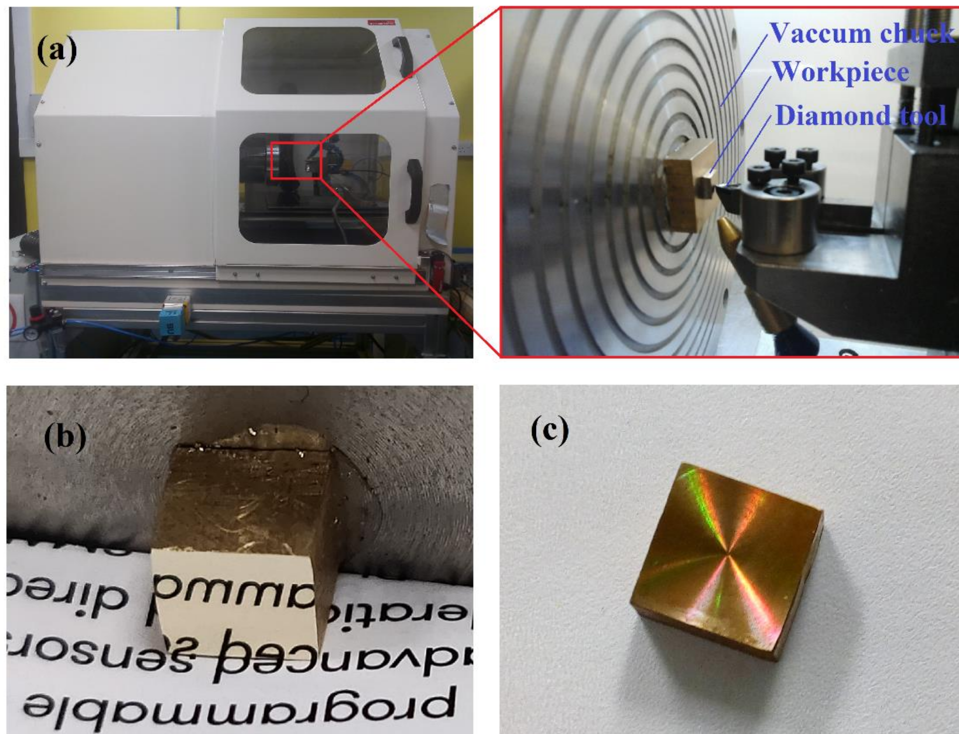

Figure 6.7 Fabrication of brass stamp with SPDT. (a) Machining set up. (b) Brass stamp after flat turning. (c) Brass stamp after microstructure fabrication.

The AFM images and the profile of the structures are shown in Figure 6.8. It has been observed that some cutting chips are accumulated and remain at the edges of the grooves, which from burrs (Figure 6.8a-b). Some of the burrs have heights of >100 nm, which can make the inhomogeneous contact between the stamp and the substrate during the oxidation process. The fabricated parallel lines have a periodicity of 2 μm with an average height of ~380 nm (Figure 6.8c). The surface texture on the top of the motif is shown in Figure 6.8(d), where the maximum variation of the peak of the nanostructures is measured to be 13 nm.

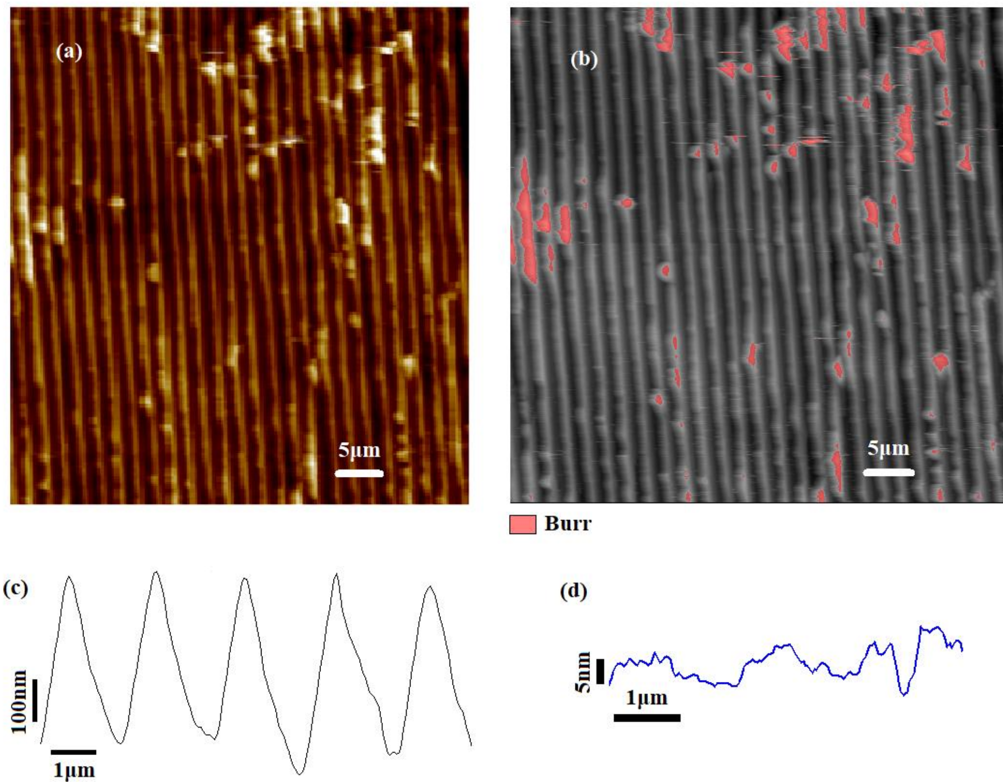

Figure 6.8 (a) AFM images of the fabricated brass structures. (b) Burrs are marked to visualize clearly. (c) Profile of the fabricated structures. (d) Surface topography on the top of a motif.

There are many factors influencing the burr formation, such as cutting speed, tool geometry, feed rate, undeformed chip thickness, and material properties of the workpiece [261]. G. Li *et al*. found that the burr formation during diamond turning of the brass materials at the smaller grating pitch (~2 μm) mainly results from the material metallographic inhomogeneous properties (the uneven proportion of α and β metallographic) [262]. The α metallographic is the solid solution of zinc in copper, which maintains a face-centred cubic crystal lattice. While the β metallographic is the intermetallic non-stoichiometric copper-zinc compound with body centre cubic crystal lattice. Less burr formation occurs with the more β metallographic in the brass.

6.4 Nano-patterning with polycarbonate stamp

6.4.1 Preparation of the samples

The samples used in this experiment were cleaved from a p-doped silicon (100) wafer of 4-inch diameter with a resistivity of 10-15 Ω-cm. The cleaved samples then have been gone through an RCA-1 cleaning process. Cleaning of these samples is very important since any contaminant adhered to the surface prevents contact between the stamp and the sample, and the oxidation in that region. The recipe for the RCA-1 cleaning is a solution of 1 part of NH_4OH (29% by weight of NH_3), 1 part of aqueous H_2O_2 (hydrogen peroxide, 30%) and 5 parts of deionized water. All the steps for RCA cleaning were performed in a place, which is located under an exhaust fume hood. The steps are as follows:

- The samples are immersed in the solution for an ultrasonic cleaning for 10 minutes. This process is repeated thrice.

- After that rinsing with DI water for 5 minutes.

- Finally, the samples are blown-dry with an N_2 gas jet.

The cleaning process increases the hydrophilicity of the surface as the solution creates a high density of hydroxyl groups on the silicon substrates. Figure 6.9 (a)-(b) shows the sample surface before and after the cleaning process, which clearly indicates the enhanced hydrophilicity. The cleaning steps remove the organic residues and the particles that ensure a low particle density (0.3 particles / μm^2) surface contaminants, as can be seen in Figure 6.9 (c).

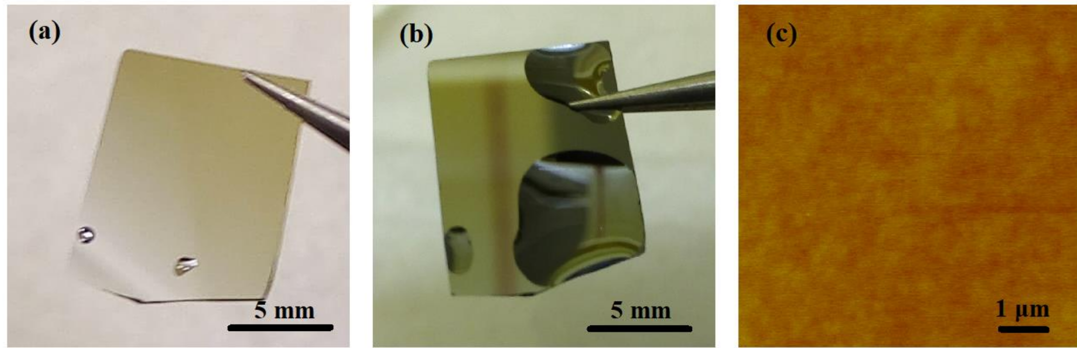

Figure 6.9 RCA cleaning of the sample. (a) Less water droplets were adhered to the sample before cleaning. (b) More water droplets were adhered to the sample after cleaning. (c) AFM topography image of silicon after the cleaning process.

6.4.2 Oxidation process and results

To perform the oxidation process, the polycarbonate stamp was placed in contact with the substrate. A pressure of 1 N was exerted uniformly on the stamp to make good contact. A voltage of 36 V has been applied for 1 minute at ambient temperature under relative humidity conditions of ~70%. Figure 6.10 shows the AFM images of the sample with a region of 11.4×11.4 μm^2 that contains 18 lines and the profile of the oxide lines after the oxidation process.

It can be seen that the fabricated silicon oxide lines maintain the periodicity of the original stamp of 780 nm, being the average height of these oxide lines of 0.7 nm. The heights of the structures were measured with respect to the bare silicon substrate. The full width at half maximum (FWHM) of the oxide lines is measured to be ~154 nm, which is smaller than the motifs of the 400 nm stamp. This is because of the less force applied so that only the upper part of the conductive pattern of the DVD stamp (which is narrower than the base) came into contact with the Si substrate to generate oxide patterns.

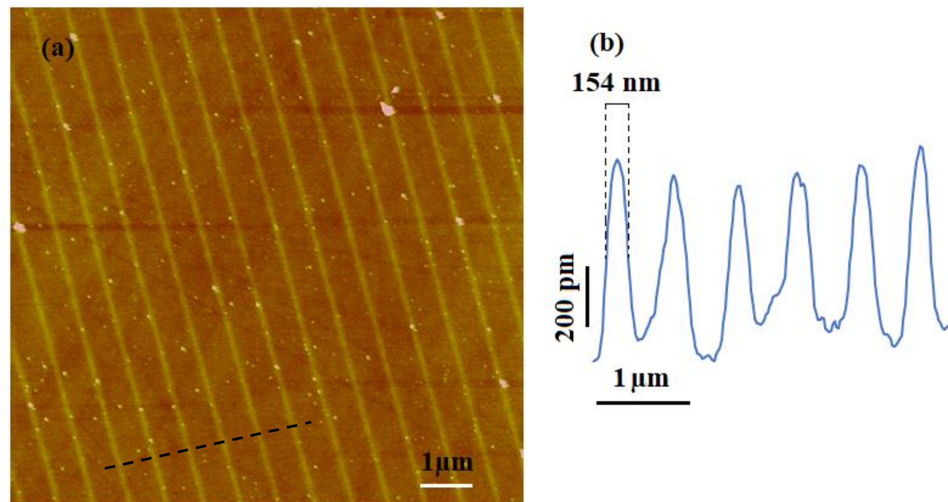

Figure 6.10 (a) AFM topography images of the oxide lines. (b) Profile of the oxide lines in the region marked by the line drawn in figure (a).

In 2003, Cavallini and his collaborators carried out a similar experiment with a polycarbonate stamp (shown in Figure 6.11) [5]. Their results showed the possibility of replicating the bits of a DVD with a height of approximately 0.7 nm and a width of ~100 nm (shown in Figure 6.11d). The aspect ratio of these structures would then be 0.007. Nevertheless, the geometry of the structures created on the silicon surface did not correspond to the geometry of the stamp motifs (Figure 6.11b). Considering these results as a reference, it is seen that the newly build NEL system can produce better pattern transfer without any distortion. Moreover, the NEL produces oxide at a slower rate than the growth rate obtained in AFM oxidation. The protrusions of the stamp are almost flat, whereas an AFM tip has a curvature of <50 nm. Because of the higher curvature, the AFM tip has higher effective electric field underneath, which makes the oxidation diffusion barriers lower [5]. In addition, the height and the width of the oxide lines can be increased by allowing more exposure time [5].

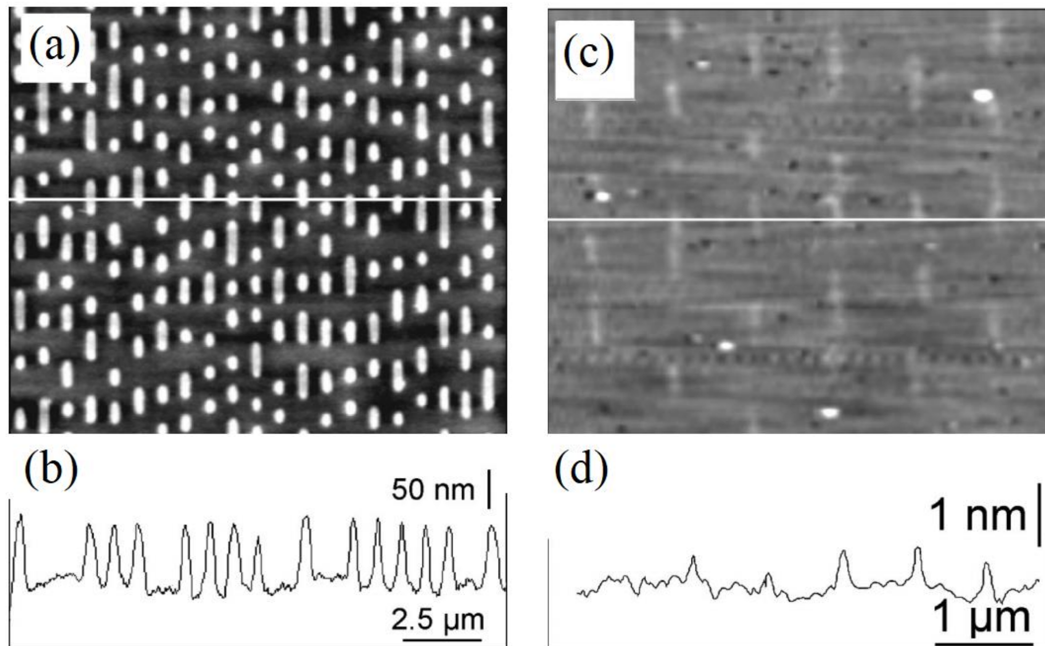

Figure 6.11 [5] (a) AFM topography images of the DVD stamp. (b) Cross-section of DVD stamp in the region marked by the line drawn in figure (a). (c) AFM topography images of the sample after the oxidation process. (d) Cross-section of the sample in the region marked by the line drawn in figure (c).

6.5 Nano-patterning with brass stamp

6.5.1 Preparation of the sample

The first experiment was performed with the brass stamp on a silicon (100) substrate. From Figure 6.12 it is observed that no significant oxidation occurred because of the non-uniform contact due to the high surface deviations and the burrs, as explained in section 6.3.2. Reactive ion etching (RIE) process also confirmed the same (Figure 6.12b). A brush layer can be effective in improving homogeneous contact between the surfaces of the stamp and the sample. By introducing a thin layer of polymer between the surfaces of the stamp and the sample, the oxidation process is

improved as this polymer film is deformed under the force exerted by the stamp, adapting the separation surface to obtain a homogeneous pressure over the whole surface. The hydroxyl-terminated polystyrene (PS–OH) is a suitable polymer as a brush layer in this regard. These polymers are used to create chemical patterns that guide the self-assembly of block co-polymers [263].

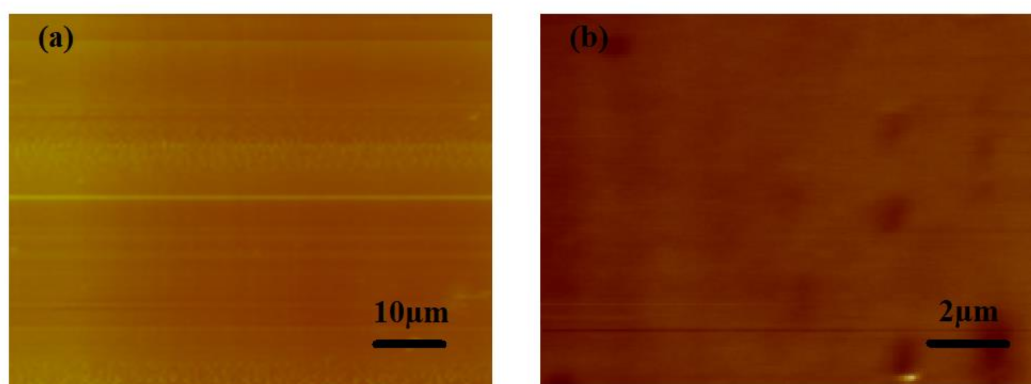

Figure 6.12 AFM topography images of the silicon surfaces. (a) After oxidation process. (b) After RIE etching process.

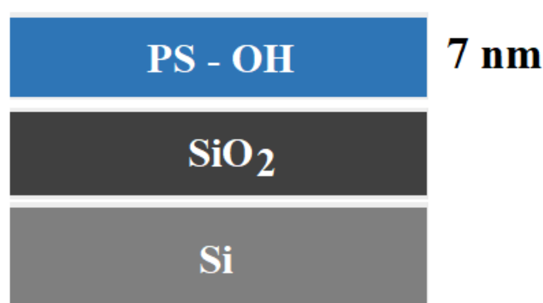

Figure 6.13 Schematic of the Si substrate with PS-OH brush layer.

To prepare the sample, a thin film of hydroxyl-terminated polystyrene (PS–OH) of 4.5 kg/mol (Mn) molecular weight and polydispersity index of 1.09 was deposited by spin-coating and annealed on a p-type Si (100) substrate with a native oxide layer. Two different annealing conditions were used: (i) 260 °C in nitrogen

atmosphere for 5 min and cooling in air and (ii) 230 °C in nitrogen atmosphere for 5 min and cooling in nitrogen. The resistivity of the Si substrate was 4 –40 Ω-cm. The structure of the sample is shown in Figure 6.13.

6.5.2 Oxidation process and results

A bias voltage of 65 V DC has been applied between the stamp and the substrate for 5 minutes under a relative humidity of 80%. After the oxidation process, an RIE etching was performed in a commercial system (Oxford 80 plus RIE) at Instituto de Ciencia de Materiales de Madrid, CSIC, Spain. An SF_6 10 sccm and O_2 (5 sccm) plasma of 15 W and 6.25×10^{-2} m Torr pressure etched 12 nm of silicon in 32 seconds. Figure 6.14 (a – b) shows the optical images of the silicon motifs at different areas of the substrate after the RIE etch. It can be seen that the motifs have been transferred to the surface of silicon with some irregularities and inhomogeneities in their shapes such as broken lines (line interception), nano bridges between lines and double lines. When comparing the images of the brass stamp (Figure 6.8), it is observed that the transferred patterns are similar, and the irregularities are due to the presence of the burrs on the stamp.

Again, some areas of silicon substrate could not be oxidized (Figure 6.15), this is happened due to the existence of some burrs with considerable height variation on the stamp, which makes the misalignment between both surfaces of the stamp and the sample within these areas during the oxidation process. Figure 6.14(d) shows the profile of the section marked in Figure 6.14(c). It is observed that the height of these silicon motifs is about 12 nm with a full width at half maximum of 700 nm and 2 μm apart. In this case, the aspect ratio of the motifs is achieved as 0.017.

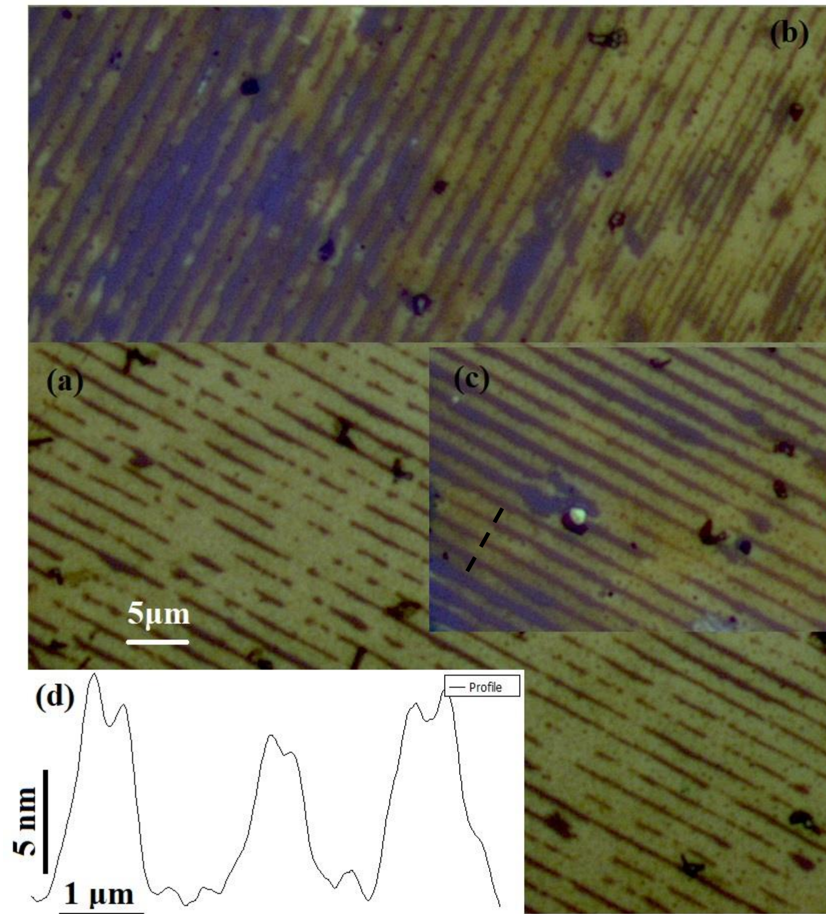

Figure 6.14 (a)-(c) Optical image of the motifs at different areas of the substrate after the RIE etch process. (d) Profile of the silicon lines manufactured.

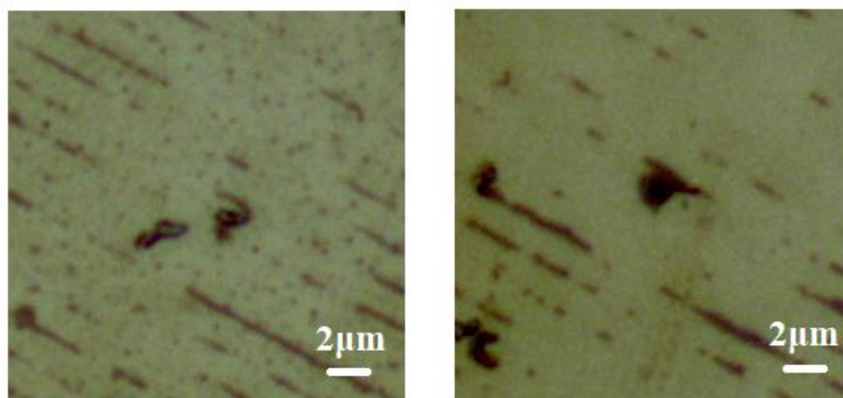

Figure 6.15 Unoxidized areas on the substrate due to burrs.

6.6 Advantage and disadvantage of brass stamps in the NEL process

The stamp with the low elastic modulus (for example, PDMS of ~2 MPa) makes the stamp susceptible to deform, buckle, or motif collapse [264]. Therefore, patterns with smaller features require more rigid mechanical properties of the stamp. Brass stamp with the high elastic modulus (~100 GPa) is advantageous in this regard. However, high reproducibility can be achieved with the brass stamp because of its breaking strength. No significant degradation in the stamp surface has been observed after more than 15 operations (shown in Figure 6.16). This property is beneficial in manufacturing industries as it increases the lifetime of the stamp. Another advantage of the brass stamp is the ability to achieve patterns with a high aspect ratio that is desired in nanolithography applications.

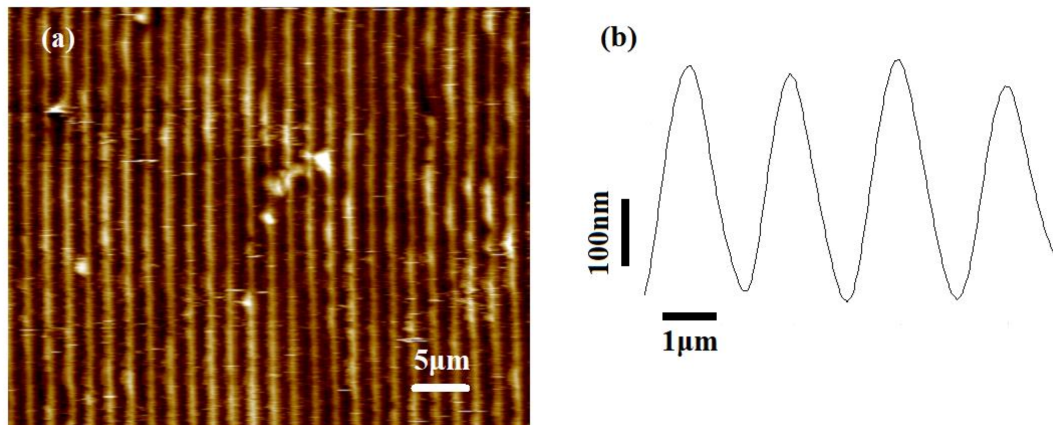

Figure 6.16 (a) AFM images of the brass stamp after 15 operations. (b) Profile of the motifs.

On the other hand, the most significant problem in the brass stamp is the burrs formation during the SPDT process, which causes pattern irregularity and unoxidized area. The deburring techniques can be used to improve the surface quality, but these

techniques are too specific, complicated, and high cost [265]. Alternative solutions would be to use other machining/lithography processes for the stamp fabrication that are capable to limit the burrs formation (for example, EBL, FIB).

6.7 Summary

In this chapter, a prototype NEL system has been developed that allows the control of both the pressure exerted on the stamp and the lateral positioning of the stamp on the sample. To check the performance of this prototype, oxidation was performed on a silicon (100) substrate by using a polycarbonate stamp. The AFM images reveal that the NEL process carried out with the developed system replicates the patterns maintaining the same periodicity (780 nm).

The fabrication of patterns on the brass surface was achieved with the SPDT machine. Some burrs formation occurred during the machining process, which can be reduced by using deburring techniques or other fabrication techniques. The burrs make the brass stamp difficult to achieve the pattern replication as they make an inhomogeneous contact between the stamp and the substrate. A thin polymer film (PS-OH) of approximately 7 nm has been introduced on top of the silicon surface to improve the homogeneous contact. Then NEL oxidation results show that pattern transfer can be achieved with some irregularities. Besides, the brass stamps show no degradation after many uses, which makes them advantageous to use in the NEL process. Therefore, the issues of the burr formation, higher surface deviations, and non-uniformity must be resolved in making these stamps applicable to the NEL process.

Chapter 7 Rolling Nanoelectrode Lithography

7.1 Introduction

Nanofabrication over large areas paves the way for the commercial applications of nanotechnology. Large-area nanofabrications are now being used to manufacture many devices and create innovative products for nanoelectronics, optoelectronics, nanophotonics, and other areas. However, the NEL process with a flat stamp is not suitable for large area nanopatterning as the non-uniformity becomes an issue when they use large stamps. Firstly, it is difficult to achieve a uniform contact between the stamp and the substrate in large-scale due to disuse of the resist materials. Again, another critical challenge in the NEL process is to maintain a uniform pressure over the whole contact area during oxidation. These challenges severely limit NEL to be applied for large-area nanopatterning.

In this chapter, a rolling NEL (R-NEL) process is proposed, which could significantly improve the pattern uniformity. This method can be advantageous as it enables continuous patterning and easy de-molding in large-area fabrication. Firstly, the design concepts in roller-based system are introduced. Then a prototype of the proposed R-NEL system is implemented, and the oxidation process on Si (100) substrate is performed. Finally, the influence of the experimental parameters, such as pattern direction, applied voltage, and rolling speed on the R-NEL process is also investigated.

7.2 Description of the rolling NEL system

The roller-based nanopatterning concepts are not new, which have been successfully utilized in thermal/UV nanoimprint lithography techniques for large-area

nanofabrication, as described in chapter 2. These roller-based manufacturing methods have been recognized to be a high-throughput and low-cost technology. These methods can even fabricate continuous nanopatterns, which make them attractive for various industrial applications [76, 266]. However, application of roller on NEL is rare due to the challenges in fabricating the conductive roller stamps. In the R-NEL system, the roller stamp rolls over the sample while applying the voltage between the stamp and the sample, which eventually produces continuous oxide patterns (Figure 7.1). The introduction of the roller is required to maintain uniform pressure over the whole area. Consequently, the local oxidation process can occur uniformly over a large area of the samples.

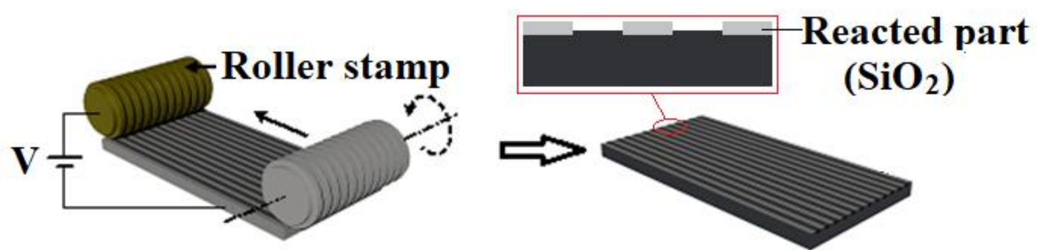

Figure 7.1 Schematic of the proposed rolling NEL system.

In order to develop the prototype system, an air bushing with the roller stamp is mounted on the Z axis of a three-axis translational motion control system. The air bushing distributes air through a tubular media containing millions of sub-micron holes, which holds the roller and enables it to rotate frictionlessly. The sample is placed on a base that can move along X and Y axes. The motions of these three axes are controlled by a computer, which allows the correct positioning of the sample relative to the roller stamp. The roller goes down to make gentle contact with the sample. When the sample moves along the X axis, the roller also rotates due to adhesive force at the

contact between them. Thus, the roller rolls over the sample and fabricates the whole sample surface. Figure 7.2 shows the design concept of a prototype of the rolling NEL system.

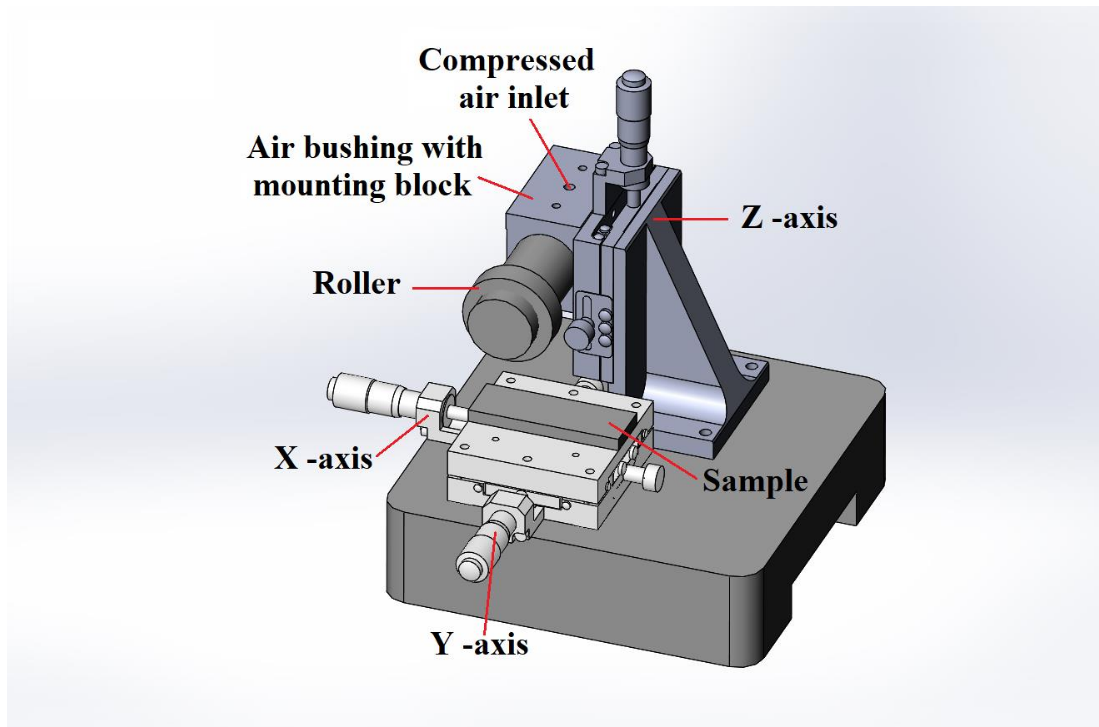

Figure 7.2 Design concept of a prototype of the rolling NEL system.

Obtaining precise contact area between the stamp and the sample is crucial to determine the rolling speed needed for the oxidation process. The actual contact area during oxidation is only a line or a finite rectangular area along the roller in contact with the sample. The size of the contact area, which can be determined by Hertz theory [267], depends upon some parameters such as the applied force, roller dimensions, and the properties of the roller and the sample. By using the Hertz theory, the half-width (b) of the rectangular contact area of two parallel cylinders can be written as [268]:

$$b = \sqrt{\frac{4F\left[\frac{1-v_1^2}{E_{m1}} + \frac{1-v_2^2}{E_{m2}}\right]}{\pi L\left(\frac{1}{R_1} + \frac{1}{R_2}\right)}} \tag{7-1}$$

where E_{m1} and E_{m2} are the elastic moduli for cylinders 1, and 2 and v_1 and v_2 are the Poisson's ratios, and R_1 and R_2 are the radii, respectively. L and F refer to the length of the contact area and the applied force, respectively.

As the sample has a plane surface, then its radius becomes infinite. Considering the flat surface of the sample, the equation reduces to:

$$b = \sqrt{\frac{4FR_1\left[\frac{1-v_1^2}{E_{m1}} + \frac{1-v_2^2}{E_{m2}}\right]}{\pi L}} \tag{7-2}$$

As the throughput of the system depends on the effective contact area, it should be made large. One way to increase the contact area by using the flexible roller stamp, which also ensures the conformal contact during the oxidation process. When a force is applied, the contact area spreads in size. In the case of a flexible roller stamp, the contact area can also be calculated on a purely geometrical basis (shown in Figure 7.3) after carefully measuring the reduced radius of the stamp. Applying Pythagoreans theorem, the half-width b of the rectangular contact area is found as follow:

$$b = \sqrt{R_1^2 - (R_1 - z)^2} \tag{7-3}$$

where z is the portion reduced in stamp diameter.

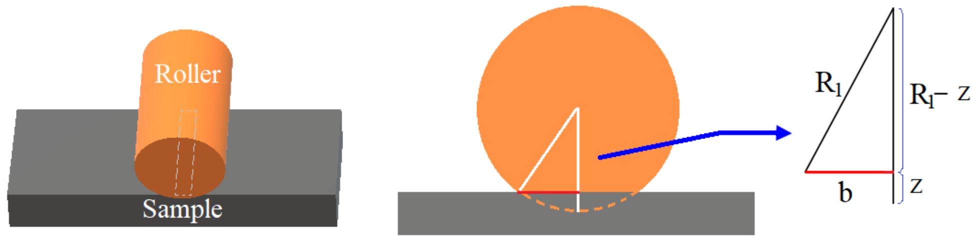

Figure 7.3 Contact area calculation with deformed/elastic roller.

The rolling speed can be calculated by using the following formula:

$$Rolling\ speed = \frac{2b}{t} \tag{7-4}$$

where t is the time required for the oxidation process. The maximum limit for the rolling speed can be obtained by considering the minimum required time for the oxidation process.

7.3 Fabrication of the roller stamp

The roller fabrication for the R-NEL process can be obtained by several methods. One method is to create structures/patterns directly on the roller surface by machining or lithographic processes such as beam writing, mask exposure, and self-assembly techniques. However, the patterning on a circular surface is generally tricky and more complex. Some machining processes also limit the feature size (for example, SPDT). Another way is to wrap a belt or flexible flat stamp around a bare roller. This method is generally the easiest as the belt, or the flexible flat stamp can easily be fabricated with various patterning techniques.

However, wrapping a belt on a roller may leave a seam, which produces an inevitable stamp joint error and degrades the replication accuracy. In this research, the latter was chosen as it is typically more practical and cost-effective for research

purposes. It is also worth noting that a seamless roller stamp should not yield any substantial technical differences, so long as the experimental parameters are the same.

In order to prepare the stamp, a cylindrical roller base has been machined from brass materials on an ultra-precision diamond turning machine. The length and diameter of the roller were selected as 100 mm and 13 mm, respectively. Then the roller base has been first wrapped with a 2 mm thick and 10 mm wide layer of synthetic rubber (polyisobutylene and 2 mol% isoprene), which increases the elasticity of the stamp as well as the contact area. After that, a polycarbonate strip (100 μm thick) was peeled off from a DVD-R and cleaned with an ethanol solution. The strip has adhered to the rubber surface. The overall diameter and the width for the nanostructured area of the roller become 17.2 mm and 10 mm, respectively. Figure 7.4 shows the process steps for roller preparation. The AFM image of the nanostructures shows no degradation after peeled off from the DVD and adhered to the roller (Figure 7.5).

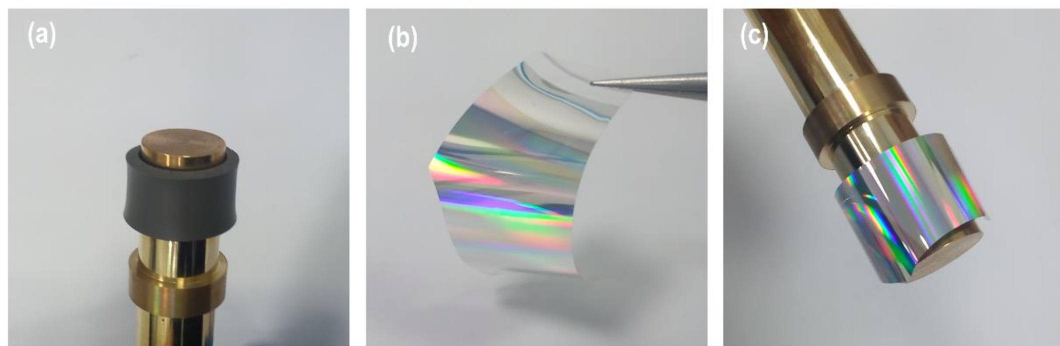

Figure 7.4 (a) Peeled polycarbonate strip. (b) Roller with a rubber band. (c) Completed roller stamp.

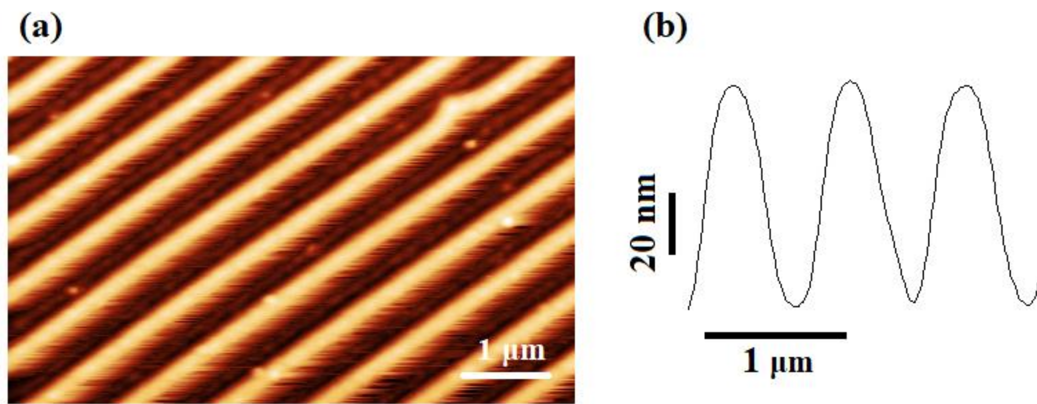

Figure 7.5 (a) AFM topographic image of the roller stamp. (b) Line profile of the AFM image.

7.4 Implementation of the R-NEL system

In order to implement the system, the roller stamp was mounted on the shaft of the previously built NEL system described in chapter 6. The air bushing system of 13.02 mm inner diameter from NEW WAY was used (shown in Figure 7.6), which provides an even distribution of a thin, but a stiff layer of air. The specification of the air bushing can be found in Appendix B. Co-polymer O-rings are utilized to compensate the parallelism errors of up to 50 µm over the length of the roller. While supplying clean, dry compressed air at 60 psi into the mounting block, the roller was inserted into the bushing. A controller is used to maintain a constant airflow at the required pressure (shown in Figure 7.7). A humidifier is used to maintain the relative humidity inside the enclosure. A hygrometer and a weighing scale are also used to measure the relative humidity and the force applied on the roller, respectively. Figure 7.8 shows an overview of the implemented roller based NEL system.

Figure 7.6 Air bushing system.

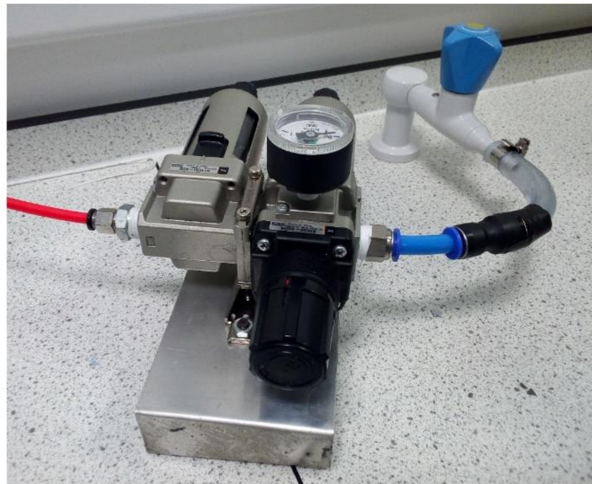

Figure 7.7 Airflow controller.

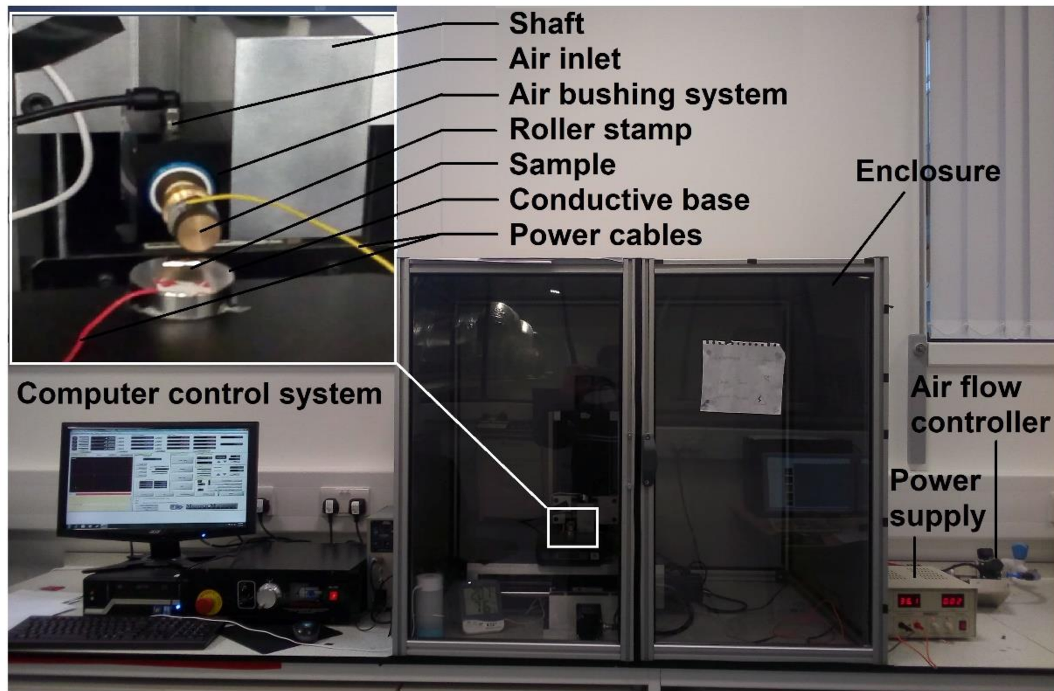

Figure 7.8 Implemented R-NEL system.

7.5 Experimental methods

All the experiments were carried out at room temperature with a relative humidity of 80%. The pressure of the compressed air into the air bushing and the applied force were maintained at 60 psi, and at 1 N, respectively. An atomic force microscope (DI Dimension 3100) was used to inspect the nanostructures on the sample surfaces. To run an experimental operation, the roller is moved towards the sample first by using the jogging of the controller interface (Mach3) until the force reached the desired value. Then a simple program defined by a G Code is run to move the sample in the x-direction at a specific speed. The program statement is in the form:

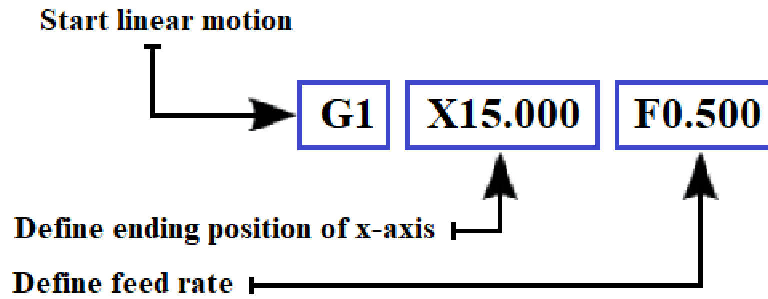

A test run has been performed by using the above-mentioned G code to check the synchronization between the rolling speed and the horizontal displacement of the sample. They showed an excellent synchronization (the sample travels the distance exact equal to the rotational displacement of the roller) even when a little force (0.5 N) was applied on the roller.

7.5.1 Preparation of the samples

In these experiments, samples of p- doped silicon (100) with resistivity ρ = 10-15 Ω-cm were used. As explained in chapter 6, these samples were cleaned with ultrasound in the solution NH_4OH / H_2O_2 / H_2O (1: 1: 5) for 10 minutes. The cleaning process was repeated thrice to achieve the optimal cleaning with a low density of particles on the surface. After cleaning, the samples are blown-dry with an N_2 gas jet.

7.5.2 Contact area calculation

To evaluate the contact area, oxidation was performed with this roller stamp for one minute without any rotation of it. By careful visualization of the oxide area with the AFM, the value appeared to be ~1.1 mm, which is very close to the calculative value of 1.15 mm (the parameters used in calculation are tabulated in Table 7.1). Hence, a rolling speed of 0.50 mm/minute ensures the exposure time to be ~ 2 minutes.

Table 7.1 Parameters for contact-area calculation.

Parameters	Value
Poisson’s ratio of Si (100)	0.28
Poisson’s ratio of synthetic rubber	0.48
Elastic modulus of Si (100)	160 GPa
Elastic modulus of synthetic rubber	2.5 MPa
Length of contact area	10 mm
Radius of the roller stamp	8.6 mm
Applied force	1 N

7.6 Results and discussion

7.6.1 Nanofabrication with R-NEL

The first experiment was carried out by using the roller stamp, where the polycarbonate strip was adhered to the roller base by a double-sided adhesive tape. Figure 7.9 shows the result of the oxidation after applying a voltage of 36 V at a rolling speed of 0.50 mm/minute. It is clearly observed that there is a distorted oxide pattern with some area remained unoxidized. By careful investigation, it is found that the distortion occurred due to the slippage of the roller onto the substrate. This is because of the improper adhesive used (double-sided adhesive tape) between the polycarbonate strip and the roller base. This inappropriate adhesive also creates misalignment between the roller and the substrate, which prevents some area from being oxidized. Therefore, good adhesion between the polycarbonate strip and the roller base is very important to avoid the slippage and the misalignment.

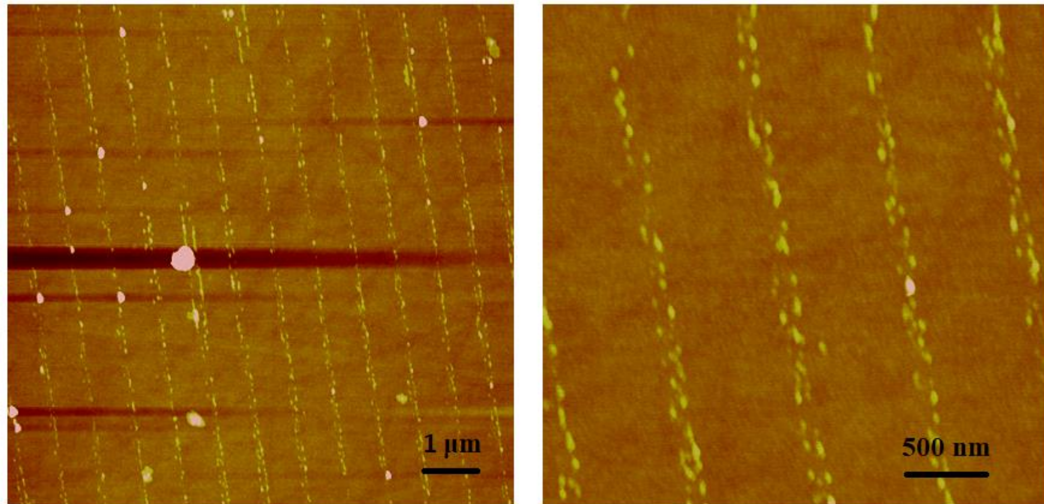

Figure 7.9 AFM topography images of the distorted oxide pattern.

In order to improve the adhesion between the strip and the roller, silver adhesive paint was used. The oxidation experiment was performed with the same experimental parameters, which confirms improved oxidation, as shown in Figure 7.10. A uniform pattern transfer has been achieved with an oxide mean height of 2.1 nm and full width at half maximum (FWHM) of 195 nm on an area of about 8 x 10 mm^2. These results indicate a significant improvement in pattern uniformity compared to the other results obtained with the conventional NEL process [4, 5]. It is also worth mentioning that the seam of the roller used in the experiments restricts the length of the sample area to be patterned. However, this should not make any qualitative technical differences, as mentioned before. Therefore, it is seen that the new rolling NEL process can achieve uniform pattern replication, maintaining the same periodicity.

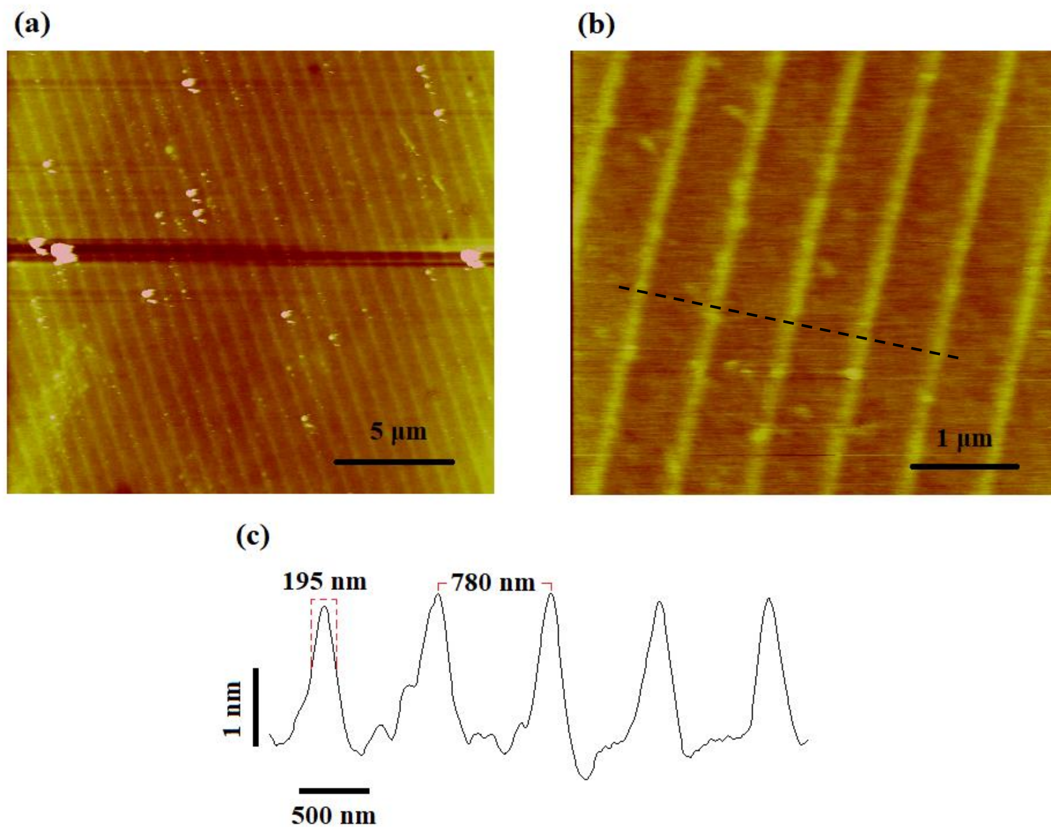

Figure 7.10 (a) AFM topography image of the oxide lines made by R-NEL. (b) Profile of the line marked in the image (a).

7.6.2 Influence of the pattern directions

The oxidation processes performed in the previous section used the roller stamps where the patterns were orthogonal to the moving sample direction (Figure 7.11a). It would be interesting to see how the orientation of patterns affects the oxidation process. To do this, an oxidation experiment was carried out with the same experimental parameters where the patterns are parallel to the moving sample (Figure 7.11b). An oxide pattern of 2 nm height and 190 nm FWHM have been achieved while maintaining the same periodicity (780 nm) (shown in Figure 7.12). These oxide patterns are very similar to the pattern obtained with the roller stamp, where the

patterns were orthogonal to the moving sample direction. Therefore, it can be concluded that there is no significant influence of pattern directions on the oxidation process in the rolling NEL process.

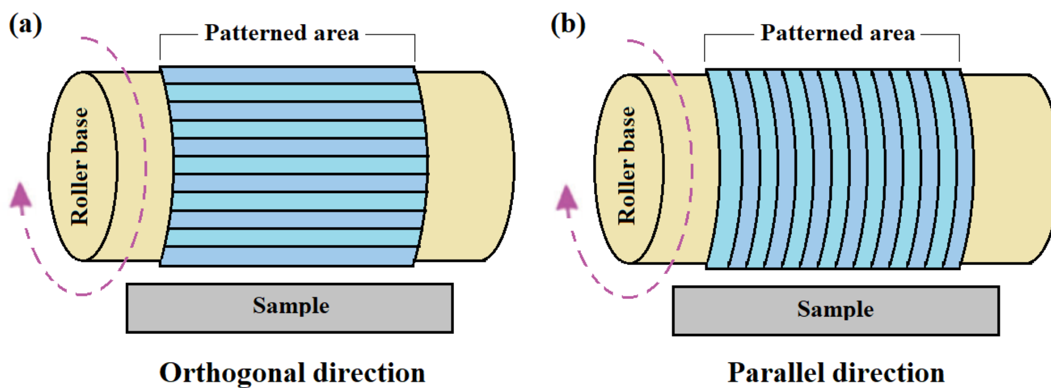

Figure 7.11 Schematic diagram of pattern directions. (a) Orthogonal. (b) Parallel.

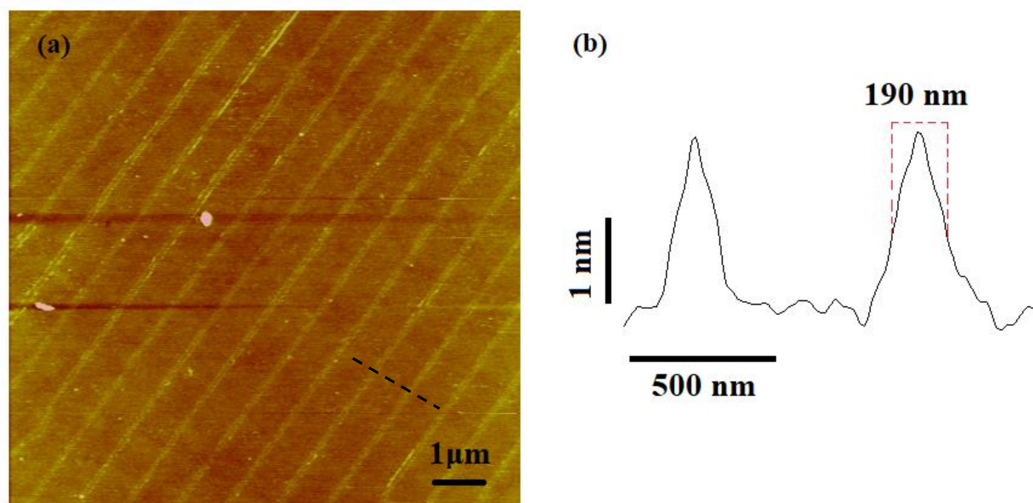

Figure 7.12 Parallel pattern direction. (a) AFM topography image of the oxide lines. (b) Profile of the lines marked in the image (a).

7.6.3 Effect of the rolling speed

The rolling speed and the applied voltage are two major parameters to optimize the rolling NEL approach. Hence, the effect of bias voltage and rolling speed on oxide growth were studied. In this section, the oxidation process was conducted at three rolling speeds of 0.25, 0.50, and 1 mm/minute. Applying the constant voltage (36 V), Figure 7.13 (a-c) shows the topographic images of the substrates for three different rolling speeds. The height and the full width at half maximum (FWHM) of the oxides are represented concerning the rolling speeds where each point of the graph represents an average of few values obtained in the same sample (shown in Figure 7.13d).

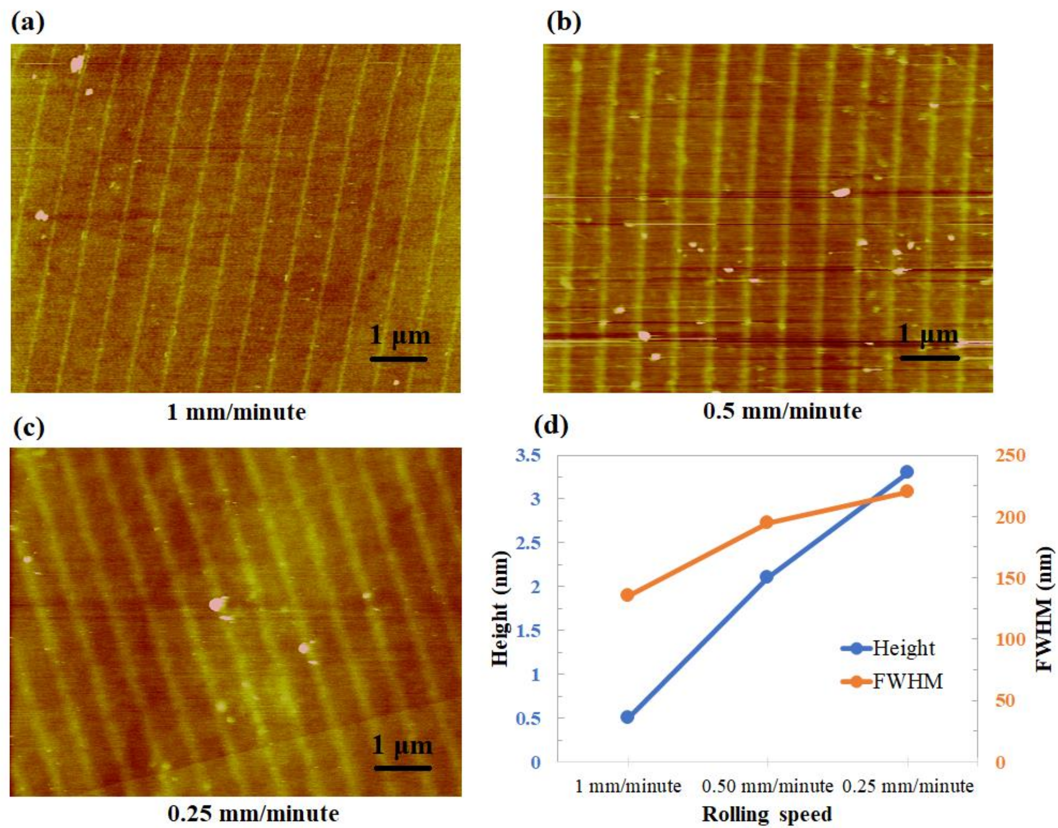

Figure 7.13 (a)-(c) AFM topographic images. (d) Relationship between the rolling speed and oxide height (left side of the graph) and FWHM (right side of the graph).

It is seen that the oxide patterns have a linear increase of height with a decrease in the rolling speed. It can be explained by the fact that as the rolling speed increases, the exposure time for the contact area decreases. The previous study also showed that the height of the oxides increases with the oxidation time [5]. However, D. Stievenard *et al*. presented that the oxide height varies as log(1/speed) with tip writing speed in the AFM oxidation lithography process [252]. In the rolling NEL process, it shows linear dependency on rolling speed rather than logarithmic.

Again, it can be seen from Figure 7.13 (d) that the width (FWHM) increases with decreasing rolling speed. In other words, low rolling speeds made broader oxide patterns. The growth behavior of oxide width with the rolling speed can be explained considering two models proposed for AFM oxidation. Firstly, Kuramochi *et al*. [255] suggested the ionic diffusion as the main reason for the lateral oxide growth at the long exposure time. Ionic diffusion takes place through the adsorbed water layer when the grown oxide starts preventing the current flow under the stamp protrusion (tip).

In another research, Bloeß *et al*. [153] showed that the size of the water bridge limits the lateral oxide growth. Although the size of the water bridge is influenced by the electric field and the relative humidity, the size of the contact area remains the main factor. Therefore, it can be concluded that the oxide width increases with the exposure time due to ionic diffusion until a certain value determined by the size of the water bridge.

7.6.4 Effect of the applied bias voltage

In this case, the oxidation was performed with bias voltage ranging from 26 to 46 V at a rolling speed of 0.50 mm/minute. Figure 7.14 shows that the oxide height

increases linearly with the applied voltage. This outcome also validates the results obtained from MD simulations described in chapter 4.

Also, the aspect ratio (height:width) of the oxide lines is one of the essential factors both in mask fabrication and lithography processes for the semiconductor industry. It is found that the aspect ratio also increases as the rolling speed decreases (from 0.0037 for 1 mm/minute to 0.015 for 0.25 mm/minute). Therefore, the precise control of the aspect ratio of the oxide lines can be achieved by careful optimization of the experimental parameters, such as rolling speed and the applied voltage. Besides, the throughput can easily be increased by using the roller stamp with a higher radius.

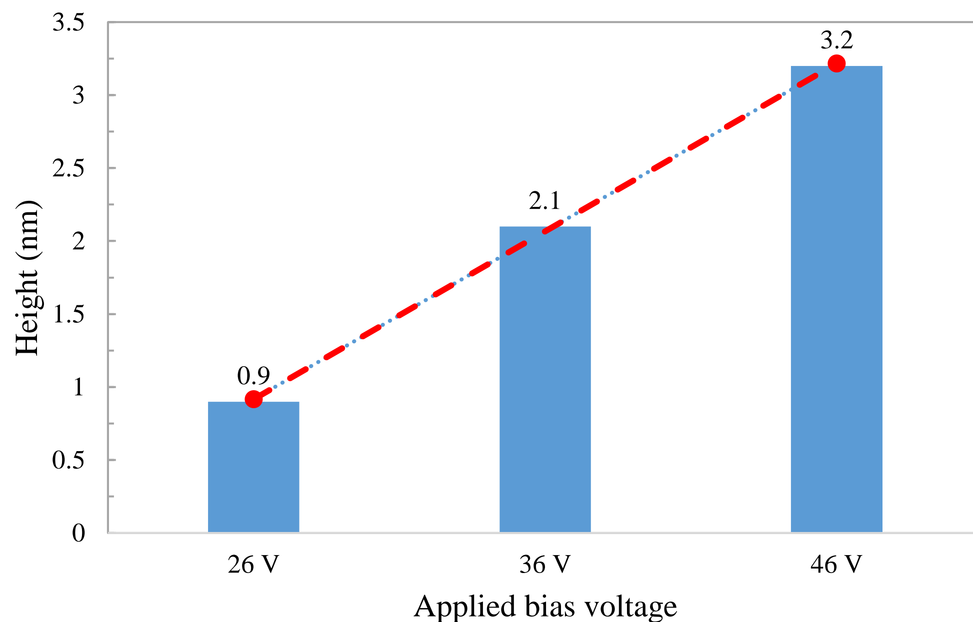

Figure 7.14 Height of oxide lines for different applied bias voltages at a rolling speed of 0.50 mm/minute.

7.7 Summary

A roller based nanoelectrode lithography approach was proposed for the first time in this paper to fabricate nanostructures on silicon substrates. A prototype system

was designed and implemented where a polycarbonate strip wrapped with a brass roller base was used as the stamp. This new system requires a much smaller force since it proceeds in a small area perpendicular to the sample moving direction. A uniform pattern transfer for the large area has been achieved with this new R-NEL system. The rolling speed and the applied bias voltage were identified as the primary control parameters for the oxide growth. Experimental studies show the linear dependence of the oxide height as a function of the applied voltage, whereas the oxide height is inversely proportional to the rolling speed. The effect of the pattern direction was also identified, which show no significant differences. These results show that the new rolling NEL approach allows the control of the parameters involved in the oxidation process, and this could enable the nanoelectrode lithography method in large area fabrication and electronic device mass production.

Chapter 8 Conclusions and Future Works

8.1 Conclusions

This PhD thesis investigated the underlying mechanism of nanoelectrode lithography on the silicon substrates based on simulation and experimental studies. Chapters 3, 4, and 5 of this thesis have been devoted to the molecular dynamics simulation study of the kinetics of the NEL oxidation process and the parametric effects on the process. Chapter 5 also includes an experimental validation of substrate orientational influence on the oxidation process. Chapter 6 has shown the feasibility of brass materials for the nanoelectrode lithography process. Finally, in Chapters 7, a new type of NEL process based on roller stamp was proposed and developed for the large-area nanofabrication applications. The main conclusions from the research can be summarised as follows:

1. The adsorption of the water molecules on the silicon surfaces and their dissociation into OH^- and H_3O^+ are observed at the first stage of the NEL oxidation process. The OH groups are also adsorbed on the Si surfaces and then dissociate by releasing the O atoms to form the Si–O–Si bonds, making the surfaces oxidized. The higher oxidation rate is found at the very beginning, and the rate slows down over the period. The accumulation of the oxygen atoms in the oxide film is found in a layer by layer fashion. The number of the oxygen atoms is observed less in the deeper positions of the oxide film, and the RDF analysis suggests the oxide film as an amorphous structure.

2. There is a linear dependence of the oxide thickness with the intensity of the electric field. The higher electric field can make the surface more oxidized. A similar characteristic is also observed for the higher range of relative humidity. After

a certain value (40%), the oxide thickness varies linearly with the relative humidity. These results are in good agreement with the experimental observations.

3. Molecular adsorption of H_2O contributes more to the interaction process for the substrates (100) and (110), whereas the dissociative adsorption dominates for the substrate (111). The thickness of the oxide film observed in ReaxFF MD simulation exhibits the order T(100) > T(110) > T(111) at lower electric field intensities (3 V/nm and 5 V/nm), which is the same order that the surface energy exhibits, confirming that surfaces with higher surface energy are more reactive at lower electric field intensity.

4. However, a crossover was observed at higher electric field intensity (7 V/nm) for the substrates (100) and (110), which yield the order T(110) > T(100) > T(111). Besides, it was found that there was also a slight crossover in the initial oxygen diffusion rate to R(111) > R(110) at 7 V/nm. The initial order at lower electric field intensities was R(100) > R(110) > R(111). The oxygen diffusion rate and the thickness of the oxide film increase with the increase of the electric field intensities.

5. The AFM oxidation experiment showed the thickness of the oxide films yields the order T(110) > T(111) > T(100), which is different from the simulation results. As the areal density of atoms and the activation energy depend on the substrate orientation, these two parameters could be the main reasons for the variation of the oxide growth. The experimental result also suggested that the variation in the relative humidity does not change the order of the substrate's orientations in terms of the oxide thickness.

6. The NEL process was carried out on a silicon (100) substrate with a polycarbonate stamp on a prototype NEL system, that shows a good pattern replication.

On the other hand, the patterning with the brass stamp showed difficulties in producing homogeneous contact between the stamp and the substrate due to the burrs formed on the brass surface during the SPDT machining process. A thin polymer film (PS-OH) of approximately 7 nm can be introduced on top of the silicon surface to improve the homogeneous contact. Then NEL oxidation results showed that pattern transfer could be achieved with some irregularities. Besides, the brass stamps showed no degradation after many uses, which makes them advantageous to use in the NEL process. Nevertheless, the issues of the burr formation and non-uniformity should be alleviated first to make these stamps appropriate to the NEL process.

7. It is feasible to use the developed rolling nanoelectrode lithography (R-NEL) approach for the large-area nanofabrication. This new system requires a much smaller force since it proceeds in a small area perpendicular to the sample moving direction. A uniform pattern transfer for the large area can be achieved with this new R-NEL system. The rolling speed and the applied bias voltage were identified as the primary control parameters for the oxide growth. Experimental studies showed the linear dependence of the oxide height as a function of the applied voltage, whereas the oxide height is inversely proportional to the rolling speed. The effect of the pattern direction was also identified, which showed no significant differences. These results show that the new roller based NEL system allows the control of the parameters involved in the oxidation process, and this could enable the nanoelectrode lithography process in large area fabrication and electronic device mass production.

8.2 Contributions to knowledge

The contributions to knowledge in this dissertation can be listed as follows:

1. A new MD models which is able to suitably simulate the NEL oxidation process and study the effect of the parameters such as relative humidity, and electric field using a reactive force field (ReaxFF), which can appropriately describe the covalent interactions of silicon and water molecules.

2. The knowledge on how the crystallographic orientation of the silicon substrates influence the oxidation process. MD simulations and experimental study have provided novel insights into the orientation dependent parameters, such as areal density of atoms, surface energy, and the activation energy, which could be the main factors for the variation of the oxide growth.

3. Enhancement of knowledge on the applicability of brass materials as the NEL stamps. These stamps can reduce the process steps and lower the cost.

4. Development of a novel rolling NEL approach and system for large area patterning for the first time. The rolling NEL requires very little force exerted on the stamp. This lithography process offers pattern transfer with high uniformity and high throughput. It also facilitates continuous patterning, which makes it a promising method for large-area nanofabrication applications.

8.3 Recommendations for future works

1. Molecular dynamics simulations were performed in this research for 400 picoseconds only, while experimental investigations show large-scale features. Therefore, further studies are required with a long simulation run time to elucidate some of the many unknowns concerning the origin of the anomalous features.

2. Currently, the NEL process is used to fabricate nanostructures on the semiconductor substrates. This method can be useful to pattern nanostructures on the polymer substrates (for example, PMMA), which are the essential components for optical devices. Therefore, it is worth a try to investigate the applicability of the NEL process in fabricating the polymer substrates. The required electric field and the maximum allowable thickness of the polymer thin film can be the main controlling factors in this regard.
3. The rolling NEL approach was presented for the first time in this thesis. Therefore, the further exploration of this process, such as patterning with the flexible rollers (resin type), influence of the applied force, and 3D feature fabrication is required. Brass materials can be useful to fabricate the roller stamp if only the burr formation is mitigated, as explained in chapter 6. Besides, other stamp materials, such as electroless nickel should be explored. Previous study showed that an array of nano-gratings was successfully obtained on an electroless nickel substrate by using nano-scale single crystal diamond tool with SPDT machine [269]. Their approach can be effective in creating nanostructures on a precision roller for the rolling NEL process. Furthermore, some modifications should be considered to make this technique appropriate for commercial use. Firstly, a rotating system can be implemented by using electrical motors (synchronized motors or stepper motors), which allow the roller to rotate at the desired speed. A control system is needed to synchronize both the rolling speed and the sample speed to avoid the slip between them. In addition, the rolling speed so as the throughput can be increased by using a roller with a large diameter.

4. At present, the NEL approach is used to fabricate nanostructures on flat surfaces. However, next generation electronic devices require flexible memory and logic devices that have curved surfaces. Hence, the further exploration of the rolling NEL on patterning the flexible surfaces (for example, flexible silicon) would be beneficial to the industrial popularisation of this technology.

Appendix A: RH calculations [218]

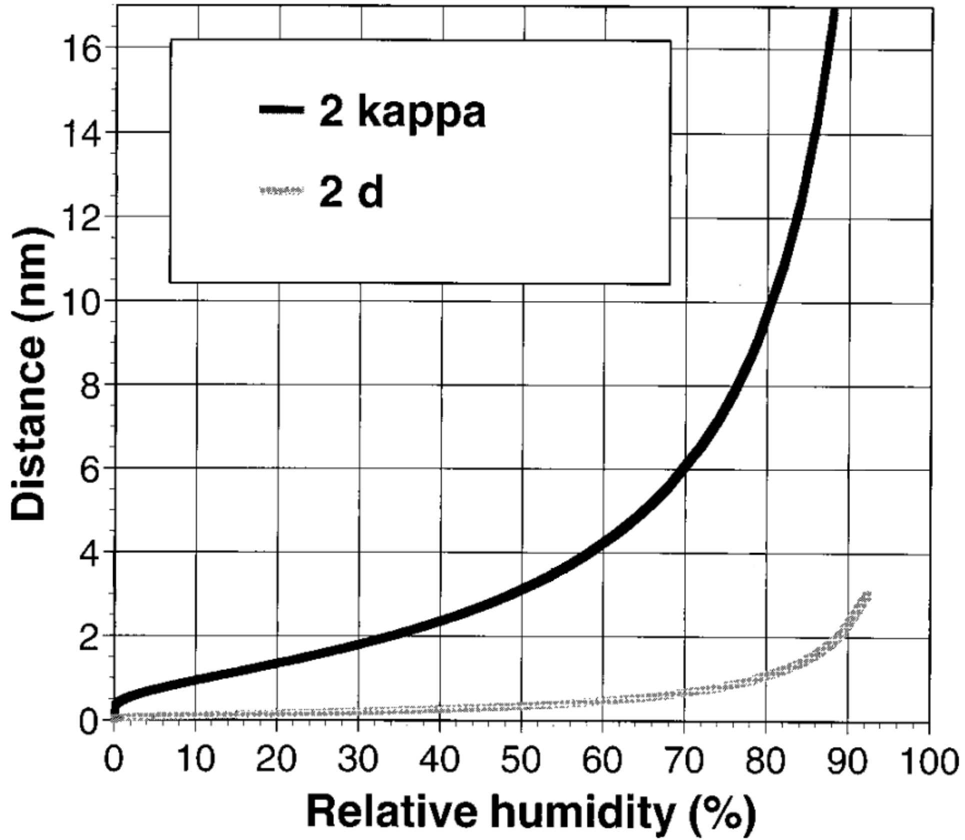

Figure A The curves represent twice the theoretical values of the film thickness, 2d (grey), and the radius of the meniscus, 2k (black) vs the relative humidity.

The values of the film thickness (d) and the radius of the meniscus (k), the so-called Kelvin radius are calculated as follows:

$$d^3 = \frac{A}{6\pi nkT \ln(x)} \tag{A-1}$$

$$k = \frac{\gamma}{nkT \ln(x)} \tag{A-2}$$

where *A* is the Hamaker constant of the stamp–sample system, *n* is the number density of the liquid (molecules per m^3), *kT* is the thermal energy, *x* is the relative humidity, and *γ* is the surface energy of the liquid (γ_{H2O}~72 mJ/m^2).

Appendix B: Specification of Air Bushing

Table B Specification of air bushing [270]

Parameters	Value
Size	13 nm
Input Pressure	60 psi
Radial Load Max	10 lb
Radial Stiffness	0.06 lb/µin
Pitch Moment Max	7.5 lb-in
Pitch Stiffness	19.0 lb-in/mil rad
Flowrate on Shaft	4.75 - 6.60 SCFH
Air Gap at maximum recommended load	150 micro-inches
Bushing Inside Diameter (ID)	13.020 mm +.005/-.000
Bushing Outside Diameter (OD)	0.9 in
Bushing Length	2.0 in
Bushing Weight	1.1 oz
Housing Material/Finish	Aluminum/Anodized
Porous Media Material	Carbon
Recommended Shaft Outside Diameter (OD)	0.5118 in
Recommended Shaft Tolerance	-.0002/-.0007 in (g6)
Recommended Mounting Bore Diameter	0.952 in +.005/-.000
Pressure Port Threads	M3 x 0.5
Viable Pressure Range	60 - 80 psi
Maximum Allowable Pressure Supply	100 psi
Recommended Bushing Rotary Speed	50 m/s
Bushing ID Speed	76,500 rpm
Resolution	Infinite
Maximum Speed	164.04 ft/s

References

[1] International Technology Roadmap for Semiconductors (ITRS) 2015 Edition, 2015.

[2] H. Hiroshima and M. Komuro, “Control of bubble defects in UV nanoimprint,” *Jpn. J. Appl. Phys*., 46(9B), 6391–6394, 2007.

[3] X. Liang, H. Tan, Z. Fu and S. Y. Chou, “Air bubble formation and dissolution in dispensing nanoimprint lithography,” *Nanotechnology*, 18, 025303, 2007.

[4] A. Yokoo, “Nanoelectrode lithography,” *Japanese Journal of Applied Physics*, Part 2: Letters, 42, L92–L94, 2003.

[5] M. Cavallini, P. Mei, F. Biscarini and R. García, “Parallel writing by local oxidation nanolithography with submicrometer resolution,” *Applied Physics Letters*, 83, 5286–5288, 2003.

[6] Y. F. Li, K. H. Chen, Y. Ootera, H. Toshiyoshi and H. Fujita, “Nanoelectrode lithography using flexible conductive molds,” *Applied Physics A: Materials Science and Processing,* 121, 363–370, 2015.

[7] C. Albonetti et al., “Parallel-local anodic oxidation of silicon surfaces by soft stamps,” *Nanotechnology*, 19, 435303, 2008.

[8] N. S. Losilla, J. Martínez and R. García, “Large area nanoscale patterning of silicon surfaces by parallel local oxidation,” *Nanotechnology*, 20, 475304, 2009.

[9] A. Yokoo and S. Sasaki, “Oxidation patterning of GaAs by nanoelectrode lithography,” *Japanese Journal of Applied Physics, Part 1: Regular Papers and Short Notes and Review Papers,* 44, 1119–1122, 2005.

[10] Y. Okada, Y. Iuchi, M. Kawabe and J. S. Harris, “Basic properties of GaAs oxide generated by scanning probe microscope tip-induced nano-oxidation process,” *Journal of Applied Physics,* 88, 1136–1140, 2000.

[11] N. S. Losilla, J. Martinez, E. Bystrenova, P. Greco, F. Biscarini and R. García, "Patterning pentacene surfaces by local oxidation nanolithography," *Ultramicroscopy,* 110, 729–732, 2010.

[12] J. Mulkens et al., "Overlay and edge placement control strategies for the 7-nm node using EUV and ArF lithography," *in Proc. SPIE 9422*, 94221Q, 2015.

[13] D. Z. Pan, L. Liebmann, B. Yu, X. Xu and Y. Lin, "Pushing multiple patterning in sub-10 nm: are we ready?," in *Proc. of the 52nd annual design automation conference,* p. 1-6, 2015.

[14] B. Turkot, S. L. Carson, A. Lio et al., "EUV progress toward HVM readiness," in *Proc. SPIE 9776*, 977602, 2016.

[15] C. Wagner and N. Harned, "EUV lithography: Lithography gets extreme," *Nature Photonics,* 4, 24-26, 2010.

[16] A. Pirati, R. Peeters, D. Smith et al., "EUV lithography performance for manufacturing: status and outlook," in *Proc. SPIE 9776*, 97760A, 2016.

[17] M. Hori, T. Naruoka, H. Nakagawa et al., "Novel EUV resist development for sub-14 nm half pitch," in *Proc. SPIE 9422*, 94220P, 2015.

[18] N. Fu, Y. Liu, X. Ma and Z. Chen, "EUV Lithography: State-of-the-Art Review," *J. Microelectron. Manuf.*, 2, 2019.

[19] M. Mastenbroek, "Progress on 0.33 NA EUV systems for High-Volume Manufacturing," in *Proc. SPIE 11147, International Conference on Extreme Ultraviolet Lithography*, 1114703, 2019.

[20] M. C. Phillips, "EUV Extendibility at 0.33 and 0.55NA" in *Proc. SPIE 11147, International Conference on Extreme Ultraviolet Lithography*, 1114702, 2019.

[21] E. R. Hosler and R. Obert, "Free-electron Lasers: Beyond EUV Lithography Insertion," *Wood II*, p. 16.

[22] A. Pirati, J. V. Schoot, K. Troost et al., "The future of EUV lithography: enabling Moore's Law in the next decade," in *Proc. SPIE 10143*, 101430G, 2017.

[23] I. Fomenkov, "EUV Source for High Volume Manufacturing: Performance at 250 W and Key Technologies for Power Scaling," *Source Workshop*, Dublin, Ireland, 2017.

[24] Yuta Takashima et al., "Update of the development progress of the high power LPP-EUV light source using a magnetic field," in *Proc. SPIE 11147, International Conference on Extreme Ultraviolet Lithography*, 111471M, 2019.

[25] E. R. Hosler, O. R. Wood, W. A. Barletta, P. J. S. Mangat, and M. E. Preil, "Considerations for a free-electron laser-based extreme-ultraviolet lithography program," in *Proc. SPIE 9422*, 94220D, 2015.

[26] T. Sizyuk and A. Hassanein, "Revisiting Li as potential EUV source using dual-laser beam systems," *in Proc. SPIE*, 9776-25, 2016.

[27] A. Hassanein and T. Sizyuk, "Pulse widths optimization of dual-beam laser systems for high-power EUV sources," in *Proc. SPIE*, 9776-26, 2016.

[28] E. Buitrago, T. S. Kulmalax, R. Fallica and Y. Ekinci, "EUV lithography process challenges," *Frontiers of Nanoscience*, Vol. 11, J. Hayton, Elsevier, p. 150, 2016.

[29] Y. Vesters, D. D. Simone and S. De Gendt, "Influence of post exposure bake time on EUV photoresist RLS trade-off," in *Proc. SPIE 10143*, 1014324, 2017.

[30] A. Shirotori et al., "Development of main chain scission type photoresists for EUV lithography," in *Proc. SPIE 11147, International Conference on Extreme Ultraviolet Lithography*, 111470J, 2019.

[31] Vesters Y. at el., "Multi-trigger resist patterning with ASML NXE3300 EUV scanner," in *Proc. SPIE*, 10586, 2018.

[32] G. O'Callaghan et al., "Initial results with the high opacity multi-trigger resist," in *Proc. SPIE 11147, International Conference on Extreme Ultraviolet Lithography*, 111470K, 2019.

[33] T. Fujimori, T. Tsuchihashi and S. Minegishi, "Novel ultra-high sensitive 'metal resist' for EUV lithography," in *Proc. SPIE*, 9776-4, 2016.

[34] D. D. Simone, S. Sayan, S. Dei et al., "Novel metal containing resists for EUV lithography extendibility," in *Proc. SPIE*, 9776-5, 2016.

[35] H. Tsubaki, W. Nihashi, T. Tsuchihashi et al., "Negative-tone imaging with EUV exposure toward 13nm hp," in *Proc. SPIE*, 9776-8, 2016.

[36] S. Tagawa, A. Oshima, C. Q. Dinh et al., "The reaction mechanism and patterning of photosensitized chemically amplified resists," in *Proc. SPIE*, 9776-38, 2016.

[37] K. Kasahara, V. Kosma, J. Odent et al., "Recent progress in nanoparticle photoresists development for EUV lithography," in *Proc. SPIE*, 9776-3, 2016.

[38] K. Kasahara, H. Xu, V. Kosma et al., "Nanoparticle photoresist studies for EUV lithography," in *Proc. SPIE,* 10143, 2017.

[39] D. D. Simone, Y. Vesters, A. Shehzad et al., "Exploring the readiness of EUV photo materials for patterning advanced technology nodes," in *Proc. SPIE 10143*, 101430R, 2017.

[40] H. B. Cao, P. F. Nealey and W. D. Domke, "Comparison of resist collapse properties for deep ultraviolet and 193 nm resist platforms," *Journal of Vacuum Science & Technology B*,18:3303-7, 2000.

[41] B. Y. Zong, P. Ho, G. C. Han et al., "A simple approach to sub-100 nm resist nanopatterns with a high aspect ratio," *Journal of Micromechanics and Microengineering,* 23(3), 035038, 2013.

[42] W. Shibayama, S. Shigaki, M. Nakajima et al., "Dry development rinse process (DDRP) & materials (DDRM) for EUVL." *Journal of photopolymer Scienece and Technology*, 29(3), 469-474, 2016.

[43] V. Sidorkin, S. Zimmermann, S. Proske, M. Finken, G. R. Cantrell and M. Bender, "Towards ultimate image placement accuracy for EUV mask writing with pattern shift process," in *Proc. SPIE 10957, Extreme Ultraviolet (EUV) Lithography X,* 109570K, 2019.

[44] V. Philipsen, K. V. Luong, L. Souriau et al., "Reducing EUV mask 3D effects by alternative metal absorbers," in *Proc. SPIE 10143*, 1014310, 2017.

[45] D. Hellweg, M. Koch, S. Perlitz et al., "Actinic review of EUV masks: performance data and status of the AIMS EUV system," *in Proc. SPIE*, 10143, 2017.

[46] I. Mochi, P. Helfenstein, I. Mohacsi et al., "RESCAN: an actinic lensless microscope for defect inspection of EUV reticles," in *Proc. SPIE*, 10143, 2017.

[47] H. Feldmann, O. Conradi, P. Graeupner, J. Schoot, P. Kuerz, and W. Kaiser "Advancing EUV lithography optics," in *Proc. SPIE 11147, International Conference on Extreme Ultraviolet Lithography*, 1114704, 2019.

[48] S. J. Lin et al., "Multiple electron-beam direct-write lithography: an overview," in *Proc. SPIE*, 9777-3, 2016.

[49] G. de Boer et al., "MAPPER: Progress towards a highvolume manufacturing system," in *Proc. SPIE,* 8680, 2013.

[50] E. Platzgummer, E. Klein, and H. Loeschner, "Electron multi-beam technology for mask and wafer writing at 0.1 nm address grid," in *Proc. SPIE 8680*, 868001, 2013.

[51] D. Lam, D. Liu, and T. Prescop, "E-beam direct write (EBDW) as complementary lithography,"in *Proc. SPIE 7823*, 78231C, 2010.

[52] B. J. Kampherbeek, "Applications for Mapper technology," *Semicon Europa*, Munich, 2017.

[53] M. Wieland et al., "Performance validation of Mapper's FLX-1200," in *Proc. SPIE 10958, Novel Patterning Technologies for Semiconductors, MEMS/NEMS, and MOEMS*, 109580I, 2019.

[54] EBPG5200, https://www.raith.com/products/ebpg5200.html, (accessed April 2020).

[55] H. Matsumoto, H. Kimura, T. Tamura, and K. Ohtoshi, "Multi-beam mask writer MBM-1000," in *Proc. SPIE 10958, Novel Patterning Technologies for Semiconductors, MEMS/NEMS, and MOEMS*, 109580J, 2019.

[56] A. E. Grigorescu and C. W. Hagen, "Resists for sub-20-nm electron beam lithography with a focus on HSQ: state of the art," *Nanotechnology*, 20(29), 2009.

[57] J. K. W. Yang, B. Cord, H. Duan et al., “Understanding of hydrogen silsesquioxane electron resist for sub-5-nm-half-pitch lithography,” *Journal of vacuum science & technology. B*, 26(6), 2622-2627, 2009.

[58] M. Altissimo, “E-beam lithography for micro-nanofabrication,” *Biomicrofluidics*, 4, 36, 2010.

[59] V. R. Manfrinato, L. Zhang, D. Su et al., “Resolution limits of electron-beam lithography towards the atomic scale,” *Nano Letters*, 13(4), 2013.

[60] B. Lee, J. Hong, N. Amos et al., “Sub-10-nm-resolution electron-beam lithography toward very-high-density multilevel 3D nano-magnetic information devices,” *J. Nanopart. Res.,* 15:1665, 2013.

[61] J. Nabity. (2017). Nanometer Pattern Generation System. JC Nabity Lithography Systems. USA. [Online]. Available: http://www.jcnabity.com.

[62] S. W. Youn, M. Ogiwara, H. Goto, M. Takahashi and R. Maeda, “Prototype development of a roller imprint system and its application to large area polymer replication for a microstructured optical device,” *Journal of Materials Processing Technology*, 202, 76–85, 2008.

[63] T. Kono et al., “Improvement of nano-imprint lithography performance for device fabrication,” in *Proc. Novel Patterning Technologies 10584*, 105840V, 2018.

[64] T. Nakayama, M. Yonekawa, Y. Matsuoka et al., “Improved defectivity and particle control for nanoimprint lithography highvolume semiconductor manufacturing,” In *Proc SPIE 10144*, 1014407, 2017.

[65] T. Arai, Y. Matsuoka and H. Azuma, “Improved particle control for high volume semiconductor manufacturing for nanoimprint lithography,” in *Proc. SPIE, XXV Symposium on Photomask and Next-Generation Lithography Mask Technology*, 10807, 2018.

[66] T. Kono et al., “Half-pitch 14nm direct patterning with nanoimprint lithography,” in *Proc. SPIE 10958, Novel Patterning Technologies for Semiconductors, MEMS/NEMS, and MOEMS*, 109580H, 2019.

[67] S.V. Sreenivasan, “Nanoimprint lithography steppers for volume fabrication of leading-edge semiconductor integrated circuits,” *Microsystems & Nanoengineering*, 3, 17075, 2017.

[68] T. Hayashi et al., “Status of overlay performance for NIL high volume manufacturing,” in *Proc. SPIE, XXVI Symposium on Photomask and Next-Generation Lithography Mask Technology*, 11178, 2018.

[69] Z. Hamaya et al., “High volume semiconductor manufacturing using nanoimprint lithography,” in *Proc. SPIE*, 10810, 2018.

[70] J. M. Keith, N. Gregory, B. Shufeng and Y. C. Stephen, “Wafer-scale patterning of sub-40 nm diameter and high aspect ratio (more than 50:1) silicon pillar arrays by nanoimprint and etching,” *Nanotechnology*, 34, 345301, 2008.

[71] B. Cui, L. Clime, K. Li and T. Veres, “Fabrication of large area nanoprism arrays and their application for surface enhanced raman spectroscopy,” *Nanotechnology*, 14, 145302, 2008.

[72] J. Lee, S. Park, K. Choi and G. Kim, “Nano-scale patterning using the roll typed UV-nanoimprint lithography tool,” *Microelectronic Engineering*, 85, 861–865, 2008.

[73] J. John, Y. Tang, J. Rothstein et al., “Large-area, continuous roll-to-roll nanoimprinting with PFPE composite molds,” Nanotechnology, 24, 505307, 2013.

[74] J. Taniguchi, H. Yoshikawa, G. Tazaki and T. Zento “High-density pattern transfer via roll-to-roll ultraviolet nanoimprint lithography using replica mold,” *Journal of Vacuum Science & Technology B 30*, 06FB07,1-5, 2012.

[75] J. J. Dumond and H. Y. Low, “Recent developments and design challenges in continuous roller micro- and nanoimprinting,” *Journal of Vacuum Science & Technology B 30.1*, 010801,1-28, 2012.

[76] N. Kooy, K. Mohamed, L. T. Pin and O.S. Guan, “A review of roll-to-roll nanoimprint lithography,” *Nanoscale Research Letters*, 9:320, 1-13, 2014.

[77] H. Teyssedre et al., “200mm wafer scale NIL process assessment for sub-micrometer CD uniformity with the SmartNIL process,” in *Proc. SPIE*, 9777-8, 2016.

[78] Courtesy of DOW Chemical Company.

[79] M. Muramatsu et al., “Pattern fidelity improvement of chemo-epitaxy DSA process for high-volume manufacturing,” in *Proc. SPIE*, 9777-14, 2016.

[80] H. Pathangi et al., “Block co-polymer contributions to the defectivity and roughness performance of the 14nm half-pitch LiNe flow @ imec,” in *Proc. SPIE*, 9777-15, 2016.

[81] F. Delachat, A. Gharbi, P. P. Barros et al., “Advanced surface affinity control for DSA contact hole shrink applications,” in *Proc. SPIE*, 10144, 2017.

[82] M. Muramatsu, T. Nishi, G. You, Y. Ido, and T. Kitano, “Pattern defect reduction for chemo-epitaxy DSA process,” in *Proc. SPIE 10960, Advances in Patterning Materials and Processes XXXVI,* 109600W, 2019.

[83] S. Xiao et al., “Pushing the limit of directed self-assembly and double patterning to 4nm half-pitch and beyond,” in *Proc. SPIE*, 9777-15, 2016.

[84] M. Muramatsu, T. Nishi1, G. You et al., “Pattern defect reduction and LER improvement of chemo-epitaxy DSA process,” in *Proc. SPIE 10144*, 101440Q, 2017.

[85] S. H. Park et al., “Block copolymer multiple patterning integrated with conventional ArF lithography,” *Soft Matter*, 6, 120, 2010.

[86] J. Y. Cheng et al., “Simple and versatile methods to integrate Directed Self-Assembly with optical lithography using a polarity-switched photoresist,” *ACS Nano*, 4, 4815-4823, 2010.

[87] M. Somervell, R. Gronheid, J. Hooge et al. “Comparison of directed self-assembly integrations,” in *Proc. SPIE*, 8325, 2012.

[88] H. S. Moon et al., “Large-area, highly oriented lamellar block copolymer nanopatterning directed by graphoepitaxially assembled cylinder nanopatterns,” *J. Mater. Chem.*, 22, 6307, 2012.

[89] S. J. Jeong and S. O. Kim, "Ultralarge-area block copolymer lithography via soft graphoepitaxy," *Journal of Material Chemistry*, 21, 5856, 2011.

[90] Y. S. Jung et al., "A path to ultranarrow patterns using self-assembled lithography," *Nano Lett.*, 10, 1000-1005, 2010.

[91] J. W. Jeong et al., "Highly tunable self-assembled nanostructures from a poly (2-vinylpyridine-b-dimethylsiloxane) block copolymer," *Nano Lett.,* 11, 4095-101, 2011.

[92] H. S. Suh, D. H. Kim, P. Mon et al., "Sub-10-nm patterning via directed self-assembly of block copolymer films with a vapour-phase deposited topcoat," *Nature Nanotechnology*, 12, 2017.

[93] A. Paquet et al., "Spacer patterning lithography as a new process to induce block copolymer alignment by chemo-epitaxy," in *Proc. SPIE 10958, Novel Patterning Technologies for Semiconductors, MEMS/NEMS, and MOEMS*, 109580M, 2019.

[94] S. Morita et al., "Sub-15nm patterning technology using directed self-assembly on nanoimprinting guide," in *Proc. SPIE*, 9777-19, 2016.

[95] A. Singh et al., "Patterning sub-25 nm half-pitch hexagonal arrays of contact holes with chemo-epitaxial DSA guided by ArFi pre-patterns," in *Proc. SPIE 9425*, 94250X, 2015.

[96] C-C. Liu et al., "Chemical Patterns for Directed Self-Assembly of Lamellae-Forming Block Copolymers with Density Multiplication of Features," *Macromolecules*, 46(4), 1415-1424, 2013.

[97] J. Kim et al., "SMART^{TM} process for directed block co-polymer self-assembly," *J. Photopolymer Sci. Technol.,* 26(5), 573-579, 2013.

[98] Y. Seino, Y. Kasahara, K. Miyagi et al., "Directed self-assembly lithography using coordinated line epitaxy (COOL) process," in *Proc. SPIE 9423*, 9423-41, 2015.

[99] B. H. Kim et al., “Surface Energy Modification by Spin-Cast, Large-Area Graphene Film for Block Copolymer Lithography,” *ACS Nano*, 4, 5464-5470, 2010.

[100] J. Y. Kim et al., “Flexible and Transferrable Self-Assembled Nanopatterning on Chemically Modified Graphene,” *Adv. Mater.*, 25, 1331-1335, 2013.

[101] C. K. Hyon et al., “Direct nanometer-scale patterning by the cantilever oscillation of an atomic force microscope,” *Appl. Phys. Lett.*, 75, 292–294, 1999.

[102] M. Wendel, S. Kühn, H. Lorenz, J. P. Kotthaus, and M. Holland, “Nanolithography with an atomic force microscope for integrated fabrication of quantum electronic devices,” *Appl. Phys. Lett.*, 65, 1775–1777, 1994.

[103] H. W. Schumacher, U. F. Keyser, U. Zeitler, R. J. Haug and K. Eberl, “Nanomachining of mesoscopic electronic devices using an atomic force microscope,” *Appl. Phys. Lett.*, 75, 1107–1109, 1999.

[104] Y. Yan, T. Sun, Y. Liang, and S. Dong, “Investigation on AFM-based micro/nano-CNC machining system,” *Int. J. Mach. Tools Manuf.*, 47, 1651–1659, 2007.

[105] Y. T. Mao et al., “Research on three dimensional machining effects using atomic force microscope,” *Rev. Sci. Instrum.*, 80, 065105, 2009.

[106] Y. Yan et al., “Top-down nanomechanical machining of three-dimensional nanostructures by atomic force microscope,” *Small,* 6, 724–728, 2010.

[107] Y. Sun, Y. Yan, Z. Hu, X. Zhao, and J. Yan, “3D polymer nanostructures fabrication by AFM tip-based single scanning with a harder cantilever,” *Tribol. Int.*, 47, 44–49, 2012.

[108] H. Mamin, and D. Rugar, “Thermomechanical writing with an atomic force microscope tip,” *Appl. Phys. Lett.*, 61, 1003-1005, 1992.

[109] D. Pires et al., “Nanoscale Three-Dimensional Patterning of Molecular Resists by Scanning Probes,” *Science,* 328, 732–736, 2010.

[110] J. E. Shaw, P. N. Stavrinou and T. D. Anthopoulos, "On-demand patterning of nanostructured pentacene transistors by scanning thermal lithography," *Adv. Mater.*, 25, 552–558, 2013.

[111] W. K. Lee et al., "Chemically isolated graphene nanoribbons reversibly formed in fluorographene using polymer nanowire masks," *Nano Lett.*, 11, 5461–5464, 2011.

[112] Z. Wei et al., "Nanoscale Tunable Reduction of Graphene Oxide for Graphene Electronics," *Science*, 328, 1373–1376, 2010.

[113] Y. Wei et al., "Efficient fabrication of carbon nanotube micro tip arrays by tailoring cross-stacked carbon nanotube sheets," *Nano Lett.*, 12, 2071–2076, 2012.

[114] S. T. Zimmermann, D. W. R. Balkenende, A. Lavrenova, C. Weder and J. Brugger, "Nanopatterning of a Stimuli-Responsive Fluorescent Supramolecular Polymer by Thermal Scanning Probe Lithography," *ACS Appl. Mater. Interfaces*, 9, 41454–41461, 2017.

[115] H. J. Mamin, "Thermal writing using a heated atomic force microscope tip," *Appl. Phys. Lett.*, 69, 433–435, 1996.

[116] B. Gotsmann, and U. Dürig, "Thermally Activated Nanowear Modes of a Polymer Surface Induced by a Heated Tip," *Langmuir*, 20, 1495–1500, 2004.

[117] R. A. Griffiths, A. Williams, I. Servin, and R. Tiron, "Corrigendum : Thermal scanning probe lithography for the directed self- assembly of block copolymers," *Nanotechnology*, 28, 1–9, 2017.

[118] H. J Kim et al., "Ultrananocrystalline diamond tip integrated onto a heated atomic force microscope cantilever," *Nanotechnology*, 23, 0–9, 2012.

[119] L. L. Cheong et al., "Thermal probe maskless lithography for 27.5 nm half-pitch Si technology," *Nano Lett.*, 13, 4485–4491, 2013.

[120] Y. K. Ryu Cho et al., "Sub-10 Nanometer Feature Size in Silicon Using Thermal Scanning Probe Lithography," *ACS Nano*, 11, 11890–11897, 2017.

[121] C. Rawlings et al., "Fast turnaround fabrication of silicon point-contact quantum-dot transistors using combined thermal scanning probe lithography and laser writing," *Nanotechnology*, 29, 505302, 2018.

[122] R. V. Martínez, J. Martínez, and R. Garcia, "Silicon nanowire circuits fabricated by AFM oxidation nanolithography," *Nanotechnology*, 21, 245301, 2010.

[123] F. M. Espinosa et al., "Direct fabrication of thin layer MoS2field-effect nanoscale transistors by oxidation scanning probe lithography," *Appl. Phys. Lett.*, 106, 1–5, 2015.

[124] S. Bertolazzi, D. Krasnozhon and A. Kis, "Nonvolatile memory cells based on MoS2/graphene heterostructures," *ACS Nano*, 7, 3246–3252, 2013.

[125] L. Wang et al., "Functionalized MoS2nanosheet-based field-effect biosensor for label-free sensitive detection of cancer marker proteins in solution," *Small*, 10, 1101–1105, 2014.

[126] A. I. Dago, Y. K. Ryu and R. Garcia, "Sub-20 nm patterning of thin layer WSe2 by scanning probe lithography," *Appl. Phys. Lett.*, 109, 2016.

[127] M. Lorenzoni,and B. Torre, "Scanning probe oxidation of SiC, fabrication possibilities and kinetics considerations," *Appl. Phys. Lett.*, 103, 163109, 2013.

[128] M. Cavallini et al., "Additive nanoscale embedding of functional nanoparticles on silicon surface," *Nanoscale*, 2, 2069–2072, 2010.

[129] R. D. Piner, J. Zhu, F. Xu, S. Hongand C. A. Mirkin, ""Dip-Pen" Nanolithography," *Science*, 283, 661-663, 1999.

[130] B. W. Maynor, S. F. Filocamo, M. W. Grinstaff and J. Liu, "Direct-writing of polymer nanostructures: poly(thiophene) nanowires on semiconducting and insulating surfaces," *J. Am. Chem. Soc.*, 124, 522-3, 2002.

[131] B. W. Maynor, J. Li, C. Lu and J. Liu, "Site-specific fabrication of nanoscale heterostructures: local chemical modification of GaN nanowires using electrochemical dip-pen nanolithography," *J. Am. Chem. Soc.*, 126, 6409-13, 2004.

[132] G. Agarwal, R. R. Naik and M. O. Stone, “Immobilization of Histidine-Tagged Proteins on Nickel by Electrochemical Dip Pen Nanolithography,” *J. Am. Chem. Soc.*, 125, 7408-7412, 2003.

[133] B. A. Nelson, W. P. King, A. R. Laracuente, P. E. Sheehan and L. J. Whitman, “Direct deposition of continuous metal nanostructures by thermal dip-pen nanolithography,” *Appl. Phys. Lett.,* 88, 1–3, 2006.

[134] W. K. Lee, Z. Dai, W. P. King and P. E. Sheehan, “Maskless nanoscale writing of nanoparticle-polymer composites and nanoparticle assemblies using thermal nanoprobes,” *Nano Letters*, 10, 129–133, 2010.

[135] S. Chung, J. R. Felts, D. Wang, W. P. King and J. J. D. Yoreo, “Temperature-dependence of ink transport during thermal dip-pen nanolithography,” *Appl. Phys. Lett.,* 99, 193101, 2011.

[136] J. Zhong, G. Sun and D. He, “Classic, liquid, and matrix-assisted dip-pen nanolithography for materials research,” *Nanoscale*, 6, 12217–12228, 2014.

[137] P.-C. Chen et al., “Polyelemental nanoparticle libraries,” *Science*, 352, 1565–1569, 2016.

[138] C. Santschi, J. Polesel-Maris, J. Brugger and H. Heinzelmann, in: A. A. Tseng (Ed.), Nanofabrication: Fundamentals and Applications, *World Scientific*, Singapore, 65—126, 2008.

[139] X. F. Wang and C. Liu, “Multifunctional Probe Array for Nano Patterning and Imaging,” *Nano Letter*, 5, 1867-1872, 2005.

[140] S. C. Minne et al., “Centimeter scale atomic force microscope imaging and lithography,” *Appl. Phys. Lett.*, 73, 1742, 1998.

[141] H. Pozidis et al., “Demonstration of thermomechanical recording at 641 Gbit/in/sup 2,” *IEEE Transactions on Magnetics*, 40, 2531-2536, 2004.

[142] K. Salaita et al., “Massively parallel dip-pen nanolithography with 55 000-pen two-dimensional arrays,” *Angew. Chem.*, Int. Ed. 45, 7220-3, 2006.

[143] Koelmans, W. et al., “Parallel optical readout of cantilever arrays in dynamic mode,” *Nanotechnology*, 21, 395503, 2010.

[144] A. A. Tseng, "Advancements and challenges in development of atomic force microscopy for nanofabrication," *Nano Today*, 6, 493—509, 2011.

[145] P. Paul, A. Knoll, F. Holzner and U. Duerig, "Field stitching in thermal probe lithography by means of surface roughness correlation," *Nanotechnology*, 23, 385307, 2012.

[146] T. Ando, T. Uchihashi and N. Kodera, "High-speed AFM and applications to biomolecular systems," *Ann. Rev.Biophys.*, 42, 393-414, 2013.

[147] K. B. Lee, J. H. Lim, and C. A. Mirkin, "Protein nanostructures formed via direct-write dip-pen nanolithography," *Journal of the American Chemical Society*, 125(19), 5588-5589, 2003.

[148] J. N. Israelachvili, "Intermolecular and Surface Forces," *3rd ed., Academic Press*, London, 2011.

[149] H. Sugimura, and N. Nakagiri, "Chemical approach to nanofabrication: modifications of silicon surfaces patterned by scanning probe anodization," *Japanese Journal of Applied Physics*, 34(Part 1, No. 6B), 3406-3411, 1995.

[150] J. A. Dagata et al., "Role of space charge in scanned probe oxidation," *Journal of Applied Physics*, 84(12), 6891-6900, 1998.

[151] P. Avouris, T. Hertel and R. Martel, "Atomic force microscope tip-induced local oxidation of silicon: kinetics, mechanism, and nanofabrication," *Applied Physics Letters*, 71(2), 285-287, 1997.

[152] S. Gwo, "Scanning probe oxidation of Si3N4 masks for nanoscale lithography, micromachining, and selective epitaxial growth on silicon," *Journal of Physics and Chemistry of Solids*, 62(9-10), 1673-1687, 2001.

[153] H. Bloeß, G. Staikov and J.W. Schultze, "AFM induced formation of SiO_2 structures in the electrochemical nanocell," *Electrochimica Acta*, 47, 335–344, 2001.

[154] T. Mühl, J. Kretz, I. Mönch, C.M.Schneider, H. Brückl and G. Reiss, "Parallel nanolithography in carbon layers with conductive imprint stamps," *Appl. Phys. Lett.*, 76, 786, 2000.

[155] A. Yokoo, "Nanoelectrode lithography and multiple patterning," *J. Vac. Sci. Technol. B*, 21 (6), 2966, 2003.

[156] R. V. Martinez, N. S. Losilla, J. Martinez, M. Tello and R. Garcia, "Sequential and parallel patterning by local chemical nanolithography," *Nanotechnology,* 18, 084021, 2007.

[157] B. Liu, A. J. Bard, M. V. Mirkin and S. E. Creager, "Electron Transfer at Self-Assembled Monolayers Measured by Scanning Electrochemical Microscopy," *J. Am. Chem. Soc.*, 126, 5, 1485-1492, 2004.

[158] C. F. Chen, S. D. Tzeng, M. H. Lin and S. Gwo, "Electrostatic Assembly of Gold Colloidal Nanoparticles on Organosilane Monolayers Patterned by Microcontact Electrochemical Conversion," *Langmuir*, 22, 7819, 2006.

[159] R. Garcia, A. Knoll and E. Riedo, "Advanced scanning probe lithography," *Nature Nanotech*, 9, 577–587, 2014.

[160] M. Kerkhof, H. Jasper, L. Levasier et al., "Enabling sub-10nm node lithography: presenting the NXE:3400B EUV scanner," in *Proc. SPIE 10143*, 101430D, 2017.

[161] A. S. Gangnaik et al., "Novel germanium surface modification for sub-10 nm patterning with electron beam lithography and HSQ resist," *J. Vac. Sci. Technol., B: Nanotechnol. Microelectron.: Mater., Process., Meas., Phenom*, 34, 041603, 2016.

[162] I. Servin, N. A. Thiam, P. Pimenta-Barros et al., "Ready for multi-beam exposure at 5 kV on MAPPER tool: Lithographic and process integration performances of advanced resists/stack," in *Proc. SPIE 9423*, 94231C, 2015.

[163] A. P. Malshe et al., "Tip-based nanomanufacturing by electrical, chemical, mechanical, and thermal processe," *CIRP Ann. - Manuf. Technol.,* **59**, 628–651, 2010.

[164] R. Garcia, R. V. Martinez and J. Martinez, "Nano-chemistry and scanning probe nanolithographies," *Chem. Soc. Rev.,* **35**, 29–38, 2006.

[165] Q. He, C. Tan and H. Zhang, "Recent Advances in Cantilever-Free Scanning Probe Lithography: High-Throughput, Space-Confined Synthesis of Nanostructures and beyond," *ACS Nano,* **11**, 4381–4386, 2017.

[166] E. Bellido et al., "Nanoscale positioning of inorganic nanoparticles using biological ferritin arrays fabricated by Dip-Pen Nanolithography," *Scanning,* **32**, 35–41, 2010.

[167] C. Rawlings, U. Duerig, J. Hedrick, D. Coady and A. W. Knoll, "Nanometer accurate markerless pattern overlay using thermal scanning probe lithography," *IEEE Trans. Nanotechnol.*, 13(6), 1204-1212, 2014.

[168] H.-M. Chien et al., "On the nature of defects created on graphene by scanning probe lithography under ambient conditions," *CARBON*, 80, 318-324, 2014.

[169] J. Martinez et al., "Development of a parallel local oxidation nanolithography instrument," *Review of Scientific Instruments*, 77, 086106, 2006.

[170] K. Park, W.-B. Jung, K. Kwon, O. D. Lavrentovich and H.-T. Jung, "Sub-5 nm Dendrimer Directed Self-assembly with Large-area Uniform Alignment By Graphoepitaxy," *Advanced Functional Materials*, 29(26), 1901876, 2019.

[171] S. Luryi, J. Xu and A. Zaslavsky, "Future trends in microelectronics:Journey into the unknown," *New Jersey: John Wiley & Sons*, 30, 2016.

[172] Q. Dai, J. Frommer, D. A. Berman, K. Virwani, B. Davis, J. Y. Cheng and A. Nelson, "High-throughput directed self-assembly of core-shell ferrimagnetic nanoparticle arrays," *Langmuir : the ACS journal of surfaces and colloids*, 29(24), 7472-7, 2013.

[173] T. Azuma et al., "Fabrication of Sub-10 nm Metal Wire Circuits using Directed Self-Assembly of Block Copolymers," *Journal of Photopolymer Science and Technology*, 29(5), 647-652, 2016.

[174] K. Fukuhara et al.,"Overlay improvement in nanoimprint lithography for 1×-nm patterning," *Journal of Vacuum Science & Technology B, Nanotechnology and Microelectronics: Materials, Processing, Measurement, and Phenomena*, 34, 06K405, 2016.

[175] K. Sakai et al., "The advantages of nanoimprint lithography for semiconductor device manufacturing," in *Proc. SPIE 10958, Novel Patterning Technologies for Semiconductors, MEMS/NEMS, and MOEMS*, 109580G, 2019.

[176] B. J. Alder and T. E. Wainwright, "Phase Transition for a Hard Sphere System," *J. Chem. Phys.*, 27, 1208-1209, 1957.

[177] L. Verlet, "Computer" experiments" on classical fluids. I. Thermodynamical properties of Lennard-Jones molecules," *Physical review*, 159(1), 98-103, 1967.

[178] R. W. Hockney and J. W. Eastwood, "Computer Simulation Using Particles," *McGraw-Hill*, New York, 1981.

[179] H. C. Andersen, "Molecular dynamics simulations at constant pressure and/or temperature," *The Journal of Chemical Physics.*, 72(4), 2384-2393, 1980.

[180] H. J. C. Berendsen, J. P. M. Postma, W. F. van Gunsteren, A. DiNola, J. R. Haak, "Molecular-Dynamics with Coupling to an External Bath," *Journal of Chemical Physics.*, 81(8), 3684–3690, 1984.

[181] S. Nosé, "A unified formulation of the constant temperature molecular-dynamics methods," *Journal of Chemical Physics.*, 81(1), 511–519, 1984.

[182] W. G. William "Canonical dynamics: Equilibrium phase-space distributions," *Phys. Rev. A.*, 31(3), 1695–1697, 1985.

[183] M. I. Baskes, J. S. Nelson and A. F. Wright, "Semiempirical modified embedded-atom potentials for silicon and germanium," *Physical Review B*, 40(9), 6085-6100, 1989.

[184] F. H. Stillinger and T. A. Weber, "Computer simulation of local order in condensed phases of silicon," *Physical Review B*, 31(8), 5262-5271, 1985.

[185] J. Tersoff, "Empirical interatomic potential for silicon with improved elastic properties," *Physical Review B*, 38(14), 9902-9905, 1988.

[186] J. Tersoff, "New empirical approach for the structure and energy of covalent systems," *Physical Review B*, 37(12), 6991-7000, 1988.

[187] J. Tersoff, "Modeling solid-state chemistry: Interatomic potentials for multicomponent systems," *Physical Review B*, 39(8), 5566-5568, 1989.

[188] J. Tersoff, "Erratum: Modeling solid-state chemistry: Interatomic potentials for multicomponent systems," *Physical Review B*, 41(5), 3248-3248, 1990.

[189] J. Godet, L. Pizzagalli, S. Brochard, and P. Beauchamp, "Comparison between classical potentials and ab initio methods for silicon under large shear," *Journal of Physics: Condensed Matter*, 15(41), 6943-6953, 2003.

[190] L. Pizzagalli, P. Beauchamp and J. Rabier, "Undissociated screw dislocations in silicon: calculations of core structure and energy," *Phil. Mag. A*, 83, 1191, 2003.

[191] J. Rabier, L. Pizzagalli and J-L Demenet, "Dislocations in silicon at high stress," *Dislocation in Solids*, Volume 16 ed L. Kubin and J. P. Hirth (Amsterdam: Elsevier) p 47 (chapter 93), 2010.

[192] K. Kang and W. Cai, "Brittle and ductile fracture of semiconductor nanowires—molecular dynamics simulations," *Phil. Mag*., 87, 2169, 2007.

[193] J. Guenole, J. Godet and S. Brochard, "Deformation of silicon nanowires studied by molecular dynamics simulations," *Modelling Simul. Mater. Sci. Eng.*, 19, 074003, 2011.

[194] W. D. Luedtke and U. Landman, "Preparation, structure, dynamics, and energetics of amorphous silicon: a molecular-dynamics study," *Phys. Rev. B*, 40 1164, 1989.

[195] C. Fusco, T. Albaret and A. Tanguy, "The role of local order in the small-scale plasticity of model amorphous materials," *Phys. Rev. E*, 82, 066116, 2010.

[196] M. I. Baskes, "Modified embedded-atom potentials for cubic materials and impurities," *Phys. Rev. B*, 46, 2727, 1992.

[197] B. J. Thijsse, "Silicon potentials under (ion) attack: towards a new MEAM model," *Nucl. Instrum. Methods B*, 228 198, 2005.

[198] M. Timonova, B. J. Lee and B. J. Thijsse, "Sputter erosion of Si(001) using a new silicon MEAM potential and different thermostats," *Nucl. Instrum. Methods B*, 255, 195, 2007.

[199] S. Ryu, C. R. Weinberger, M. I. Baskes and W. Cai W, "Improved modified embedded-atom method potentials for gold and silicon," *Modelling Simul. Mater. Sci. Eng.*, 17, 075008, 2009.

[200] M. Timonova and B. J. Thijsse, "Optimizing the MEAM potential for silicon," *Modelling Simul. Mater. Sci. Eng.*, 19, 015003, 2011.

[201] D. W. Brenner, "The Art and Science of an Analytic Potential," in *Computer Simulation of Materials at Atomic Level (John Wiley & Sons, Ltd),* Chap. 2, pp. 23–40, 2005.

[202] Z. Fan et al., "A minimal Tersoff potential for diamond silicon with improved descriptions of elastic and phonon transport properties," *Journal of Physics: Condensed Matter*, 32(13), 2019.

[203] P. M. Agrawal, L. M. Raff, and R. Komanduri, "Monte Carlo simulations of voidnucleated melting of silicon via modification in the Tersoff potential parameters," *Physical Review B*, 72(12), 125206-125217, 2005.

[204] A. C. T. van Duin, S. Dasgupta, F. Lorant, and W. A. Goddard, "ReaxFF: A Reactive Force Field for Hydrocarbons," *The Journal of Physical Chemistry A*, 105(41), 9396-9409, 2001.

[205] A. C. T. van Duin, "The ReaxFF method and its applications to atomistic-scale simulations on atomic-layer deposition and chemical vapor deposition in complex 2D-materials," *2D Crystal consortium*, 2018.

[206] U. Khalilov, G. Pourtois, S. Huygh, A. C. T. Van Duin, E. C. Neyts and A. Bogaerts, "New mechanism for oxidation of native silicon oxide," *Journal of Physical Chemistry C*, 117, 9819–9825, 2013.

[207] S. Dumpala, S. R. Broderick, U. Khalilov, E. C. Neyts, A. C. T. Van Duin, J. Provine, R. T. Howe and K. Rajan, "Integrated atomistic chemical imaging and reactive force field molecular dynamic simulations on silicon oxidation," *Applied Physics Letters,* 106, 2015.

[208] J. Wen, T. Ma, W. Zhang, A. C. T. Van Duin and X. Lu, "Surface orientation and temperature effects on the interaction of silicon with water: Molecular

dynamics simulations using ReaxFF reactive force field," *Journal of Physical Chemistry A*, 121, 587–594, 2017.

[209] Y. Sun, Y. Liu, X. Chen, Z. Zhai, F. Xu and Y. Liu, "Micromechanism of oxygen transport during initial stage oxidation in Si(100) surface: A ReaxFF molecular dynamics simulation study," *Applied Surface Science*, 406, 178–185, 2017.

[210] Y. Sun, X.-F. Chen, Z. Zhai, S.-H. Tian, Y.-L. Liu and S. Izumi, "Initial stage oxidation on nano-trenched Si(1 0 0) surface," *Journal of Physics D: Applied Physics*, 51, 015305, 2018.

[211] M. A. Pamungkas, B. H. Kim and K. R. Lee, "Reactive molecular dynamic simulations of early stage of wet oxidation of Si (001) surface," *Journal of Applied Physics*, 114, 073506, 2013.

[212] M. A. Pamungkas, M. Joe, B. H. Kim and K. R. Lee, "Reactive molecular dynamics simulation of early stage of dry oxidation of Si (100) surface," *Journal of Applied Physics*, 110, 053513, 2011.

[213] T. Cramer, F. Zerbetto and R. García, "Molecular mechanism of water bridge buildup: Field-induced formation of nanoscale menisci," *Langmuir*, 24, 6116–6120, 2008.

[214] C. D. Daub, D. Bratko, K. Leung and A. Luzar, "Electrowetting at the nanoscale," *Journal of Physical Chemistry C*, 111, 505–509, 2007.

[215] A. Notargiacomo and A. A. Tseng, "Assembling uniform oxide lines and layers by overlapping dots and lines using AFM local oxidation," *Nanotechnology,* (IEEE-NANO), 907, 2009.

[216] L. Filipovic and S. Selberherr, "Electric Field Based Simulations of Local Oxidation Nanolithography using Atomic Force Microscopy in a Level Set Environment," *ECS Transactions*, 49(1), 265-272, 2012.

[217] B. Theogene et al., "3-D finite element calculation of electric field enhancement for nanostructures fabrication mechanism on silicon surface with AFM tip induced local anodic oxidation," *Integrated Ferroelectrics*, 190(1), 129-141, 2018.

[218] M. Luna, J. Colchero and A. M. Baró, “Intermittent contact scanning force microscopy: The role of the liquid necks,” *Applied Physics Letters*, 72, 3461–3463, 1998.

[219] M. Calleja and R. García, “Nano-oxidation of silicon surfaces by noncontact atomic-force microscopy: Size dependence on voltage and pulse duration,” *Applied Physics Letters*, 76, 3427–3429, 2000.

[220] T. Baumgärtel and H. Graaf, In book: Lithography: Principles, Processes and Materials Chapter: Local anodic oxidation nanolithography on silicon – Chemical routes to functional nanostructures, Publisher: Nova science publishers, Editors: T.C. Hennessey, 2011.

[221] Y.-R. Ma, C. Yu, Y.-D. Yao, Y. Liou, and S.-F. Lee, “Tip-induced local anodic oxidation on the native SiO2 layer of Si(111) using an atomic force microscope,” *Physical Review B*, 64, 195324, 2001.

[222] A. E. Gordon et al., “Mechanisms of surface anodization produced by scanning probe microscopes,” *Journal of Vacuum Science & Technology B: Microelectronics and Nanometer Structures*, 13(6), 2805-2808, 1995.

[223] S. Plimpton, “Fast Parallel Algorithms for Short-Range Molecular Dynamics,” *Journal of Computational Physics*, 117, 1–42, 1995.

[224] O. Assowe, O. Politano, V. Vignal, P. Arnoux, B. Diawara, O. Verners and A. C. T. Van Duin, “Reactive molecular dynamics of the initial oxidation stages of Ni(111) in pure water: Effect of an applied electric field,” *Journal of Physical Chemistry A*, 116, 11796–11805, 2012.

[225] A. Stukowski, “Visualization and analysis of atomistic simulation data with OVITO–the Open Visualization Tool,” *Modelling and Simulation in Materials Science and Engineering*, 18(1), 015012-015019, 2009.

[226] A. Van Duin et al., “ReaxFF force fields: Development of a transferable empirical method for atomic-scale simulations of chemical reactions,” *Interatomic Potentials Workshop*, Oxford, 2008.

[227] K. D. Nielson, A. C. T. van Duin, J. Oxgaard, W. Q. Deng and W. A. Goddard, “Development of the ReaxFF Reactive Force Field for Describing Transition Metal

Catalyzed Reactions, with Application to the Initial Stages of the Catalytic Formation of Carbon Nanotubes," *Journal of Physical Chemistry A*, 109, 493, 2005.

[228] K.-I. Nomura, R. K. Kalia, A. Nakano and P. Vashishta, "A scalable parallel algorithm for large-scale reactive force-field molecular dynamics simulations," *Computer Physics Communications*, 178, 73–87, 2008.

[229] K. Chenoweth, A. C. T. van Duin and W. Goddard, "ReaxFF Reactive Force Field for Molecular Dynamics Simulations of Hydrocarbon Oxidation," *J. Phys. Chem. A*, 112(5), 1040−1053, 2008.

[230] W. J. Mortier, S. K. Ghosh, and S. Shankar, "Electronegativity-equalization method for the calculation of atomic charges in molecules," *J. Am. Chem. Soc.*, 108, 4315, 1986.

[231] G. O. A. Janssens, B. G. Baekelandt, H. Toufar, W. J. Mortier, and R. A. Schoonheydt, "Comparison of Cluster and Infinite Crystal Calculations on Zeolites with the Electronegativity Equalization Method (EEM)," *J. Phys. Chem.,* 99, 3251, 1995.

[232] A. K. Rappe and W. A. Goddard III, "Charge Equilibration for Molecular Dynamics Simulations," *Journal of Physical Chemistry*, 95, 3358–3363, 1991.

[233] J. Chen and T. J. Martínez, "Charge conservation in electronegativity equalization and its implications for the electrostatic properties of fluctuating-charge models," *Journal of Chemical Physics*, 131, 044114-1-044114-3, 2009.

[234] J. Wen et al., "Atomic insight into tribochemical wear mechanism of silicon at the Si/SiO_2interface in aqueous environment: Molecular dynamics simulations using ReaxFF reactive force field," *Applied Surface Science*, 390, 216–223, 2016.

[235] G. Psofogiannakis and A. C. T. Van Duin, "Development of a ReaxFF reactive force field for Si/Ge/H systems and application to atomic hydrogen bombardment of Si, Ge, and SiGe (100) surfaces," *Surface Science*, 646, 253–260, 2016.

[236] A. C. T. van Duin, C. Zou, K. Joshi, W. A. Goddard and V. Bryantsev, "A Reaxff Reactive Force-field for Proton Transfer Reactions in Bulk Water and its

Applications to Heterogeneous Catalysis, in: Computional Catalysis. RSC Catalysis Series," *Royal Society of Chemistry*, Cambridge, 223–243, 2013.

[237] D. Wolf and S. Yip, "Materials Interfaces: Atomic-level structure and properties," *Springer Netherland*, Edition 1, p. 137, 1993.

[238] G. P. Purja Pun and Y. Mishin, "Optimized interatomic potential for silicon and its application to thermal stability of silicene," *Physical Review B*, 95, 224103, 2017.

[239] M. T. Yin and M. L. Cohen, "Theory of static structural properties, crystal stability, and phase transformations: Application to Si and Ge," *Physical Review B,* 26, 5668, 1982.

[240] G. Lu, M. Huang, M. Cuma, and F. Liu, "Relative stability of Si surfaces: A first-principles study," *Surface Science*, 588, 61, 2005.

[241] B. Jelinek, S. Groh, M. F. Horstemeyer, J. Houze, S. G. Kim, G. J. Wagner, A. Moitra, and M. I. Baskes, "Modified embedded atom method potential for Al, Si, Mg, Cu, and Fe alloys," *Physical Review B,* 85, 245102, 2012.

[242] C. Kittel, "Introduction to Sold State Physics", *Wiley Interscience*, New York, 1986.

[243] D. J. Eaglesham, A. E. White, L. C. Feldman, N. Moriya, and D. C. Jacobson, "Equilibrium Shape of Si," *Phys. Rev. Lett.*, 70, 1643, 1993.

[244] R. Garcia, M. Calleja and H. Rohrer, "Patterning of silicon surfaces with noncontact atomic force microscopy: Field-induced formation of nanometer-size water bridges," *Journal of Applied Physics*, 86, 1898–1903, 1999.

[245] Y. Chabal, "Hydride formation on the Si (100): H2O surface," *Physical Review B*, 29, 3677–3680, 1984.

[246] M. Chander, Y. Z. Li, J. C. Patrin and J. H. Weaver, "Si(100)-(2×1) surface defects and dissociative and nondissociative adsorption of H_2O studied with scanning tunneling microscopy," *Physical Review B*, 48, 2493–2499, 1993.

[247] P. A. Fontaine, E. Dubois, and D. Stievenard, “Characterization of scanning tunneling microscopy and atomic force microscopybased techniques for nanolithography on hydrogen-passivated silicon,” *J. Appl. Phys.*, 84, 1776, 1998.

[248] J. D. Baran, H. Grönbeck, and A. Hellman, “Mechanism for Limiting Thickness of Thin Oxide Films on Aluminum,” *Physical Review Letters*, 112, 146103, 2014.

[249] M. V. Coleman and D. J. D. Thomas, “The Structure of Silicon Oxide Films,” *Physica Status Solidi (B)*, 22, 593–602, 1967.

[250] T. Uchiyama and M. Tsukada, “Atomic and electronic structures of oxygen-adsorbed Si(001) surfaces,” *Physical Review B*, 53, 7917–7922, 1996.

[251] T. Uchiyama and M. Tsukada, “Scanning-tunneling-microscopy images of oxygen adsorption on the Si(001) surface,” *Physical Review B*, 55, 9356–9359, 1997.

[252] D. Stievenard, P. A. Fontaine, and E. Dubois, “Nanooxidation using a scanning probe microscope: An analytical model based on field induced oxidation,” *Appl. Phys. Lett.*, 70, 3272, 1997.

[253] N. Cabrera and N. F. Mott, “Theory of the oxidation of metals,” *Reports Prog. Phys.*, 12, 308, 1949.

[254] T. W. Sigmon, W. K. Chu, E. Lugujjo, and J. W. Mayer, “Stoichiometry of thin silicon oxide layers on silicon,” *Appl. Phys. Lett.*, 24, 105, 1974.

[255] H. Kuramochi, K. Ando and H. Yokoyama, “Effect of humidity on nano-oxidation of p-Si(0 0 1) surface,” *Surface Science*, 542, 56–63, 2003.

[256] H. Z. Massoud, J. D. Plummer and E. A. Irene, “Thermal Oxidation of Silicon in Dry Oxygen Growth Rate Enhancement in the Thin Regime,” *J. Electrochem. Soc.*, 132, 2685, 1985.

[257] E. A. Irene, H. Z. Massoud and E. Tierney, “Silicon Oxidation Studies: Silicon Orientation Effects on Thermal Oxidation,” *J. Electrochem. Soc.*, 133, 1253, 1986.

[258] E. A. Lewis and E. A. Irene, “The Effect of Surface Orientation on Silicon Oxidation Kinetics,” *J. Electrochem. Soc.*, 134, 2332, 1987.

[259] J. L. Ngau, P. B. Griffin and J. D. Plummer, “Silicon Orientation Effects in the Initial Regime of Wet Oxidation,” *Journal of The Electrochemical Society*, 149(8), F98-F101, 2002.

[260] J. R. Lagenza, “Effect of crystal orientation on oxidation rates of silicon In high pressure steam,” *J. Phys. Chem. Solids.*, 65, 2011-2014, 1961.

[261] F. Z. Fang, H. Wu and Y. C. Liu., “Modeling and experimental investigation on nanometric cutting of monocrystalline silicon,” *International Journal of Machine Tools & Manufacture*, 45, 1681–1686, 2005.

[262] G. Li et al., “Micro cutting of V-shaped cylindrical grating template for roller nano-imprint,” *Journal of Materials Processing Technology*, 213, 895–904, 2013.

[263] L. Oria, A. R. de Luzuriaga, J. A. Alduncin and F. Perez-Murano, “Polystyrene as a brush layer for directed self-assembly of block co-polymers,” *Microelectronic Engineerin*g, 110, 234–240, 2013.

[264] T. W. Odom, J. C. Love, D. B. Wolfe et al., “Improved Pattern Transfer in Soft Lithography Using Composite Stamps,” *Langmuir*, 18, 13, 5314-5320, 2002.

[265] D. Le, J.-M. Lee, S.-J. Kim, D.-Y. Lee and S.-W. Lee, “Burr analysis in microgrooving,” *The International Journal of Advanced Manufacturing Technology*, 50, 569–577, 2010.

[266] R. Huang, X. Zhang and K. Liu, “Micromachining of Roller Mold for Roll-to-Roll Manufacturing,” in *Yan J. (eds) Micro and Nano Fabrication Technology, Micro/Nano Technologies*, vol. 1. Springer, Singapore, 2018.

[267] H. Hertz, “Über die berührung fester elastischer Körper (On the contact of rigid elastic solids),” in *Miscellaneous Papers. Jones and Schott, Editors, J. reine und angewandte Mathematik 92*, Macmillan, London, 156, 1896, English translation: Hertz, H.

[268] J. Williams, “Contact between surfaces,” in *Engineering Tribology*, Cambridge: Cambridge University Press, 73-131, 2005.

[269] J. Sun, X. Luo, W. Chang, J. M. Ritchie, J. Chien and A. Lee, "Fabrication of periodic nanostructures by single-point diamond turning with focused ion beam built tool tips," *J. Micromech. Microeng.*, 22, 115014, 2012.

[270] Courtesy of NEWWAY air bearings Company.